Viscous Fluid Sheets

by

Nikos Savva

B.S., University of Wisconsin-Madison (2001)

Submitted to the Department of Mathematics
in partial fulfillment of the requirements for the degree of

DOCTOR OF PHILOSOPHY

at the

MASSACHUSETTS INSTITUTE OF TECHNOLOGY

September 2007

Signature of Author . . . .
Department of Mathematics
9 July 2007
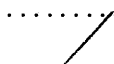
Certified by. . . . .
John W. M. Bush
Associate Professor of Applied Mathematics
Thesis Supervisor

Accepted by . . . .
Alar Toomre
Chairman, Applied Mathematics Committee

Accepted by . . . .
David Jerison
Chairman, Departmental Committee on Graduate Students
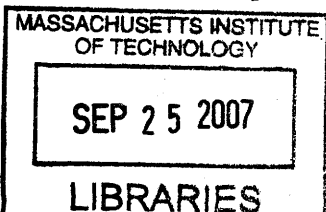
Viscous Fluid Sheets

by

Nikos Savva

Submitted to the Department of Mathematics
on 9 July 2007, in partial fulfillment of the
requirements for the degree of
DOCTOR OF PHILOSOPHY

Abstract

We present a general theory for the dynamics of thin viscous sheets. Employing concepts from diffferential geometry and tensor calculus we derive the governing equations in terms of a coordinate system that moves with the film. Special attention is given to incorporating inertia and the curvature forces that arise from the thickness variations along the film. Exploiting the slenderness of the film, we assume that the transverse fluid velocity is small compared to the longitudinal one and perform a perturbation expansion to obtain the leading order equations when the center-surface that defines the coordinate system is parametrized by lines of curvature. We then focus on the dynamics of flat film rupture, in an attempt to gain some insights into the sheet breakup and its fragmentation into droplets. By combining analytical and numerical methods, we extend the prior work on the subject and compare our numerical simulations with experimental work reported in the literature.

Thesis Supervisor: John W. M. Bush
Title: Associate Professor of Applied Mathematics

Acknowledgments

Contents

List of Figures

Chapter 1

Introduction

1.1 Background

Thin fluid sheets are encountered in a wide range of natural and industrial processes, making their study of interest to both scientists and engineers. The disintegration of fluid sheets into droplets, is desirable in a variety of industrial applications, such as spray painting and fuel injection (for an overview see [123] and the references therein). Conversely, the instabilities leading to sheet breakup is to be avoided in other applications, as in glass-blowing [45], the commercial filling of containers [97] or in curtain coating [79], where a thin layer of fluid is deposited on a moving substrate (see figure 1-1).

Sheet disintegration (see figure 1-2) is of primary importance in the context of fluid atomization (e.g. the texts by Lefebvre [72] and Bayvel & Orzechowski [7]). Atomization is the process by which a fluid volume undergoes topological changes due to instabilities and evolves into structures of progressively smaller size. Commonly, a critical step in the atomization process involves the progression from sheets to filaments to drops. The ability to understand the underlying mechanisms for drop formation and predict their size can be a deciding factor when it comes to the performance of, say, a combustion engine or a spray painting process [123]. While the mechanism of filament breakup into droplets has been extensively studied and is well understood since the seminal work of Lord Rayleigh ([20], [93]), filament formation and detachment from the film edge have not received as much attention.

Research on fluid sheets was initiated by the early exploratory experiments of Savart (1833), who in a series of papers investigated the sheets formed when a fluid jet impinges
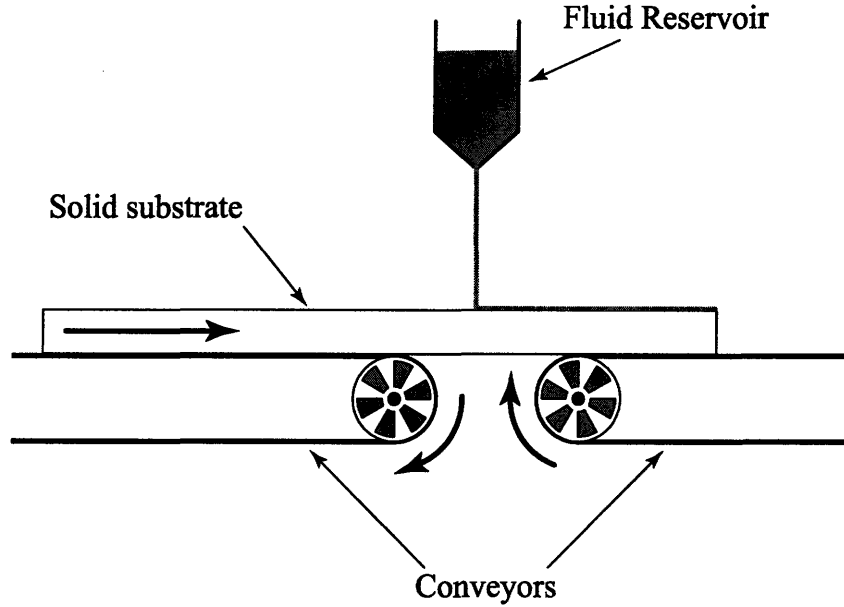
Figure 1-1: Thin film deposition on a moving substrate (curtain coating)

on a circular impactor ([100],[101]) and when two jets collide with each other [102]. Since then, many studies have been conducted on fluid sheets, the most important and relevant of which we review in this chapter.

Sheet formation by jet impingement is dependent on the flow parameters. For instance, a flat sheet will be generated by a vertical jet striking a horizontal impactor provided that the Froude number, Fr, is large:

$$\text{Fr} = \frac{\text{inertia}}{\text{gravity}} = \frac{U_0^2}{gD_0} \gg 1 \ , \tag{1.1}$$

where g is the acceleration due to gravity, D_0 is the jet diameter and U_0 is the fluid speed at the impactor. In this case, the film extends radially to a critical radius R, where a rim forms, and eventually disintegrates into small drops. The resulting flow also depends on the Weber number, defined as:

$$\text{We} = \frac{\text{inertia}}{\text{surface tension}} = \frac{\rho U_0^2 D_0}{\gamma} \ , \tag{1.2}$$

where ρ is the fluid density and γ the surface tension. Savart observed two distinct regimes: below a critical Weber number, $\text{We}_c \approx 1000$, the sheet remains flat up to the rim and as

11

Droplets

Rim

Sheet

Rim-driven Instability

Droplets

Filaments

Waves

Sheet

Wave-driven Instability
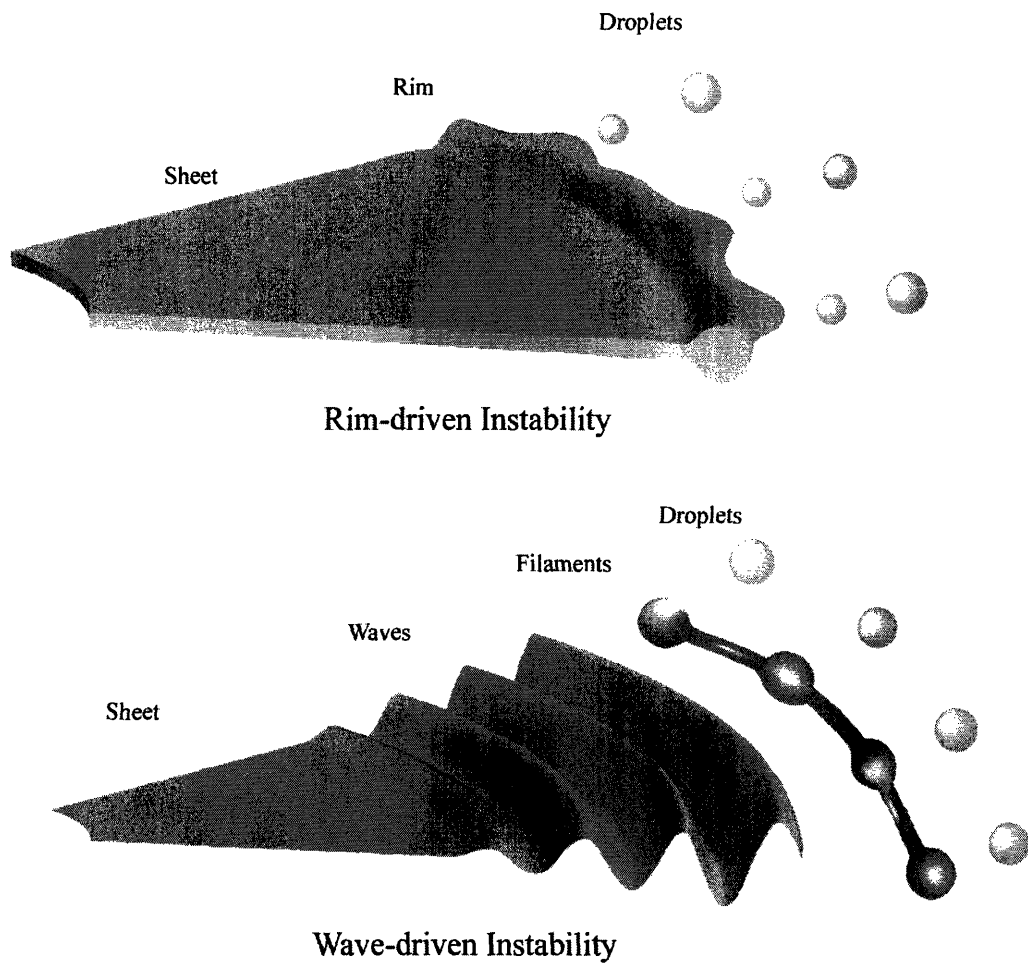
Figure 1-2: Sketch of different mechanisms for sheet disintegration. In rim-driven disintegration capillary instability causes the pinching of the rim to droplets due to the capillary instability. Wave-driven instabilities are created by the flapping of the sheet, induced by the ambient air.

We_c is exceeded, the sheet begins to flap violently and create audible sounds.

Savart's observations were followed by a number of studies devoted to expanding sheets. Taylor [114] deduced the critical radius R in the smooth sheet regime. By assuming a constant speed up to the rim and balancing the film inertia to surface tension forces, he obtained

$$\rho U_0^2 h \sim 2\gamma, \tag{1.3}$$

12

where h is the film thickness, found by the conservation of flux, Q, within the sheet:

$$Q = \tfrac{1}{4}\pi D_0^2 U_0 = 2\pi R h U_0^2 \Rightarrow h = \frac{D_0^2}{8R} \ .$$

(1.4)

Combining the last two equations yields the critical sheet radius:

$$R = \frac{\mathrm{We}}{16} D_0 \ ,$$

(1.5)

that is consistent with Savart's experiments. The rim that develops at this radius becomes unstable to azimuthal perturbations and pinches-off due to the capillary instability [93] (see figure 1-2). The smooth sheet regime was further explored by Clanet & Villermaux [26], who focused on the transient formation and destruction of the sheets as the source was turned on and off respectively.

Huang's experiments [59] offered more data supporting Taylor's result, and also deduced the critical Weber number, We_c, at the onset of the flapping regime. In this regime, the ambient air becomes dynamically significant and the maximum radial extension of the film evolves according to $R \sim \mathrm{We}^{-1/3} D_0$. Sheet disintegration is now wave-driven, as shown in figure 1-2. Analytical work via linear stability analysis was performed by Weihs [125] and a more detailed experimental study was presented by Villermaux & Clanet [122], who further elucidated some of the mechanisms of droplet shedding and gave scaling arguments for the droplet sizes. Additional work done in the context of atomization can be found in the articles by Dombrowski & Fraser [38], Crapper $et\ al.$ [28], Bremond & Villermaux [12], Villermaux [123] and the references therein.

A sheet punctured by a needle retracts due to unbalanced surface tension forces; this is in some sense the opposite configuration to the expanding sheet, but both share similar characteristics. Bursting phenomena arise in a wide range of physical settings, ranging from foams in the food industry to biological membranes (for an overview see [49]). Depending on the application at hand, film rupture can be either desirable, as in spray formation [88], or undesirable, as in curtain coating [79]. The initial observations of soap film rupture were reported by Rayleigh [94] and Dupré [40] in the late 1800's; their systematic study initiated the experimental work of Ranz in 1959 [92]. In his experiments he observed that upon puncture, the film recedes at a constant speed under the influence of surface tension and fluid accumulates in a roughly circular rim as it is drawn away from the point

$$u_c = \delta l / \delta t$$

$$\delta m = \rho H \delta l$$

$$\gamma, \rho$$

$$\updownarrow H$$

$$\delta l$$
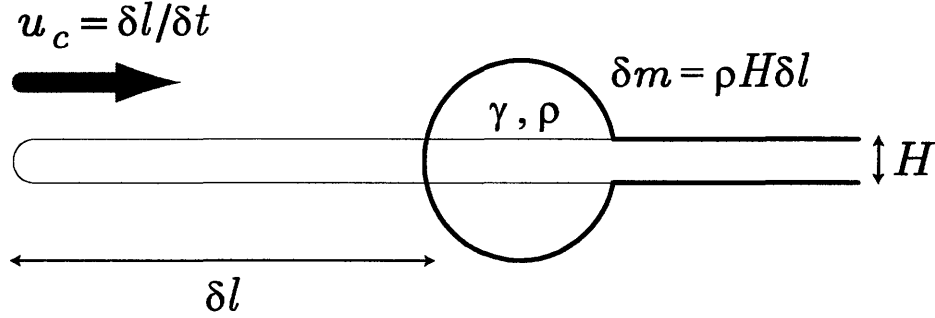
Figure 1-3: Retraction of a planar film. In time δt, the tip of the film moves by a distance $\delta l = u_c \delta t$. The mass of the fluid (per unit length) accumulated in the rim during that time is $\delta m = \rho H \delta l$.

of puncture. Dupré incorrectly deduced the retraction speed of the film, based on the erroneous assumption that the surface energy lost due to retraction is converted purely into kinetic energy:

$$\frac{1}{2}\pi \rho r^2 H U^2 = 2\gamma \pi r^2 \Rightarrow U = \sqrt{\frac{4\gamma}{\rho H}} \, , \qquad (1.6)$$

where H is the thickness of the film.

Culick [31] and Taylor [114] independently corrected Dupré's calculation using an argument based on the conservation of momentum of the film. In particular, they assumed that the motion is resisted by inertia and that the fluid collects in a rim moving at a constant speed. The film preceding the rim is assumed to be at rest; therefore the force balance on the rim may be expressed as a balance between the rate of change of rim momentum and the curvature force exerted on the rim:

$$\frac{dP}{dt} = u_c \frac{dm}{dt} = 2\gamma \, , \qquad (1.7)$$

where u_c is the constant rim speed and m the rim mass per unit length (see figure 1-3). The rate of change of the mass of the rim satisfies

$$\frac{dm}{dt} = \rho H u_c \, , \qquad (1.8)$$

where H is the sheet thickness, assumed to be uniform. Henceforth the constant speed

14

found from equations (1.7) and (1.8)

$$u_c = \sqrt{\frac{2\gamma}{\rho H}} \qquad (1.9)$$

became known as the Taylor-Culick speed. McEntee & Mysels [77] confirmed experimentally the Culick-Taylor theory for soap films of thickness greater than $0.1\mu m$. In 1983, Keller [64] extended the previous work of Taylor and Culick by considering sheets of non-uniform thickness. In collaboration with Miksis [63], Keller also considered time-dependent inviscid potential flows in which a wedge-shaped initial free surface profile admits self-similar solutions.

It is not immediately apparent why an energy balance yields an incorrect result. However, as we will see in section 4.2, viscous dissipation must be taken into account, no matter how small the fluid viscosity. Nevertheless, viscosity does not appear explicitly in the expression for u_c; rather, its presence essentially dictates how the fluid momentum is distributed within the film and whether capillary waves can exist.

While the bulk of experiments on retracting fluid sheets have been conducted with water sheets in air or with soap films, Debrégeas et $al.$ ([35],[36]) presented a series of experiments using films whose viscosity was of the order of one million times that of water. In particular they used polymer PDMS films obtained by a novel technique in which the film was created by initially dipping a ring in an isopentane solution of the polymer. After lifting the ring from the solution, the solvent evaporated, leaving behind a suspended film of pure PDMS of thickness of the order of $10\text{-}50\mu m$, much thicker than a typical soap film, which is less than $1\mu m$ thick. Accurate measurements of the retraction process revealed behavior that was markedly different from that predicted by inviscid theory. In particular, they found that the fluid no longer collects in a rim as it retracts. Moreover, the rim does not retract at a constant speed; rather the hole radius grows exponentially as:

$$R = R_0 e^{t/(1.4\tau)} \ , \qquad (1.10)$$

where $\tau = \mu H / 2\gamma$, with R_0 being the initial hole size and μ the film's dynamic viscosity. The exponential hole growth was also supported by a simple theoretical argument they provided (see § 5.2), by assuming that the surface energy gained is dissipated through the action of viscosity, but the exponent in the exponential was different from that observed.

The experimental studies of Dalnoki *et al.* [32] and Roth *et al.* [99] that succeeded the work of Debrégeas *et al.* used film rupture as a means to measure the viscosity of molten polystyrene films.

By applying Buckingham's Π-theorem, one may identify the single dimensionless control parameter concerning sheet retraction, the Ohnesorge number, defined as:

$$\mathrm{Oh} = \frac{\mu}{\sqrt{2H\rho\gamma}} \, ,\tag{1.11}$$

that essentially expresses the relative importance of viscous resistance to surface tension forces. It can also be seen as the Reynolds number of the flow if one takes u_c as the characteristic speed. Thus the Ohnesorge number for the soap films explored in the early experiments (e.g. [92], [77]) ranges from 0.01 to 1 when the thickness of the film is in the range $0.1 - 1\mu m$, whereas for the PDMS fluid in the experiments of Debrégeas *et al.* Oh ranges from 10^4 to 10^5. One of the goals of the thesis is to develop a theory for sheet retraction valid for all Oh.

Following the work of Debrégeas *et al.*, Brenner & Gueyffier [13] studied the retraction of a two-dimensional sheet numerically, by using a one-dimensional Trouton-type lubrication model from which they were able to identify 3 distinct regimes depending on the Ohnesorge number. In the low Oh regime (Oh < 0.1), they found that capillary wave disturbances are generated ahead of the retracting rim. As the Ohnesorge number is increased, the capillary waves disappear and the rim starts diffusing towards the bulk of the sheet. Finally in the high Oh regime (Oh ≫ 10), they found that no rim forms at all, in accord with Debrégeas' observations. In all cases considered, the fluid was observed to approach the Culick-Taylor speed in the long time limit. Their work however did not report on the acceleration phase of the film, which was examined later by Sünderhauf *et al.* [111], via two-dimensional numerical simulations. Critically, their model was not able to capture the exponential regime observed by Debrégeas *et al.*, a shortcoming they attributed to the different geometry considered (2D planar vs Circular). In Chapters 4 and 5, we shall elaborate on the retraction dynamics of flat sheets by building upon Brenner's & Gueyffier's work, to clarify the effects of viscosity and geometry by solving the appropriate Trouton-type model for both planar and circular geometries.

The retraction dynamics are greatly affected if the film is embedded in a viscous envi-

ronment, as was demonstrated in the studies of Joanny & de Gennes [62] and Reyssat & Queré [91]. The experimental work of Reyssat & Queré involved the bursting of soap films embedded in viscous oils, typically with viscosity 20 to 1000 times that of water. Even though the fluid is collected in a rim as it retracts, in accordance with the bursting of films in air, the retraction process is limited by the friction arising from the viscous environment. The retraction speed is not given by equation (1.9); rather, it satisfies the implicit relation:

$$V = \frac{\gamma}{2\pi\mu} \ln\left(\frac{4\mu}{V\rho r}\right) , \qquad (1.12)$$

found by balancing the curvature force with the viscous force on the cylindrical rim, determined via the Oseen approximation, with r being the radius of the toroidal rim and μ the viscosity of the ambient fluid. Given that r is time-dependent, V should also depend on time. However this dependence was found to be weak, in agreement with experimental observations.

When the fluid film is extremely thin (typically of the order of 100-1000 $\mathring{A}$), sheet rupture can be affected by van der Waals forces, [106]. These attractive, long-range molecular forces can cause the nucleation of holes when the free-surface is perturbed. Using the model of Erneux and Davis [44] on planar sheets, Ida and Miksis [60] identified a similarity form for the film thickness and found that when a perturbation is introduced in the film, van Der Waals forces and viscous forces dominate over inertial and surface tension effects and eventually lead to film rupture. By extending this work, Vaynblat et al. [121], examined axisymmetric point rupture and found that the film thins according to $\tau^{1/3}$, where τ is the time remaining to rupture.

Savart's experiments [102] on the oblique collision of identical jets, a configuration also known to produce flat sheets, have been pursued by a number of investigators with the intention of elucidating the atomization and breakup characteristics of the resulting sheets. Such configuration is applicable in fuel atomization in combustion engines [1]. By varying the flow conditions, one may observe a wide variety of structures, ranging from steady to violently flapping and quickly disintegrating sheets (see figure 1-4). As reported by a number of authors (e.g. [58], [17], [12]), flow conditions exist for which a steady leaf-shaped sheet is formed, bound by a rim normal to the plane of incidence of the jets. Multiple such leaves of progressively smaller size can coexist downstream and be mutually orthogonal,

17
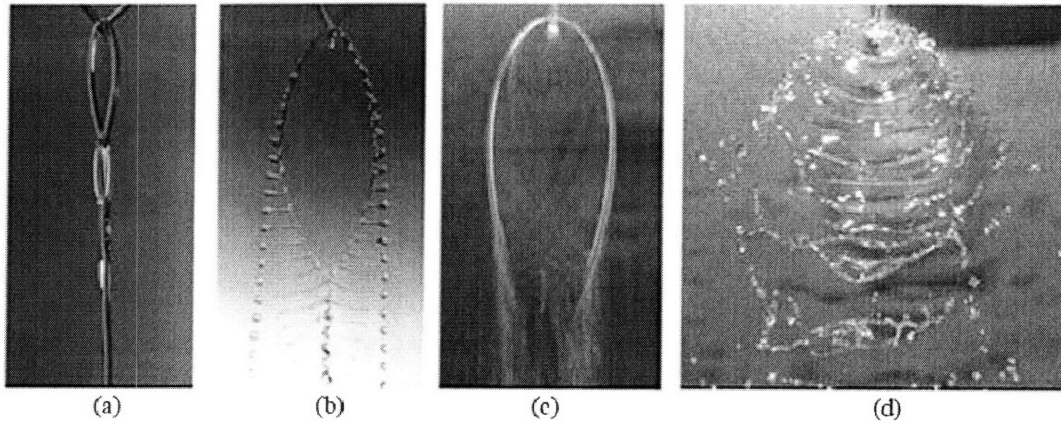
Figure 1-4: Flow structures observed for the colliding jets (taken from Bush & Hasha [17]).

resembling a chain.

Hasson & Peck [54] provided a theoretical model that gives the thickness distribution over the film, Bush & Hasha [17] provided a generalized version of Taylor's work [115] to predict the shape of the leaf and presented a detailed parameter scan indicating the regimes where each of the various structures can be observed. Most importantly, they identified that the instability of the rim (figure 1-4b) can be rationalized by the Rayleigh-Plateau instability. Experimental work focusing on the high We regime, where sheets disintegrate by flapping can be found for example in Fraser & Dombrowski [38] and Dombrowski & Hooper [39]. More recently, Bremond & Villermaux [12] explored further the issue of atomization and how the conditions near the source can affect the dynamics and the droplet size distributions.

When either the angle of ejection is not 90^0 or the Froude number criterion, equation (1.1), does not hold, a jet impinging on an impactor gives rise to the so called fluid-bells (see figure 1-5). These shapes were initially observed by Savart in [100] and [101] and theoretically studied in 1869 by Boussinesq ([10], [11]), who deduced the equations of the stationary bells. The bells close due to the azimuthal curvature and their shapes are essentially prescribed by the balance of inertial, gravitational and curvature forces. The excellent agreement between theory and experiment prompted Bond [9] to use the fluid bells to measure the surface tension of water. Similar experiments by Hopwood [55], revealed that a pressure difference between the interior of the bell and the surroundings generally alters the

18
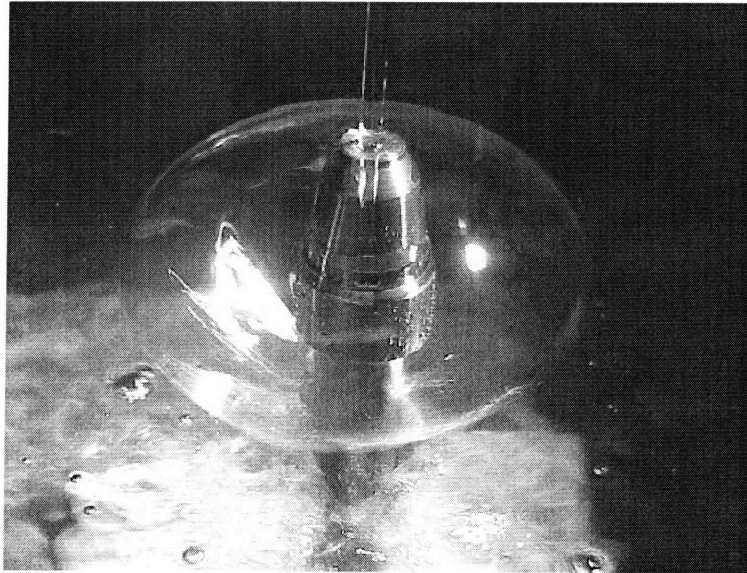
Figure 1-5: A fluid bell (taken from Buckingham & Bush [16])

bell shapes, and can also lead to their destabilization and destruction. Further theoretical studies were conducted by Lance & Perry [70], who performed numerical computations and noted that when the pressure difference inside the bell is sufficiently high, the solutions obtained yield unphysical, self-intersecting shapes, thus suggesting the apparent breakdown of the Boussinesq theory. Experiments in the regime where the Boussinesq theory yields these self-intersecting shapes, indicate that the bells tend to form cusps, but to date no theory exists that describes these shapes [27]. In another study, Taylor [112] computed a correction term that takes into account the motion of the ambient air, whereas Parlange [83] focused on the air motion inside the bell, induced by the moving fluid. In general however, the corrections in speed due to, respectively, air drag and aerodynamic pressures, are of the order of a few percent and so generally negligible in a laboratory setting [112].

Clanet [24] and Aristoff *et al.* [3], identified a regime where the bells become unstable by progressively decreasing the flow rate of the impinging jet. This process gradually increases the pressure inside the closed bell and eventually results in the bell bursting and the subsequent formation of a smaller stable bell. These studies also identified regimes in which self-sustained periodic oscillations can occur at constant flow rate, when the angle of ejection is close to 90^0. During this process the bell alternates between being concave up and down (see figure 1-6). In a follow-up paper, Clanet [25], studied the detachment

19
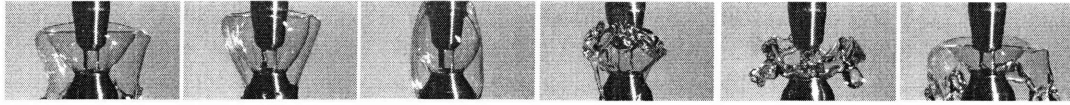
Figure 1-6: Self-sustained oscillations of bells at constant flow rate (Aristoff *et al.* [3]).
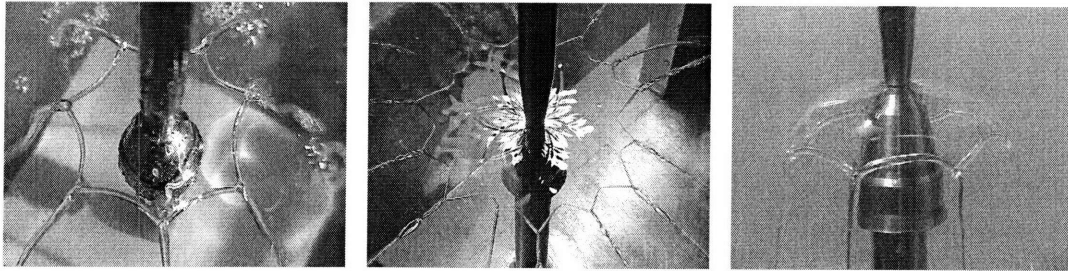
Figure 1-7: Symmetry breaking in fluid sheets with viscosities 10 - 20cS (taken from Buckingham & Bush [16]).

of the film from the impactor and the dependence of the maximum angle of ejection ψ (see figure 3-1) on the flow parameters. In all these experiments, symmetry was preserved. However as shown in a series of experiments by Buckingham & Bush [16], the attainable shapes depend on both the fluid viscosity and the source conditions, which may break the symmetry yielding a variety of fascinating polygonal and polyhedral forms (see figure 1-7).

Bark *et al.* [5] presented a combined experimental and theoretical investigation of the effects of rotation on the bell shapes. Here the phenomenon is markedly different, since the presence of the centripetal forces prevents the closing of the bells downstream. As the bell tends to close due to surface tension, conservation of angular momentum dictates that large swirl velocities and hence large centripetal forces be generated that cause the fluid to be flung outwards. Inviscid theory suggests that there should exist infinitely many necks downstream, something that is not observed experimentally. The bells instead tend to disintegrate, typically before the second or third neck forms, which can be attributed to viscous dissipation and the Kelvin-Helmholtz instability. A related mechanism aimed at producing small metal particles was introduced by Gasser & Marty [51], who proposed the use of a rotating magnetic field to set liquid metal sheets into a swirling motion. The sheets produced by this procedure will ultimately disintegrate to yield the desired particles, of characteristic size $50\mu m$.

A liquid film falling under the influence of gravity is susceptible to a number of instabilities. Various aspects of the dynamics of falling liquid films have been investigated owing largely to its applications in curtain coating (e.g. [14], [33], [34], [46], [73] and [74]). Teng *et al.* [119], motivated by earlier experiments by Lin & Roberts [73], studied the linear stability of a viscous film falling between two viscous gases. Taking into account the destabilizing effect of the ambient gas, they showed that the critical Weber number above which the flow is convectively unstable is approximately unity in accordance with Taylor's earlier predictions [116] for a sheet in inviscid ambient, but for We < 1 they found that the flow is absolutely unstable. Conversely, Taylor's earlier work on sheets, where he neglected the ambient air, predicted the flow to be neutrally stable in this low We limit. Le Grand *et al.* [71] discovered experimentally a new type of instability that gives rise to a striking checkerboard pattern on the film. As the film falls from a smoothly curved substrate instead of a slot, transverse motions are generated within the sheet and ultimately yield this wave-induced pattern.

The dynamics of a falling liquid film in the viscous limit are qualitatively different from those of its low viscosity counterpart. In particular, it is observed that the film folds itself in a regular, periodic manner, just as happens when honey is poured on toast. In an industrial setting, this folding instability can be observed during the commercial filling of containers, with, for example, paint. Detailed experiments of this phenomenon were first carried out by Cruickshank & Munson [29], who later investigated the linear theory of the problem [30]. Yarin & Tchavdarov [129] also employed linear theory to study this instability, but its applicability was restricted to the onset of folding. The inertia-free models of Skorobogatiy & Mahadevan [107] and Ribe [97], yielded scalings for the folding amplitude and frequency that were supported by experiments. Nevertheless these models showed only qualitative agreement with the experiments. As Ribe pointed out, the discrepancy in frequency of up to a factor of 2 with the experimental data, can be amended by either including the inertial terms or the surface tension effects near the edges of the film that tend to reduce its width downstream. This mechanism is quite similar to that arising in the recently reported experiments of Chiu-Webster & Lister [23], who examined the fascinating shapes attained by coiling and folding when a viscous thread falls onto a moving surface, the 'fluid mechanical sewing machine'.

In comparison to the wealth of inviscid models to describe thin film dynamics, the

theory of viscous films is much less developed. In many situations, the inclusion of viscosity is critical. The first study of a viscously dominated thin film flow was that of Pearson & Petrie ([85] and [86]), who were motivated by an interest in thin-film blowing, wherein film deformations are induced by a pressure difference applied between at the film boundaries.

Fliert *et al.* [45] developed general equations for unsteady films of arbitrary shape, using an asymptotic expansion in terms of the aspect ratio of the film, namely the ratio of its characteristic thickness to length. This work is essentially a generalization of the work of Pearson & Petrie who presented the governing equations in the axisymmetric, static case, and the model of Yarin *et al.* [128], who considered the unsteady axisymmetric case and applied it to the problem of hollow fiber drawing. Fliert *et al.* developed this general formulation and then applied it to the special case of the blowing of a two-dimensional viscous sheet, in which inertial effects are negligible. A mistake in their formulation is corrected in Chapter 3.

More recently, Ribe [96] generalized the previous two-dimensional theories by Buckmaster, Nachman & Ting [15] and Ribe [95] to allow for consideration of sheet dynamics in arbitrary geometries. The difference between the models of Ribe [96] and Fliert *et al.* [45] lies in the form of the governing equations and how they are obtained. By closely following the elastic theory of shells [53], Ribe integrates the 3 dimensional flows across the film, thus obtaining a set of equations that depend on integrals involving the stress elements, the bending and stretching moments. While this approach yields better results than the asymptotic expansion of Fliert *et al.* [95], this technique cannot be utilized when inertial terms are significant, due to the nonlinearity they introduce. Lastly, Ida & Miksis [61] considered the evolution equations for thin sheets with the effects of van der Waals forces, inertia and surfactants present; however, their model scaling resulted in the inertial terms and viscous terms of the normal momentum equations being incorrectly dropped. The inclusion of inertia and surface tension contributions arising from the curvatures of the bounding interfaces of the film not being exactly equal are taken into account in Chapters 2 and 3. These curvature effects are expected to become appreciable for sheets with sharp curvature and/or rapidly varying thickness, as for example in retracting sheets, bells and sheets with rims.

In principle, numerical simulations of the fully three-dimensional equations that govern the thin film flows are somewhat impractical, especially if there is a large difference between

the sheet thickness and length. For instance, in a situation where the film thickness is many orders of magnitude smaller than the characteristic sheet length, successful resolution of the governing equations would require an extremely fine discretization in the vicinity of the film, especially if the ambient fluid is taken into account. In cases where the ambient fluid can be assumed to be dynamically insignificant, efficiency can be improved, by using, say, a boundary fitted method (e.g. [18], [81]).

As demonstrated by numerical tests by Ribe [95] and Mehring & Sirignano [78] and corroborated by numerous experimental data, reducing the dimension of the problem by taking the motions normal to the film to be smaller relative to the tangential speeds, yields reasonably good descriptions of the dynamics. For this reason, the majority of the literature is devoted to techniques reducing the complicated, three-dimensional problem into a lower one- or two-dimensional system. The current thesis contributes in this direction, by presenting a general framework upon which one can build lower dimensional models to study thin film flows.

1.2 Thesis outline

We here present the results of a theoretical investigation of the dynamics of thin viscous sheets. We begin in Chapter 2 by introducing the notation and the differential geometric concepts necessary for deriving the equations of motion on a curved geometry for an arbitrary coordinate system, whose basis is not necessarily orthonormal. Particular attention is given to including the inertial terms, which have not been previously considered, apart from the special case of curvilinear coordinates. Such a formal treatment is most valuable when one considers fully three-dimensional simulations by using an appropriate boundary-fitted numerical technique. The more compact-looking equations for a curvilinear coordinate system are less advantageous for arbitrarily shaped thin films, since remeshing of the equations would be required at each timestep. In the remainder of the thesis we focus on relatively simple cases, where the film exhibits certain symmetries.

In Chapter 3, we consider the dynamics of a slender sheet of viscous fluid, in geometries where it is convenient to employ a curvilinear coordinate system. Using an asymptotic expansion, we find the leading order equations, which, together with the appropriate free-surface conditions, yield a model that reduces the equations from three to two dimensional.

The surface tension contributions arising from the variations in the fluid thickness are also included, which become important near the edge of the film. Further reduction of the equations for two-dimensional or axisymmetric sheets reduce the resulting equations to a set of coupled one-dimensional, time-dependent partial differential equations.

In Chapters 4 and 5, we present the application of the general theory developed in the previous chapters to the bursting of flat viscous sheets. In particular, we consider both the two-dimensional, planar film (Chapter 4) and the axisymmetric, circular film (Chapter 5), and present a combined analytical and numerical investigation of their dynamics. We extend prior work on the subject through rationalizing the experimental observations of Debrégeas *et al.* [35] on the bursting of very viscous sheets. We conclude in Chapter 6, by discussing the implications of our work and proposing directions for future research on the dynamics of thin films.

Chapter 2

Notation and general formulation

In this chapter we present the equations that govern the motion of fluid sheets through a formal differential geometric and fluid mechanical treatment. We model the fluid as Newtonian and incompressible, but this treatment can also be extended to allow for fluids of different characteristics. To do so we require a brief review of the concepts borrowed from differential geometry that are essential to describing the Navier Stokes equation on a curved film. This introduction to the notation used throughout makes up most of §2.1. In the subsequent sections 2.2-2.3 we extend the prior work done on fluid sheets (e.g. [56],[45] and [96]), to include terms arising from inertia and the variation of the sheet thickness. We conclude in §2.4 by presenting the appropriate boundary conditions.

In what follows, superscripts and subscripts are used to label contravariant and covariant quantities respectively. Greek indices take the values 1 and 2 whereas the Latin indices take the values 1,2 and 3. Summation is assumed for repeated indices unless otherwise stated. This notation is abandoned in subsequent chapters when we turn our attention to simpler geometries.

2.1 Notation and concepts from differential geometry and tensor calculus

2.1.1 Differential geometry of surfaces

Our discussion is limited to regular surfaces $\mathbf{r}_0 \left(x_1, x_2 \right)$ defined on a set $U \subseteq \mathbb{R}^2$ such that $\mathbf{r}_0 : U \to \mathbb{R}^3$. Such a surface is called regular if it is smooth and the vectors $\partial_{x_1} \mathbf{r}_0$ and
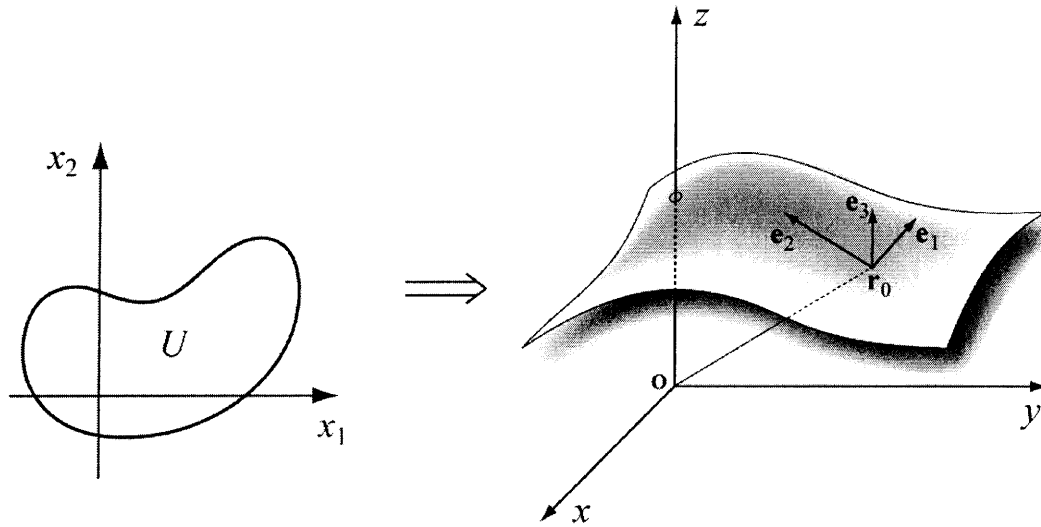
Figure 2-1: Geometry of a surface in $\mathbb{R}^3$.

$\partial_{x_2}\mathbf{r}_0$ are linearly independent at all points $(x_1, x_2) \in U$. Here we use $\partial_{x_i}\mathbf{r}_0$ to denote partial differentiation of $\mathbf{r}_0$ with respect to x_i. Equivalently, $\mathbf{r}_0$ should be smooth and the vector product $\partial_{x_1}\mathbf{r}_0 \times \partial_{x_2}\mathbf{r}_0$ should be non-zero at every point of U. This last statement implies that a normal at each point on the surface is well-defined.

We proceed with a presentation of the tools needed for defining the differential operators on a surface which will eventually allow us to formulate the Navier Stokes equations on a surface. In our treatment, we omit all proofs and introduce notation only as needed to derive the equations. The details can be found in the excellent texts on differential geometry by Pressley [89] and Do Carmo [37].

The vectors

$$\mathbf{e}_\alpha = \partial_{x_\alpha}\mathbf{r}_0 \tag{2.1}$$

correspond to the *covariant* tangent vectors of the surface. The unit normal vector $\mathbf{e}_3$ is:

$$\mathbf{e}_3 = \hat{\mathbf{n}} = \frac{\mathbf{e}_1 \times \mathbf{e}_2}{|\mathbf{e}_1 \times \mathbf{e}_2|}. \tag{2.2}$$

Because the chosen coordinate system (x_1, x_2) may not be orthonormal, one may define a

$$\| \mathbf{e}^\beta \| = \frac{1}{\| \mathbf{e}_\beta \| \sin \theta}$$
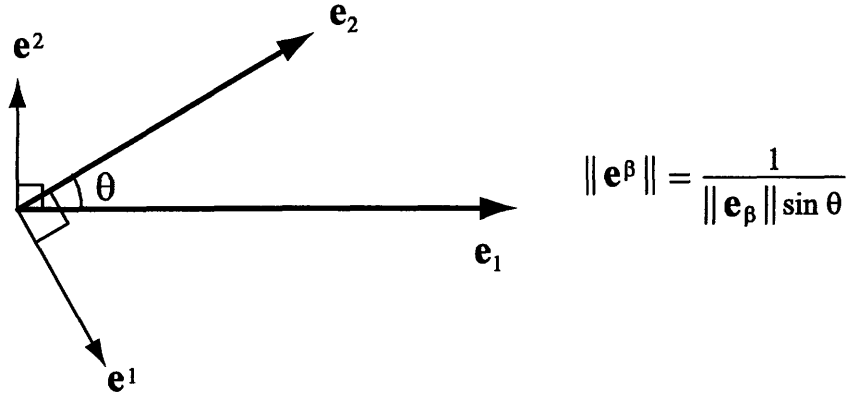
Figure 2-2: Covariant and contravariant vectors in two dimensions.

set of *contravariant* vectors $\mathbf{e}^\beta$ that satisfy

$$\mathbf{e}_\alpha \cdot \mathbf{e}^\beta = \delta_\alpha^\beta \ , \tag{2.3}$$

where δ_α^β corresponds to the Kronecker delta. An explicit expression for these reciprocal basis vectors can be computed using

$$\mathbf{e}^1 = \frac{\mathbf{e}_2 \times \mathbf{e}_3}{a}, \quad \mathbf{e}^2 = \frac{\mathbf{e}_3 \times \mathbf{e}_1}{a} \text{ and } \mathbf{e}^3 = \mathbf{e}_3 \ , \tag{2.4}$$

where $a = \mathbf{e}_1 \cdot (\mathbf{e}_2 \times \mathbf{e}_3)$.

Another important concept from the differential geometry of surfaces is to define a means of computing arc-lengths of curves lying on the surface $\mathbf{r}_0$. If we define a curve $\mathbf{c}(t) = \mathbf{r}_0(x_1(t), x_2(t))$, its arc-length s starting from a point $\mathbf{c}(t_0)$ to a point $\mathbf{c}(t_1)$ is found using

$$s = \int_{t_0}^{t_1} \| \dot{\mathbf{c}}(\tau) \| \, d\tau = \int_{t_0}^{t_1} \left(a_{11} (\dot{x}_1)^2 + a_{12} \dot{x}_1 \dot{x}_2 + a_{22} (\dot{x}_2)^2 \right) d\tau \ . \tag{2.5}$$

The expression $\left(a_{11} (\dot{x}_1)^2 + a_{12} \dot{x}_1 \dot{x}_2 + a_{22} (\dot{x}_2)^2 \right)$ is termed the *first fundamental form*, where the coefficients a_{11}, a_{22} and $a_{12} = a_{21}$ constitute the metric tensor of the surface and are given by

$$a_{\eta\beta} = \mathbf{e}_\eta \cdot \mathbf{e}_\beta \ . \tag{2.6}$$

Just as the first fundamental form characterizes the arc-length of curves that lie on $\mathbf{r}_0$, the *second fundamental form* characterizes the curvature of a surface. To introduce this notion, we perturb the surface $\mathbf{r}_0\left(x_1, x_2\right)$ to $\mathbf{r}_0\left(x_1 + \Delta x_1, x_2 + \Delta x_2\right)$ which moves the surface away from its tangent plane at $\mathbf{r}_0\left(x_1, x_2\right)$ by a distance

$$
\begin{aligned}
\left(\mathbf{r}_0\left(x_1 + \Delta x_1, x_2 + \Delta x_2\right) - \mathbf{r}_0\left(x_1, x_2\right)\right) \cdot \mathbf{e}_3 & \\
\simeq \left[\mathbf{e}_\alpha \Delta x_\alpha + \frac{1}{2}\left(\left(\Delta x_1\right)^2 \partial_{x_1}\partial_{x_1}\mathbf{r}_0 + 2\Delta x_1\Delta x_2\partial_{x_1}\partial_{x_2}\mathbf{r}_0 + \left(\Delta x_2\right)^2 \partial_{x_2}\partial_{x_2}\mathbf{r}_0\right) + ...\right] \cdot \mathbf{e}_3 & \\
\simeq \frac{1}{2}\left(b_{11}\left(\Delta x_1\right)^2 + 2b_{12}\Delta x_1\Delta x_2 + b_{22}\left(\Delta x_2\right)^2\right) . &
\end{aligned}
\tag{2.7}
$$

This last result is the analogue for the curvature term $\kappa\left(\Delta t\right)^2$ in the case of a curve $\mathbf{c}\left(t\right)$. Here we define the coefficients of the second fundamental form, the curvature tensor $b_{\alpha\beta}$ as:

$$
b_{\alpha\beta} = \mathbf{e}_3 \cdot \partial_{x_\alpha}\mathbf{e}_\beta .
\tag{2.8}
$$

In addition to this formalism, it is of interest to know how the tangent vectors vary as we move along the surface. To do so we define the 6 *Christoffel symbols* $\Gamma^\eta_{\alpha\beta}$ by

$$
\partial_{x_\alpha}\mathbf{e}_\beta = \Gamma^\eta_{\alpha\beta}\mathbf{e}_\eta + b_{\alpha\beta}\mathbf{e}_3 .
\tag{2.9}
$$

These are given explicitly by:

$$
\Gamma^1_{11} = \frac{1}{2a}\left(a_{22}\partial_{x_1}a_{11} - 2a_{12}\partial_{x_1}a_{12} + a_{12}\partial_{x_2}a_{11}\right) ,
\tag{2.10}
$$

$$
\Gamma^2_{11} = \frac{1}{2a}\left(2a_{11}\partial_{x_1}a_{12} - a_{11}\partial_{x_2}a_{11} - a_{12}\partial_{x_1}a_{11}\right) ,
\tag{2.11}
$$

$$
\Gamma^1_{12} = \frac{1}{2a}\left(a_{22}\partial_{x_2}a_{11} - a_{12}\partial_{x_1}a_{22}\right) ,
\tag{2.12}
$$

$$
\Gamma^2_{12} = \frac{1}{2a}\left(a_{11}\partial_{x_1}a_{22} - a_{12}\partial_{x_2}a_{11}\right) ,
\tag{2.13}
$$

$$
\Gamma^1_{22} = \frac{1}{2a}\left(2a_{22}\partial_{x_2}a_{12} - a_{22}\partial_{x_1}a_{22} - a_{12}\partial_{x_2}a_{22}\right) ,
\tag{2.14}
$$

$$
\Gamma^2_{22} = \frac{1}{2a}\left(a_{11}\partial_{x_2}a_{22} - 2a_{12}\partial_{x_2}a_{12} + a_{12}\partial_{x_1}a_{22}\right) ,
\tag{2.15}
$$

where $a = a_{11}a_{22} - a_{12}a_{21}$. Of equal importance are the derivatives of the normal vectors along the surface:

$$
\partial_{x_\alpha}\mathbf{e}_3 = -b^\beta_\alpha\mathbf{e}_\beta ,
\tag{2.16}
$$

28

where

$$b_1^1 = \frac{b_{11}a_{22} - b_{12}a_{12}}{a}, \quad b_1^2 = \frac{b_{12}a_{11} - b_{11}a_{12}}{a}, \tag{2.17}$$

$$b_2^1 = \frac{b_{12}a_{22} - b_{22}a_{12}}{a}, \quad b_2^2 = \frac{b_{22}a_{11} - b_{12}a_{12}}{a}. \tag{2.18}$$

We conclude by defining the mean and Gaussian curvatures of the surface. Letting κ_1 and κ_2 be the principal curvatures of the surface, its Gaussian curvature is

$$K = \kappa_1 \kappa_2 = a \left(b_1^1 b_2^2 - b_1^2 b_2^1 \right) = \frac{b_{11}b_{22} - b_{12}b_{21}}{a_{11}a_{22} - a_{12}a_{21}} \tag{2.19}$$

and its mean curvature is:

$$H = \frac{1}{2} \left(\kappa_1 + \kappa_2 \right) = -\frac{1}{2} \nabla_s \cdot \hat{\mathbf{n}} = -\frac{1}{2} \left(b_1^1 + b_2^2 \right) = \frac{a_{22}b_{11} - 2a_{12}b_{12} + a_{11}b_{22}}{2a}. \tag{2.20}$$

The principal curvatures are:

$$\kappa_{1,2} = H \pm \sqrt{H^2 - K}. \tag{2.21}$$

2.1.2 Covariant differentiation

In deriving the equations of motion, we need to express how the hydrodynamic quantities vary as the fluid particles move along the surface. To do this, the notion of the *covariant derivative* of a vector or tensor component with respect to the surface coordinates x_α needs to be introduced. It essentially expresses the derivative of the vector, taking into account the change of the basis vectors from point to point. To illustrate these concepts, we go through the steps of deriving the derivative with respect to x_β of a vector field $\mathbf{F} = F^\alpha \mathbf{e}_\alpha$ defined on the surface $\mathbf{r}_0$:

$$\begin{aligned}
\partial_{x_\beta} \mathbf{F} &= \frac{\partial}{\partial x_\beta} \left(F^\alpha \mathbf{e}_\alpha \right) = \frac{\partial F^\alpha}{\partial x_\beta} \mathbf{e}_\alpha + F^\alpha \frac{\partial \mathbf{e}_\alpha}{\partial x_\beta} \\
&= \frac{\partial F^\alpha}{\partial x_\beta} \mathbf{e}_\alpha + F^\alpha \left(\Gamma_{\alpha\beta}^\gamma \mathbf{e}_\gamma + b_{\alpha\beta} \mathbf{e}_3 \right) \\
&= \left(\frac{\partial F^\alpha}{\partial x_\beta} + F^\gamma \Gamma_{\gamma\beta}^\alpha \right) \mathbf{e}_\alpha + F^\alpha b_{\alpha\beta} \mathbf{e}_3 \\
&= F_{,\beta}^\alpha \mathbf{e}_\alpha + F^\alpha \mathbf{e}_{\alpha,\beta},
\end{aligned} \tag{2.22}$$

29
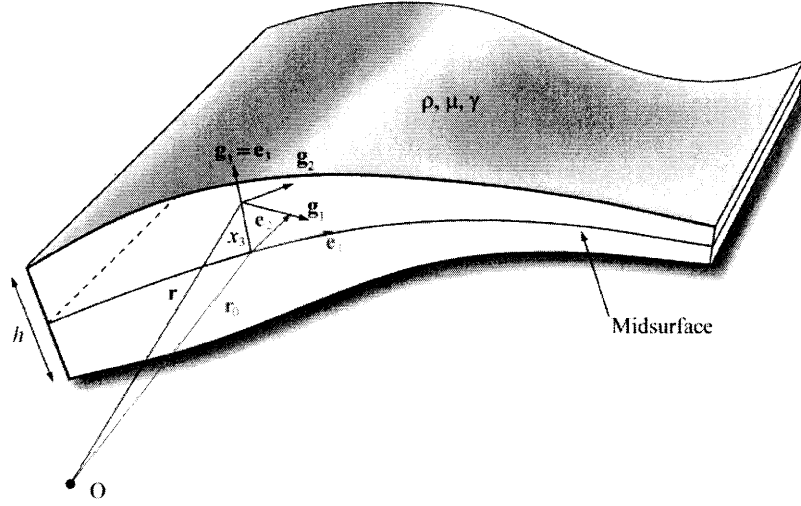
Figure 2-3: Definition sketch of the thin film model. The basis vectors $\mathbf{g}_\alpha$ of the coordinate system defined in (2.25) are essentialy rotations of the corresponding tangent vectors of the surface $\mathbf{e}_\alpha$.

where we made use of equation (2.9) in the second step. The quantities

$$F^\alpha\big|_\beta = \frac{\partial F^\alpha}{\partial x_\beta} + F^\gamma \Gamma^\alpha_{\gamma\beta} \ , \tag{2.23}$$

$$\mathbf{e}_\alpha\big|_\beta = b_{\alpha\beta}\mathbf{e}_3 \tag{2.24}$$

denote the covariant derivatives of the components of the vector field and the basis vectors respectively. Similar expressions may be derived for the components of vectors and tensors and can be found in Chapter 1 of the book by Green and Zerna [53].

2.2 Problem geometry

We consider the motion of a slender fluid sheet of dynamic viscosity μ, density ρ variable thickness h and surface tension γ. The motion of the ambient fluid is neglected in this analysis. Following the prior work on the subject such as [96] and [45], we describe the underlying dynamics by choosing a coordinate system that moves with the sheet. For this reason we define the 'midsurface' $\mathbf{r}_0\,(x_1, x_2, t)$ to be the surface whose normals intersect the bounding surfaces at equal distances $h/2$ (see fig 2.3). Here x_1 and x_2 are the coordinates of $\mathbf{r}_0$ and $x_3 \in \left[-\frac{1}{2}h, \frac{1}{2}h\right]$ is the normal distance from $\mathbf{r}_0$.

30

This allows us to define the position vector $\mathbf{r}\left(x_1, x_2, x_3, t\right)$ of a fluid particle within the sheet as

$$\mathbf{r} = \mathbf{r}_0 + x_3 \mathbf{e}_3 \ , \quad x_3 \in \left[-\tfrac{1}{2}h, \tfrac{1}{2}h\right] \ , \tag{2.25}$$

where as usual $\mathbf{e}_3$ is the (unit) normal vector to the surface. Since points that do not lie on $\mathbf{r}_0$ do not share the same vectors $\mathbf{e}_i$ we use the formalism and notation developed in §2.1 for surfaces to define the contravariant $\mathbf{g}_i$ and covariant $\mathbf{g}^i$ base vectors associated with the coordinate system (2.25) as

$$\mathbf{g}_\alpha = \partial_\alpha \mathbf{r} = q_\alpha^\gamma \mathbf{e}_\gamma \ , \quad \mathbf{g}_3 = \mathbf{g}^3 = \mathbf{e}_3 \quad \text{and} \quad \mathbf{g}^\alpha = \frac{\left(q_\rho^\rho \delta_\lambda^\alpha - q_\lambda^\alpha\right)}{q_1^1 q_2^2 - q_1^2 q_2^1} \mathbf{e}^\lambda \ , \tag{2.26}$$

where

$$q_\alpha^\gamma = \delta_\alpha^\gamma - x_3 b_\alpha^\gamma \ . \tag{2.27}$$

Since the vectors $\mathbf{g}_\alpha$ and $\mathbf{e}_\alpha$ share the same normal vector, it is easy to see that the $\mathbf{g}_\alpha$ are obtained through rotations on the vectors $\mathbf{e}_\alpha$. These vectors constitute dual bases, meaning that they satisfy:

$$\mathbf{g}_i \cdot \mathbf{g}^j = \delta_i^j \ . \tag{2.28}$$

As in the case of surfaces, we also define the covariant and contravariant components of the metric tensor

$$g_{ij} = \mathbf{g}_i \cdot \mathbf{g}_j \ , \quad g^{ij} = \mathbf{g}^i \cdot \mathbf{g}^j \ . \tag{2.29}$$

Finally, an important set of equations that we need to use to simplify the equations later on is:

$$\frac{\partial \mathbf{g}_\beta}{\partial x_\alpha} = \left(\frac{\partial q_\beta^\gamma}{\partial x_\alpha} + q_\beta^\lambda \Gamma_{\alpha\lambda}^\gamma\right) \mathbf{e}_\gamma + b_{\alpha\lambda} q_\beta^\lambda \mathbf{e}_3 \ , \tag{2.30}$$

$$\frac{\partial \mathbf{g}_3}{\partial x_\alpha} = \frac{\partial \mathbf{g}_\alpha}{\partial x_3} = -b_\alpha^\beta \mathbf{e}_\beta. \tag{2.31}$$

Here we note that the vectors are *not* assumed to be either of unit length or orthogonal. The advantage of this more general description lies in the fact that the sheet may undergo large deformations and material coordinates that were initially orthogonal will not necessarily remain so at later times, thus requiring remeshing at each time step of the computation [96]. The elasticity theory of shells is built upon this theoretical framework (see

31

for example Green and Zerna [53]), where the velocities of the fluid particles correspond to the deformations of the elastic shell. The Reynolds number of the flow, which characterizes the relative importance of viscous and inertial forces, is defined as:

$$\mathbb{R}e = \frac{u_0 \ell}{\nu} \, ,$$

(2.32)

where $\nu = \mu/\rho$ is the kinematic viscosity of the fluid, ℓ is a characteristic lengthscale and u_0 a characteristic velocity. The governing equations in the low $\mathbb{R}e$ regime, where the inertial terms can be dropped, are directly analogous to the equations obeyed by an elastic shell in equilibrium. It is thus that Ribe developed the general theory for viscous sheets [96], by following closely the theory developed for elastic shells in equilibrium. In this case, integration of the Navier-Stokes equations across the sheet yield a set of equations for the total force and torque balance on the sheet. However, this procedure is not applicable in the more general case where inertia is present, due to the non-linearity introduced by the convective terms. Hence the standard lubrication approximation is performed, as we will see in the next chapter, where we investigate surfaces parametrized in curvilinear coordinates. In what follows, the general set of equations are presented; the leading order expansions for surfaces parametrized in curvilinear coordinates are to be presented in the next chapter.

2.3 Navier Stokes equations

Given the complexity of the calculation, we proceed by computing the individual components of the momentum equation:

$$\rho \, \frac{d\mathbf{v}}{dt} = \nabla \cdot \mathbf{T} + \mathbf{f}_{\text{body}} \, ,$$

(2.33)

where $\mathbf{v}$ is the velocity of the fluid particles, $\mathbf{T}$ corresponds to the stress tensor and $\mathbf{f}_{\text{body}}$ is the body force (e.g. gravity).

2.3.1 Inertial terms

Since the location of each fluid particle within the sheet is given by $\mathbf{r}$, the velocity of the fluid particles measured in the *laboratory frame* is:

$$\begin{aligned}
\mathbf{v} &= \frac{d\mathbf{r}}{dt} = v^i\mathbf{g}_i = v_i\mathbf{g}^i \\
&= \frac{\partial\mathbf{r}}{\partial t} + \frac{dx_i}{dt}\frac{\partial\mathbf{r}}{\partial x_i} \\
&= \frac{\partial\mathbf{r}}{\partial t} + u^i\mathbf{g}_i = \mathbf{w} + \mathbf{u} ,
\end{aligned} \tag{2.34}$$

where $\mathbf{w} = \partial\mathbf{r}/\partial t$ corresponds to the velocity that describes the motion of the coordinate system attached to the midsurface and $\mathbf{u} = u^i\mathbf{g}_i$ corresponds to the velocity as measured in this moving coordinate frame. Under this non-orthonormal coordinate system, the physical components of the velocity u^i_{phys} are related to the components u^i (no summation assumed over i) by:

$$\mathbf{u} = u^i\mathbf{g}_i = u^i_{\text{phys}}\hat{\mathbf{g}}_i \Rightarrow u^i_{\text{phys}} = u^i\sqrt{g_{ii}} . \tag{2.35}$$

In case the base vectors are not of unit length, the u^i would not correspond to velocities that are measurable in a laboratory setting, justifying our introduction of u^i_{phys}. Even though the geometries we will examine later preserve the orthogonality of the coordinate curves, we proceed in this more general setting for the sake of completeness. The acceleration term is now:

$$\begin{aligned}
\frac{d\mathbf{v}}{dt} &= \frac{\partial\mathbf{v}}{\partial t} + \frac{\partial\mathbf{v}}{\partial x_i}\frac{dx_i}{dt} = \frac{\partial\mathbf{v}}{\partial t} + u^i\frac{\partial}{\partial x_i}\left(\frac{\partial\mathbf{r}}{\partial t} + u^k\mathbf{g}_k\right) \\
&= \frac{\partial\mathbf{v}}{\partial t} + u^i\frac{\partial\mathbf{g}_i}{\partial t} + u^3\frac{\partial}{\partial x_3}\left(u^k\mathbf{g}_k\right) + u^\alpha\frac{\partial}{\partial x_\alpha}\left(u^\beta\mathbf{g}_\beta\right) + u^\alpha\frac{\partial}{\partial x_\alpha}\left(u^3\mathbf{g}_3\right) .
\end{aligned} \tag{2.36}$$

This may be expressed in terms of either the base vectors $\mathbf{g}_i$ or the surface vectors $\mathbf{e}_i$. In terms of the former:

$$\frac{d\mathbf{v}}{dt} = \left(\frac{\partial\mathbf{r}}{\partial t} + 2u^i\frac{\partial\mathbf{g}_i}{\partial t}\right) + \left(\frac{\partial u^i}{\partial t} + u^k\frac{\partial u^i}{\partial x_k} + u^m u^k\bar{\Gamma}^i_{mk}\right)\mathbf{g}_i . \tag{2.37}$$

Here $\bar{\Gamma}^i_{mk}$ are the Christoffel symbols of the coordinate system that satisfy (see [2] p. 165):

$$\frac{\partial\mathbf{g}_m}{\partial x_k} = \bar{\Gamma}^i_{mk}\mathbf{g}_i . \tag{2.38}$$

For a curvilinear coordinate system there are 27 such symbols, 15 of which are distinct and non-zero (for a surface we have only 6 as we saw in the previous section). The explicit computation of $\bar{\Gamma}^i_{mk}$ is shown in Appendix B. It is also worth noting that in case of a non-moving curvilinear coordinate system, the expression for the acceleration term that can be found in some introductory fluid mechanics textbooks (e.g. [6]) follow from the assumption of orthonormal base vectors. Identical expressions are obtained if we derive these expressions in terms of $\hat{\mathbf{g}}_i$ that are taken to be orthogonal. It is most useful to express the acceleration vector in terms of the surface vectors. Using equations (2.30) and (2.31) and after some tedious algebra, we obtain:

$$
\begin{aligned}
\frac{d\mathbf{v}}{dt} = A^i \mathbf{e}_i = & \frac{\partial^2 \mathbf{r}_0}{\partial t^2} + x_3 \frac{\partial^2 \mathbf{e}_3}{\partial t^2} + 2u^3 \frac{\partial \mathbf{e}_3}{\partial t} + 2u^\alpha q_\alpha^\gamma \frac{\partial \mathbf{e}_\gamma}{\partial t} \\
& + \left[q_\beta^\gamma \frac{\partial u^\beta}{\partial t} + 2u^\beta \frac{\partial q_\beta^\gamma}{\partial t} + u^\alpha \left(\frac{\partial \left(u^\beta q_\beta^\gamma \right)}{\partial x_\alpha} + \left(u^\beta q_\beta^\lambda \right) \Gamma^\gamma_{\alpha\lambda} \right) + u^3 \left(q_\beta^\gamma \frac{\partial u^\beta}{\partial x_3} - 2b_\alpha^\gamma u^\alpha \right) \right] \mathbf{e}_\gamma \\
& + \left(\frac{\partial u^3}{\partial t} + u^k \frac{\partial u^3}{\partial x_k} + u^\alpha u^\beta b_{\alpha\lambda} q_\beta^\lambda \right) \mathbf{e}_3 \ .
\end{aligned}
\tag{2.39}
$$

In general, the time derivatives of vectors in equations (2.37) and (2.39) cannot be expressed *a priori* in terms of the basis vectors $\mathbf{e}_i$ or $\mathbf{g}_i$ and should be projected onto the base vectors to obtain their respective components. In deriving equation (2.39), no simplifications are made apart from the assumption that a midsurface can be defined. These expressions are most suitable for three dimensional computations, but as we will see in the next chapter we can exploit the slenderness of the sheet to simplify the equations considerably.

2.3.2 Stress tensor

The constitutive relations for a Newtonian fluid in a general coordinate system are:

$$
\tau^{ij} = -pg^{ij} + 2\mu g^{ik} g^{jl} e_{kl} \ ,
$$

where p is the pressure of the fluid and e_{ij} is the strain rate tensor given by ([53], p.381)

$$e_{\alpha\beta} = \tfrac{1}{2}\left[q_\beta^\lambda\left(v_\lambda|_\alpha - b_{\lambda\alpha}v_3\right) + q_\alpha^\lambda\left(v_\lambda|_\alpha - b_{\lambda\beta}v_3\right)\right] , \tag{2.40}$$

$$e_{\alpha 3} = \partial_{x_\alpha}v_3 + \partial_{x_3}v_\alpha + b_\alpha^\lambda\left(v_\lambda - x_3\partial_{x_3}v_\lambda\right) , \tag{2.41}$$

$$e_{33} = \partial_{x_3}v_3 , \tag{2.42}$$

where the covariant derivatives $v_{\alpha,\beta}$ of the contravariant components of velocity can be found using ([53], p.38)

$$v_\lambda|_\alpha = \partial_{x_\alpha}v_\lambda - \Gamma_{\lambda\alpha}^\mu v_\mu . \tag{2.43}$$

Here the v_i correspond to the components of $\mathbf{V}$ expressed in the surface coordinate system, $\mathbf{V} = v_i\mathbf{e}^i = v^i\mathbf{e}_i$. In deriving the divergence of the stress tensor for an elastic shell, Green and Zerna expressed the tensor elements relative to the midsurface base vectors $\mathbf{e}_i$ instead of the base vectors $\mathbf{g}_i$ associated with the coordinate system. Even though this was done in order to facilitate the integration of the equations across the sheets and obtain physically meaningful stress resultants and bending moments, it is also suitable for our purposes, given that we have already expressed the acceleration term (2.39) in terms of the surface vectors. Hence

$$\sigma^{i\lambda} = fq_\alpha^\lambda\tau^{i\lambda}, \quad \sigma^{i3} = f\tau^{i3} , \tag{2.44}$$

where $f = q_1^1 q_2^2 - q_1^2 q_2^1 = 1 - 2Hx_3 + Kx_3^2$. The divergence of the stress tensor is set equal to the inertial and body forces on the right hand side, which yields the momentum equations:

$$f\rho\left(A^\beta - F_{\text{body}}^\beta\right) = \sigma^{\alpha\beta}\big|_\alpha - b_\alpha^\beta\sigma^{\alpha 3} + \partial_{x_3}\sigma^{3\beta} , \tag{2.45}$$

$$f\rho\left(A^3 - F_{\text{body}}^3\right) = \sigma^{\alpha 3}\big|_\alpha + b_{\alpha\beta}\sigma^{\alpha\beta} + \partial_{x_3}\sigma^{33} , \tag{2.46}$$

where the expressions for the covariant derivatives of the tensor elements are:

$$\sigma^{\alpha\beta}\big|_\alpha = \partial_{x_\alpha}\sigma_\alpha^{\alpha\beta} + \Gamma_{\alpha\gamma}^\beta\sigma^{\alpha\gamma} + \Gamma_{\alpha\gamma}^\alpha\sigma^{\gamma\beta} , \tag{2.47}$$

$$\sigma^{\alpha 3}\big|_\alpha = \partial_{x_\alpha}\sigma^{\alpha 3} + \Gamma_{\alpha\beta}^\alpha\sigma^{\beta 3} . \tag{2.48}$$

2.3.3 Continuity equation

The continuity equation requires incompressibility of the fluid. The strain elements should satisfy $h^{ij}e_{ij} = 0$, or in terms of the velocities and the geometry of the center surface:

$$\partial_{x_3}(fv_3) + \left[a^{\alpha\beta} + x_3\left(b^{\alpha\beta} - 2Ha^{\alpha\beta}\right)\right]v_\alpha|_\beta = 0 .\qquad(2.49)$$

2.4 Boundary conditions

We must now supplement the governing equations with the appropriate boundary conditions. In the end we have to solve the three components of the momentum equations and the continuity for v_i and p. We note that in case the geometry is entirely arbitrary, additional conditions/equations must be provided, as we will see in the next chapter when we consider the special case of an axisymmetric sheet.

2.4.1 Geometry of the boundaries

The thickness h may be considered small compared to the characteristic lengthscale and we assume that the radius of curvature of the center surface is of the order of the characteristic lengthscale and varies slowly along the surface. Nevertheless, there can exist situations where $\partial_{x_\alpha}h$ may be quite important such as near neck regions, or in regions where the film thickness varies rapidly. Therefore, we proceed by deriving the mean curvature of the boundaries in order to take into account these effects. The outer surfaces are defined by:

$$\mathbf{r}^\pm = \mathbf{r}_0 \pm \tfrac{1}{2}h\mathbf{e}_3 ,\qquad(2.50)$$

and tangent vectors by

$$\mathbf{c}_\alpha^\pm = \partial_{x_\alpha}\mathbf{r}^\pm = \mathbf{g}_\alpha^\pm \pm \tfrac{1}{2}\partial_{x_\alpha}h\mathbf{e}_3 .\qquad(2.51)$$

The determinant of the metric tensor $g_{\alpha\beta}^\pm$ is

$$g^\pm = \mathbf{g}_3 \cdot (\mathbf{g}_1 \times \mathbf{g}_2) = af_\pm ,\qquad(2.52)$$
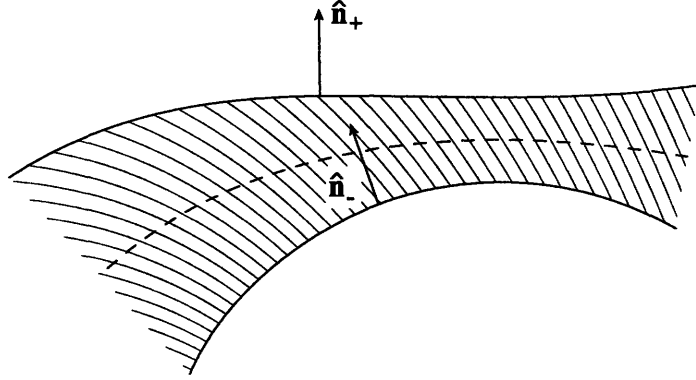
Figure 2-4: Definition sketch of the *outer* and *inner* normals.

where we define $a = \mathbf{e}_3 \cdot (\mathbf{e}_1 \times \mathbf{e}_2) = a_{11}a_{22} - a_{12}a_{21}$ and $f_\pm = 1 \pm Hh + Kh^2/4$. To compute the normal vectors, we consider

$$
\begin{aligned}
c_1^\pm \times c_2^\pm &= \left(\mathbf{g}_1^\pm \pm \tfrac{1}{2}\partial_{x_1}h\mathbf{e}_3\right) \times \left(\mathbf{g}_2^\pm \pm \tfrac{1}{2}\partial_{x_2}h\mathbf{e}_3\right) \\
&= \left(\mathbf{g}_1^\pm \times \mathbf{g}_2^\pm\right) \pm \tfrac{1}{2}\partial_{x_1}h\left(\mathbf{e}_3 \times \mathbf{g}_2^\pm\right) \pm \tfrac{1}{2}\partial_{x_2}h\left(\mathbf{g}_1^\pm \times \mathbf{e}_3\right) \\
&= \frac{\mathbf{g}^3}{g} \mp \tfrac{1}{2}\partial_{x_\alpha}h\frac{\mathbf{g}^\alpha}{g} ,
\end{aligned}
\tag{2.53}
$$

where we have used the reciprocal base property, equation (2.4). The unit normal is:

$$
\hat{\mathbf{n}}^\pm = \frac{\mp\tfrac{1}{2}\partial_{x_\alpha}h\mathbf{g}^\alpha + \mathbf{g}^3}{\sqrt{1 + \tfrac{1}{4}g^{\alpha\beta}\partial_{x_\alpha}h\partial_{x_\beta}h}} .
\tag{2.54}
$$

We note that $\hat{\mathbf{n}}^+$ is the outer normal whereas $\hat{\mathbf{n}}^-$ is the inner normal, in the sense that $\hat{\mathbf{n}}^+/\hat{\mathbf{n}}^-$ points away/towards the fluid region (see Figure 2-4). The first fundamental form is

$$
a_{\alpha\beta}^\pm = \mathbf{c}_\alpha^\pm \cdot \mathbf{c}_\beta^\pm = g_{\alpha\beta}^\pm + \tfrac{1}{4}\partial_{x_\alpha}h\partial_{x_\beta}h .
\tag{2.55}
$$

To find the second fundamental form $b_{\alpha\beta} = \partial_{x_\beta}\mathbf{c}_\alpha^\pm \cdot \mathbf{n}^\pm$, we need to determine the derivatives of the tangent vectors, which are

$$
\partial_{x_\beta}\mathbf{c}_\alpha^\pm = \partial_{x_\beta}\mathbf{g}_\alpha^\pm \mp \tfrac{1}{2}\partial_{x_\alpha}h b_\beta^\lambda \mathbf{e}_\lambda \pm \tfrac{1}{2}\partial_{x_\alpha x_\beta}h\mathbf{e}_3 ,
\tag{2.56}
$$

37

with

$$\partial_{x_\beta} \mathbf{g}_\alpha^\pm = \partial_{x_\beta} \left(q_\alpha^\lambda \mathbf{e}_\lambda \right) = \left(q_\alpha^\lambda \Gamma_{\lambda\beta}^\eta \mp \tfrac{1}{2} \partial_{x_\beta} h b_\alpha^\eta \mp \tfrac{1}{2} h \partial_{x_\beta} b_\alpha^\eta \right) \mathbf{e}_\eta + q_\alpha^\lambda b_{\lambda\beta} \mathbf{e}_3. \tag{2.57}$$

The computation of the second fundamental form is facilitated if we write $\partial_{x_\beta} \mathbf{c}_\alpha^\pm$ in terms of the $\mathbf{g}_i$. Doing so, we find:

$$\partial_{x_\beta} \mathbf{c}_\alpha^\pm = \frac{1}{f_\pm} \left(q_\rho^\rho \delta_\eta^\gamma - q_\eta^\gamma \right) \left(q_\alpha^\lambda \Gamma_{\lambda\beta}^\eta \mp \tfrac{1}{2} b_\alpha^\eta \partial_{x_\beta} h \mp \tfrac{1}{2} b_\beta^\eta \partial_{x_\alpha} h \mp \tfrac{1}{2} h \partial_{x_\beta} b_\alpha^\eta \right) \mathbf{g}_\gamma$$

$$+ \left(q_\alpha^\lambda b_{\lambda\beta} \pm \tfrac{1}{2} \partial_{x_\alpha x_\beta} h \right) \mathbf{g}_3 \; . \tag{2.58}$$

The second fundamental form is thus:

$$b_{\alpha\beta}^\pm = \partial_{x_\beta} \mathbf{c}_\alpha^\pm \cdot \hat{\mathbf{n}}^\pm = \frac{1}{\Lambda_\pm} \left[\frac{-\partial_{x_\gamma} h}{2 f_\pm} \left(q_\rho^\rho \delta_\eta^\gamma - q_\eta^\gamma \right) \left(q_\alpha^\lambda \Gamma_{\lambda\beta}^\eta \mp \tfrac{1}{2} b_\alpha^\eta \partial_{x_\beta} h \mp \tfrac{1}{2} b_\beta^\eta \partial_{x_\alpha} h \mp \tfrac{1}{2} h \partial_{x_\beta} b_\alpha^\eta \right) \right.$$

$$\left. \pm \left(\mu_\alpha^\lambda b_{\lambda\beta} \pm \tfrac{1}{2} \partial_{x_\alpha x_\beta} h_{,\alpha\beta} \right) \right] \; , \tag{2.59}$$

where we set $\Lambda_\pm = \sqrt{1 + \tfrac{1}{4} g_\pm^{\alpha\beta} \partial_{x_\alpha} h \, \partial_{x_\beta} h}$. The mean curvature is found using equations (2.56) and (2.59) in (2.20), which results in a rather unwieldy expression. Noting that the contributions to the mean curvature that arise from the center surface being different from the bounding surfaces essentially come from sharp variations in h, we neglect h to leading order, while at the same time retain the terms involving its derivatives, to find

$$b_{\alpha\beta}^\pm \sim \frac{\pm}{\Lambda_\pm} \left[b_{\alpha\beta} + \frac{\partial_{x_\gamma} h}{4 f_\pm} \left(b_\alpha^\gamma \, \partial_{x_\beta} h + b_\beta^\gamma \, \partial_{x_\alpha} h \mp 2 \Gamma_{\alpha\beta}^\gamma \right) \pm \tfrac{1}{2} \partial_{x_\alpha x_\beta} h \right] \; , \tag{2.60}$$

$$a_{\alpha\beta}^\pm \sim a_{\alpha\beta} + \tfrac{1}{4} \partial_{x_\alpha} h \, \partial_{x_\beta} h \; . \tag{2.61}$$

Finally in the special case of a curvilinear coordinate system, where

$$a_{12} = a_{21} = b_{12} = b_{21} = 0 \tag{2.62}$$

38

we find that the mean curvature may be expressed:

$$
H^{\pm} = \frac{\nabla \cdot \hat{\mathbf{n}}^{\pm}}{2} = \frac{b_{11}^{\pm} a_{22}^{\pm} - 2 b_{12}^{\pm} a_{12}^{\pm} + a_{22}^{\pm} a_{11}^{\pm}}{2 a \left(\Lambda_{\pm}\right)^2}
$$

$$
= \frac{\pm}{2 a \left(\Lambda\right)^3} \left[\left(a_{22} + \tfrac{1}{4}\left(\partial_{x_2} h\right)^2\right) \left(b_{11} + \tfrac{1}{2}\left(\partial_{x_1} h\right)^2 \kappa_1 \mp \tfrac{1}{2}\partial_{x_\gamma} h \; \Gamma_{11}^{\gamma} \pm \tfrac{1}{2}\partial_{x_1 x_1} h\right) \right.
$$

$$
- 2\tfrac{1}{4}\partial_{x_1} h \; \partial_{x_2} h \left(\tfrac{1}{2}\partial_{x_1} h \; \partial_{x_2} h \; H \mp \tfrac{1}{2}\partial_{x_\gamma} h \; \Gamma_{12}^{\gamma} \pm \tfrac{1}{2}\partial_{x_1 x_2} h\right)
$$

$$
\left. + \left(b_{22} + \tfrac{1}{2}\left(\partial_{x_2} h\right)^2 \kappa_2 \mp \tfrac{1}{2}\partial_{x_\gamma} h \; \Gamma_{22}^{\gamma} \pm \tfrac{1}{2}\partial_{x_2 x_2} h\right) \left(a_{11} + \tfrac{1}{4}\left(\partial_{x_1} h\right)^2\right) \right] . \tag{2.63}
$$

This expression can be further simplified if the geometry depends on one coordinate, say x_2. In this case we obtain:

$$
H^+ + H^- = \frac{1}{\left(\Lambda\right)^3}\left[2H + \tfrac{1}{4}\left(\partial_{x_2} h\right)^2 \frac{b_{11} + 2\kappa_2 a_{11}}{a}\right] . \tag{2.64}
$$

$$
H^+ - H^- = \frac{1}{a\left(\Lambda\right)^3}\left[\tfrac{1}{2}\partial_{x_2 x_2} h \; a_{11} - \tfrac{1}{2}\partial_{x_2} h \left(a_{22}\Gamma_{11}^2 + a_{11}\Gamma_{22}^2\right) - \tfrac{1}{8}\left(\partial_{x_2} h\right)^3 \Gamma_{11}^2\right] . \tag{2.65}
$$

In the limit of a planar film we obtain

$$
H^+ - H^- = \frac{\tfrac{1}{2}\partial_{x_2 x_2} h}{\left(1 + \tfrac{1}{4}\left(\partial_{x_2} h\right)^2\right)^{3/2}} , \tag{2.66}
$$

and in the circular geometry:

$$
H^+ - H^- = \frac{\tfrac{1}{2}\partial_{x_2 x_2} h}{\left(1 + \tfrac{1}{4}\left(\partial_{x_2} h\right)^2\right)^{3/2}} - \frac{\tfrac{1}{2}\Gamma_{11}^2 \partial_{x_2} h}{\left(1 + \tfrac{1}{4}\left(\partial_{x_2} h\right)^2\right)^{1/2}} . \tag{2.67}
$$

2.4.2 Boundary conditions

We use the normal to the midsurface, e_3, to define the outer and inner normals, $\hat{\mathbf{n}}_{\pm}$, such that $e_3 \cdot \hat{\mathbf{n}}_{\pm} > 0$ (see figure 2-4). The boundary conditions cast in vector notation take the form.

$$
\hat{\mathbf{n}}_{\pm} \cdot \left(-\mathbf{P}_{\pm} + \mathbf{T}_{\pm}\right) = \pm 2\gamma H \hat{\mathbf{n}}_{\pm} , \tag{2.68}
$$

where $\mathbf{P}_{\pm} = -p_{o\pm} g_{\pm}^{ij} \mathbf{g}_i^{\pm} \mathbf{g}_j^{\pm}$ is stress applied at the boundaries and $p_{o\pm}$ corresponds to the external pressure. Using this convention, the six boundary conditions corresponding to the

top and bottom surfaces become

$$n_k^\pm \mathbf{g}_\pm^k \cdot \left(p_{o\pm} g_\pm^{ij} \mathbf{g}_i^\pm \mathbf{g}_j^\pm + \tau_\pm^{ij} \mathbf{g}_i^\pm \mathbf{g}_j^\pm \right) = \pm 2\gamma H_\pm n_j^\pm \mathbf{g}_\pm^j$$

$$n_i p_{o\pm} g_\pm^{ij} \mathbf{g}_j^\pm + n_i \tau_\pm^{ij} \mathbf{g}_j^\pm = \pm 2\gamma H_\pm n_j^\pm \mathbf{g}_\pm^j \ . \tag{2.69}$$

2.4.3 Kinematic conditions

Finally, the kinematic boundary condition relates the rate at which the boundary moves to the velocities of the particles lying on it. Since the boundaries are treated as material surfaces, we have:

$$\frac{d}{dt}\left(x_3 \pm \tfrac{1}{2}h\right) = 0 \Rightarrow u_3 \pm \tfrac{1}{2}\left[\partial_t h + (\mathbf{V} - \partial_t \mathbf{r}) \cdot \nabla h\right] = 0 \ , \tag{2.70}$$

with

$$\boldsymbol{\nabla} h = \partial_{x_\beta} h \ \mathbf{g}^\beta. \tag{2.71}$$

Chapter 3

Leading order expansions in curvilinear coordinates

3.1 Introduction

The general theory developed in the previous chapter is admittedly rather complicated to apply, but it is necessary for entirely arbitrary geometries. Here we turn our attention to geometries that can be studied with a curvilinear, orthogonal coordinate system. This kind of coordinate system results by parametrizing the center-surface by lines of curvature where the coordinate curves intersect each other at right angles. This type of geometric parametrization was considered in the past for example by Fliert *et al.*, [45], and Ida & Miksis, [61]. In [45], attention was limited to Stokes flow in industrial processes such as glass blowing. In [61], an attempt was made to present the equations for a more general setting by incorporating van der Waals forces and Marangoni stresses in their model, but the resulting equations were cumbersome and they neglected the effects of the variations of the film thickness. These effects are essential for sheet retraction, a problem to be considered in Chapter 4. Moreover the normal momentum equation they derive was incorrectly formulated.

In what follows, we define the curvilinear coordinate system and the simplifications that result in the governing equations. By exploiting the slenderness of the film, an asymptotic analysis is performed resulting in a system of evolution equations for the shape of the center-surface, film thickness and velocities as measured in the moving-surface coordinate system.

The chapter is concluded by giving the leading order equations for the case of an unsteady axisymmetric fluid film which will be the main focus of subsequent chapters.

3.2 Navier Stokes equations in curvilinear coordinates

We begin our derivation by considering a curvilinear coordinate system in which the coordinate curves x_i =constant are mutually orthogonal. This formulation is most appropriate when the system we are dealing with exhibits some symmetries or in geometries where enforcing the orthogonality of the coordinate curves is not difficult. It is thus important to note that the assumption that the midsurface is parametrized by lines-of-curvature need not hold as the surface moves and deforms in time. In such a case a remeshing would be required at each time-step. Alternatively an asymptotic expansion of the more complicated equations of Chapter 2 needs to be considered. Geometries that exhibit certain symmetries however have this property of preserving the orthogonality of the coordinate curves at all times. In the case of lines-of-curvature parametrization of the center surface, the differential geometric quantities we used in the previous chapter reduce to:

$$q_1^1 = 1 - x_3\kappa_1, \ q_2^2 = 1 - x_3\kappa_2 \text{ and } q_1^2 = q_2^1 = 0 \ , \tag{3.1}$$

$$b_1^1 = \kappa_1, \ b_2^2 = \kappa_2 \text{ and } b_1^2 = b_2^1 = 0 \ , \tag{3.2}$$

$$b_{11} = a_{11}\kappa_1, \ b_{22} = a_{22}\kappa_2 \text{ and } b_{12} = b_{21} = 0 \ . \tag{3.3}$$

The Christoffel symbols associated with the midsurface become

$$\begin{aligned} \Gamma_{11}^1 &= \frac{1}{a_1}\frac{\partial a_1}{\partial x_1} & \Gamma_{11}^2 &= -\frac{a_1}{a_2^2}\frac{\partial a_1}{\partial x_2} \\ \Gamma_{12}^1 &= \frac{1}{a_1}\frac{\partial a_1}{\partial x_2} & \Gamma_{12}^2 &= \frac{1}{a_2}\frac{\partial a_2}{\partial x_1} \\ \Gamma_{22}^1 &= -\frac{a_2}{a_1^2}\frac{\partial a_2}{\partial x_1} & \Gamma_{22}^2 &= \frac{1}{a_2}\frac{\partial a_2}{\partial x_2} \ , \end{aligned} \tag{3.4}$$

where we use

$$a_\beta = \sqrt{a_{\beta\beta}} = |\mathbf{e}_\beta| \ . \tag{3.5}$$

Hereafter, to avoid any difficulties in notation, we drop the lowered and raised indices to distinguish between the covariant and contravariant components considered in the previous

chapter. Henceforth, a raised index denotes a power. We also define

$$l_\beta = a_\beta \left(1 - x_3 \kappa_\beta\right) \ . \tag{3.6}$$

In addition, let the *physical* components of the velocity in the coordinate system attached to the midsurface be

$$\mathbf{u} = u_i \hat{\mathbf{e}}_i \ , \tag{3.7}$$

and the fluid velocity

$$\mathbf{v} = \frac{\partial \mathbf{r}}{\partial t} + \mathbf{u} = v_i \hat{\mathbf{e}}_i \ . \tag{3.8}$$

The acceleration term becomes

$$
\begin{aligned}
\frac{d\mathbf{v}}{dt} ={}& \frac{\partial^2 \mathbf{r}_0}{\partial t^2} + x_3 \frac{\partial^2 \hat{\mathbf{e}}_3}{\partial t^2} + 2u_3 \frac{\partial \hat{\mathbf{e}}_3}{\partial t} + 2u_1 \frac{\partial \hat{\mathbf{e}}_1}{\partial t} + 2u_2 \frac{\partial \hat{\mathbf{e}}_2}{\partial t} \\
&+ \left[\frac{1}{l_1} \frac{\partial (u_1 l_1)}{\partial t} + \frac{u_1}{l_1} \left(\frac{\partial u_1}{\partial x_1} + \frac{u_2}{a_2} \frac{\partial a_1}{\partial x_2} \right) + \frac{u_2}{l_2} \left(\frac{\partial u_1}{\partial x_2} - \frac{u_2}{a_1} \frac{\partial a_2}{\partial x_1} \right) + u_3 \left(\frac{\partial u_1}{\partial x_3} - \kappa_1 u_1 \frac{a_1}{l_1} \right) \right] \hat{\mathbf{e}}_1 \\
&+ \left[\frac{1}{l_2} \frac{\partial (u_2 l_2)}{\partial t} + \frac{u_1}{l_1} \left(\frac{\partial u_2}{\partial x_1} - \frac{u_1}{a_2} \frac{\partial a_1}{\partial x_2} \right) + \frac{u_2}{l_2} \left(\frac{\partial u_2}{\partial x_2} + \frac{u_1}{a_1} \frac{\partial a_2}{\partial x_1} \right) + u_3 \left(\frac{\partial u_2}{\partial x_3} - \kappa_2 u_2 \frac{a_2}{l_2} \right) \right] \hat{\mathbf{e}}_2 \\
&+ \left[\frac{\partial u_3}{\partial t} + \frac{u_1}{l_1} \frac{\partial u_3}{\partial x_1} + \frac{u_2}{l_2} \frac{\partial u_3}{\partial x_2} + u_3 \frac{\partial u_3}{\partial x_3} + u_1^2 \kappa_1 \frac{a_1}{l_1} + u_2^2 \kappa_2 \frac{a_2}{l_2} \right] \hat{\mathbf{e}}_3 \ .
\end{aligned}
\tag{3.9}
$$

By including the inertial terms (3.9), the full Navier Stokes equations become:

$$
\begin{aligned}
\rho l_1 l_2 \left(\frac{d\mathbf{v}}{dt} - \mathbf{f}_{\text{body}} \right) ={}& \left[\frac{\partial}{\partial x_1} \left(l_2 T_{11} \right) + \frac{1}{l_1} \frac{\partial}{\partial x_2} \left(l_1^2 T_{12} \right) + \frac{1}{l_1} \frac{\partial}{\partial x_3} \left(l_1^2 l_2 T_{13} \right) - \frac{\partial l_2}{\partial x_1} T_{22} \right] \hat{\mathbf{e}}_1 \\
&+ \left[\frac{1}{l_2} \frac{\partial}{\partial x_1} \left(l_2^2 T_{12} \right) + \frac{\partial}{\partial x_2} \left(l_1 T_{22} \right) + \frac{1}{l_2} \frac{\partial}{\partial x_3} \left(l_1 l_2^2 T_{23} \right) - \frac{\partial l_1}{\partial x_2} T_{11} \right] \hat{\mathbf{e}}_2 \\
&+ \left[\frac{\partial}{\partial x_1} \left(l_2 T_{13} \right) + \frac{\partial}{\partial x_2} \left(l_1 T_{23} \right) + \frac{\partial}{\partial x_3} \left(l_1 l_2 T_{33} \right) - l_2 \frac{\partial l_1}{\partial x_3} T_{11} - l_1 \frac{\partial l_2}{\partial x_3} T_{22} \right] \hat{\mathbf{e}}_3 \ ,
\end{aligned}
\tag{3.10}
$$

with the physical components of the stress given by (e.g. [45] and [124]):

$$T_{11} = -p + \frac{2\mu}{l_1} \left(\frac{\partial v_1}{\partial x_1} + \frac{v_2}{l_2} \frac{\partial l_1}{\partial x_2} - a_1 \kappa_1 v_3 \right) , \tag{3.11}$$

$$T_{22} = -p + \frac{2\mu}{l_2} \left(\frac{\partial v_2}{\partial x_2} + \frac{v_1}{l_1} \frac{\partial l_2}{\partial x_1} - a_2 \kappa_2 v_3 \right) , \tag{3.12}$$

$$T_{33} = -p + 2\mu \frac{\partial v_3}{\partial x_3} , \tag{3.13}$$

$$T_{12} = \frac{\mu}{l_1 l_2} \left(l_1 \frac{\partial v_1}{\partial x_2} - \frac{\partial l_1}{\partial x_2} v_1 + l_2 \frac{\partial v_2}{\partial x_1} - \frac{\partial l_2}{\partial x_1} v_2 \right) , \tag{3.14}$$

$$T_{13} = \frac{\mu}{l_1} \left(l_1 \frac{\partial v_1}{\partial x_3} + a_1 \kappa_1 v_1 + \frac{\partial v_3}{\partial x_1} \right) , \tag{3.15}$$

$$T_{23} = \frac{\mu}{l_2} \left(l_2 \frac{\partial v_2}{\partial x_3} + a_2 \kappa_2 v_2 + \frac{\partial v_3}{\partial x_2} \right) . \tag{3.16}$$

Finally, the incompressibility condition may be expressed as

$$\frac{\partial}{\partial x_1} (l_2 v_1) + \frac{\partial}{\partial x_2} (l_1 v_2) + \frac{\partial}{\partial x_3} (l_1 l_2 v_3) = 0 . \tag{3.17}$$

Before proceeding further, we need to consider how the geometry of the midsurface is related to its speed. Letting:

$$\frac{\partial \mathbf{r}_0}{\partial t} = \bar{w}_i \hat{\mathbf{e}}_i \tag{3.18}$$

and following [45], we have

$$\frac{\partial}{\partial t} \left(\frac{\partial \mathbf{r}_0}{\partial x_1} \cdot \frac{\partial \mathbf{r}_0}{\partial x_2} \right) = 0 \Rightarrow \bar{w}_1 \frac{\partial a_1}{\partial x_2} + \bar{w}_2 \frac{\partial a_2}{\partial x_1} = a_1 \frac{\partial \bar{w}_1}{\partial x_2} + a_2 \frac{\partial \bar{w}_2}{\partial x_1} , \tag{3.19}$$

$$\frac{\partial}{\partial t} \left(\frac{\partial \mathbf{r}_0}{\partial x_1} \cdot \frac{\partial \mathbf{r}_0}{\partial x_1} \right) = 2a_1 \frac{\partial a_1}{\partial t} \Rightarrow a_2 \frac{\partial a_1}{\partial t} = a_2 \frac{\partial \bar{w}_1}{\partial x_1} + \bar{w}_2 \frac{\partial a_1}{\partial x_2} - a_1 a_2 \kappa_1 \bar{w}_3 , \tag{3.20}$$

$$\frac{\partial}{\partial t} \left(\frac{\partial \mathbf{r}_0}{\partial x_2} \cdot \frac{\partial \mathbf{r}_0}{\partial x_2} \right) = 2a_2 \frac{\partial a_2}{\partial t} \Rightarrow a_1 \frac{\partial a_2}{\partial t} = a_1 \frac{\partial \bar{w}_2}{\partial x_2} + \bar{w}_1 \frac{\partial a_2}{\partial x_1} - a_1 a_2 \kappa_2 \bar{w}_3 . \tag{3.21}$$

Adding (3.20) and (3.21) yields

$$\frac{\partial}{\partial t} (a_1 a_2) = \frac{\partial}{\partial x_1} (a_2 \bar{w}_1) + \frac{\partial}{\partial x_2} (a_1 \bar{w}_2) - a_1 a_2 (\kappa_1 + \kappa_2) \bar{w}_3 . \tag{3.22}$$

3.3   Slenderness approximation

We take advantage of the slenderness of the sheet to simplify the equations. To do a proper leading order expansion of the equations we need to assume that h, the thickness of the

44

sheet obeys

$$h\kappa_1 \ll 2 \text{ and } h\kappa_2 \ll 2 , \qquad (3.23)$$

where $\kappa_{1,2}$ correspond to the principal radii of curvature. This essentially means that the characteristic thickness of the film is much smaller than its longitudinal lengthscales. If this does not hold, the full set of equations (3.10) and (3.17) should be used, because when $h\kappa_1 = 2$ or $h\kappa_2 = 2$ the system of equations becomes singular. To non-dimensionalize the equations, we choose the scalings

$$
\begin{aligned}
a_1 x_1 &= L_1 a_1^* x_1^* & v_1 &= v_{10} v_1^* & \kappa_1 &= L_1^{-1} \kappa_1^* \\
a_2 x_2 &= L_2 a_2^* x_2^* & v_2 &= v_{20} v_2^* & \kappa_2 &= L_2^{-1} \kappa_2^* \text{ and } t = \tau t^* , \\
x_3 &= h x_3^* & v_3 &= v_{30} v_3^* & p &= p_0 p^*
\end{aligned}
\qquad (3.24)
$$

where the starred quantities are non-dimensional. The characteristic pressure p_0 depends on whether the motion is driven by surface tension or an applied pressure difference. Letting $\varepsilon = h/\max(L_1, L_2)$, we write the hydrodynamic quantities as an expansion

$$A = A^{(0)} + \varepsilon A^{(1)} + \varepsilon^2 A^{(2)} + ... \qquad (3.25)$$

Performing the analysis using this expansion, we find that $A^{(0)}$ does not depend on x_3 under the assumption that $x_3 = 0$ is a material surface. This assumption means that the fluid particles that lie on $x_3 = 0$ remain on it for all times, thus implying that

$$u_3(x_1, x_2, 0, t) = 0 . \qquad (3.26)$$

This reasoning motivates our alternative expansion in powers of x_3, i.e.

$$A = \tilde{A}^{(0)} + \frac{x_3}{h} \tilde{A}^{(1)} + \frac{x_3^2}{h^2} \tilde{A}^{(2)} + ... \qquad (3.27)$$

To be consistent with the proposed expansion, the effects of outer surface variations should be neglected to leading order. However, retaining the full curvature terms, as was done for the circular jet break-up by Eggers & Dupont [43] and for the planar sheet retraction by Brenner & Gueyffier [13], gave results that better agreed with experimental observations. Eggers in [41] presented an argument based on a Galerkin-type expansion, where one retains

the full curvature terms in the leading order equations of the circular jet breakup. By the same token it is reasonable to treat these terms as being leading order in our system. Therefore in our expansion we consider the viscous terms in the long wavelength limit, but retain the terms associated with surface tension provided (3.23) holds.

With this kind of expansion we can study the governing equations *restricted* to the center-surface. The final accuracy of the calculation will depend on how well we can estimate the derivatives with respect to x_3. The leading order equations are essentially the same for each of the different expansions (3.25) and (3.27). Denoting with bars the velocities evaluated at $x_3 = 0$ and using equation (3.26), the inertial terms in dimensional form become:

$$\left\lfloor \frac{d\mathbf{v}}{dt} \right\rfloor_{x_3=0} = \frac{\partial^2 \mathbf{r}_0}{\partial t^2} + 2\bar{u}_1 \frac{\partial \hat{\mathbf{e}}_1}{\partial t} + 2\bar{u}_2 \frac{\partial \hat{\mathbf{e}}_2}{\partial t}$$
$$+ \left[\frac{\partial \bar{u}_1}{\partial t} + \frac{\bar{u}_1}{a_1} \frac{\partial a_1}{\partial t} + \frac{\bar{u}_1}{a_1} \left(\frac{\partial \bar{u}_1}{\partial x_1} + \frac{\bar{u}_2}{a_2} \frac{\partial a_1}{\partial x_2} \right) + \frac{\bar{u}_2}{a_2} \left(\frac{\partial \bar{u}_1}{\partial x_2} - \frac{\bar{u}_2}{a_1} \frac{\partial a_2}{\partial x_1} \right) \right] \hat{\mathbf{e}}_1$$
$$+ \left[\frac{\partial \bar{u}_2}{\partial t} + \frac{\bar{u}_2}{a_2} \frac{\partial a_2}{\partial t} + \frac{\bar{u}_1}{a_1} \left(\frac{\partial \bar{u}_2}{\partial x_1} - \frac{\bar{u}_1}{a_2} \frac{\partial a_1}{\partial x_2} \right) + \frac{\bar{u}_2}{a_2} \left(\frac{\partial \bar{u}_2}{\partial x_2} + \frac{\bar{u}_1}{a_1} \frac{\partial a_2}{\partial x_1} \right) \right] \hat{\mathbf{e}}_2$$
$$+ \left(\bar{u}_1^2 \kappa_1 + \bar{u}_2^2 \kappa_2 \right) \hat{\mathbf{e}}_3 , \tag{3.28}$$

where we wrote $\lfloor B \rfloor_{x_3=0}$ to denote the quantity B evaluated at $x_3 = 0$. Alternatively we may group some terms to get the more compact form:

$$\left\lfloor \frac{d\mathbf{v}}{dt} \right\rfloor_{x_3=0} = \frac{\partial^2 \mathbf{r}_0}{\partial t^2} + 2\bar{u}_1 \frac{\partial \hat{\mathbf{e}}_1}{\partial t} + 2\bar{u}_2 \frac{\partial \hat{\mathbf{e}}_2}{\partial t}$$
$$+ \frac{1}{a_1} \left[\frac{\partial (a_1 \bar{u}_1)}{\partial t} + \frac{1}{2} \frac{\partial \bar{u}_1^2}{\partial x_1} + \frac{\bar{u}_2}{a_2} \frac{\partial (a_1 \bar{u}_1)}{\partial x_2} - \frac{\bar{u}_2^2}{a_2} \frac{\partial a_2}{\partial x_1} \right] \hat{\mathbf{e}}_1$$
$$+ \frac{1}{a_2} \left[\frac{\partial (a_2 \bar{u}_2)}{\partial t} + \frac{1}{2} \frac{\partial \bar{u}_2^2}{\partial x_2} + \frac{\bar{u}_1}{a_1} \frac{\partial (a_2 \bar{u}_2)}{\partial x_1} - \frac{\bar{u}_1^2}{a_1} \frac{\partial a_1}{\partial x_2} \right] \hat{\mathbf{e}}_2$$
$$+ \left(\bar{u}_1^2 \kappa_1 + \bar{u}_2^2 \kappa_2 \right) \hat{\mathbf{e}}_3 . \tag{3.29}$$

It is important to note here that the acceleration term in (3.29) is *exact*, assuming (3.26) holds. If higher order accuracy is desired, the expansion should proceed by considering higher order terms that come from the divergence of the stress tensor. The Navier Stokes

equations now assume the form:

$$\rho \left[\frac{d\mathbf{v}}{dt} \right]_{x_3=0} = \left[\left[\frac{\partial T_{13}}{\partial x_3} \right]_{x_3=0} - (2\kappa_1 + \kappa_2)\,\bar{T}_{13} + \frac{1}{a_1}\frac{\partial}{\partial x_1}\bar{T}_{11} \right.$$

$$\left. + \frac{1}{a_1^2 a_2}\frac{\partial}{\partial x_2}\left(a_1^2 \bar{T}_{12}\right) + \frac{1}{a_1 a_2}\frac{\partial a_2}{\partial x_1}\left(\bar{T}_{11} - \bar{T}_{22}\right) \right]\hat{\mathbf{e}}_1$$

$$+ \left[\left[\frac{\partial T_{23}}{\partial x_3} \right]_{x_3=0} - (2\kappa_2 + \kappa_1)\,\bar{T}_{23} + \frac{1}{a_2^2 a_1}\frac{\partial}{\partial x_1}\left(a_2^2 \bar{T}_{12}\right) \right.$$

$$\left. + \frac{1}{a_2}\frac{\partial}{\partial x_2}\left(\bar{T}_{22}\right) + \frac{1}{a_1 a_2}\frac{\partial a_1}{\partial x_2}\left(\bar{T}_{22} - \bar{T}_{11}\right) \right]\hat{\mathbf{e}}_2$$

$$+ \left[\left[\frac{\partial T_{33}}{\partial x_3} \right]_{x_3=0} - (\kappa_1 + \kappa_2)\,\bar{T}_{33} + \kappa_1 \bar{T}_{11} + \kappa_2 \bar{T}_{22} \right.$$

$$\left. + \frac{1}{a_1 a_2}\frac{\partial}{\partial x_1}\left(a_2 \bar{T}_{13}\right) + \frac{1}{a_1 a_2}\frac{\partial}{\partial x_2}\left(a_1 \bar{T}_{23}\right) \right]\hat{\mathbf{e}}_3 \qquad (3.30)$$

and the continuity equation requires that

$$\left[\frac{\partial v_3}{\partial x_3} \right]_{x_3=0} = (\kappa_1 + \kappa_2)\,\bar{v}_3 - \frac{1}{a_1 a_2}\left[\frac{\partial}{\partial x_1}\left(a_2 \bar{v}_1\right) + \frac{\partial}{\partial x_2}\left(a_1 \bar{v}_2\right) \right] \qquad (3.31)$$

$$\overset{(3.22)}{=} -\frac{1}{a_1 a_2}\left[\frac{\partial}{\partial x_1}\left(a_2 \bar{u}_1\right) + \frac{\partial}{\partial x_2}\left(a_1 \bar{u}_2\right) + \frac{\partial}{\partial t}\left(a_1 a_2\right) \right] \, . \qquad (3.32)$$

We note that we have yet to make any approximation. The approximation lies in how the normal derivatives are evaluated at the center-surface. The slenderness of the sheet allows us to estimate them using:

$$\left[\frac{\partial T_{i3}}{\partial x_3} \right]_{x_3=0} \sim \frac{T_{i3}^+ - T_{i3}^-}{h} \, , \qquad (3.33)$$

where $T_{i3}^{\pm}$ correspond to T_{i3} evaluated at the top and bottom surfaces of the sheet respectively. These $T_{i3}^{\pm}$ can be determined from the stress boundary conditions.

3.4 Stress conditions

We adopt the convention that the normals to the boundaries satisfy $\hat{\mathbf{n}}_{\pm} \cdot \hat{\mathbf{n}} \geq 0$. With this notation, we label the respective inner and outer regions such that the normal always points in the *outer* region (see figure 2-4). As in the previous chapter the boundary conditions at

the top and bottom surfaces $\mathbf{r}^\pm = \mathbf{r}_0 \pm \frac{1}{2}h\hat{\mathbf{e}}_3$ become:

$$\hat{\mathbf{n}}_\pm \cdot \left(p_0^\pm \hat{\mathbf{e}}_i \hat{\mathbf{e}}_i + T_{ij}^\pm \hat{\mathbf{e}}_i \hat{\mathbf{e}}_j \right) = \pm 2\gamma H_\pm \hat{\mathbf{n}}_\pm \ , \tag{3.34}$$

where H is the mean curvature of the surface. The unit normal vectors are:

$$\hat{\mathbf{n}}^\pm = \frac{\mp \frac{1}{2} \frac{\partial_1 h}{l_1} \hat{\mathbf{e}}_1 \mp \frac{1}{2} \frac{\partial_2 h}{l_2} \hat{\mathbf{e}}_2 + \hat{\mathbf{e}}_3}{\sqrt{1 + \frac{1}{4} \left(\partial_1 h \right)^2 / l_1^2 + \frac{1}{4} \left(\partial_2 h \right)^2 / l_2^2}} = \frac{1}{\Lambda_\pm} \left(\mp \frac{1}{2} \frac{\partial_1 h}{l_1} \hat{\mathbf{e}}_1 \mp \frac{1}{2} \frac{\partial_2 h}{l_2} \hat{\mathbf{e}}_2 + \hat{\mathbf{e}}_3 \right) \ . \tag{3.35}$$

From (3.34) and (3.35), the stress conditions in each direction take the form:

$$T_{31}^\pm = \pm \frac{1}{2} \frac{\partial_1 h}{l_1^\pm} \left(p_0^\pm - 2\gamma H_\pm + T_{11}^\pm \right) \pm \frac{1}{2} \frac{\partial_2 h}{l_2^\pm} T_{21}^\pm \ , \tag{3.36}$$

$$T_{32}^\pm = \pm \frac{1}{2} \frac{\partial_1 h}{l_1^\pm} T_{12}^\pm \pm \frac{1}{2} \frac{\partial_2 h}{l_2^\pm} \left(p_0^\pm - 2\gamma H_\pm + T_{22}^\pm \right) \ , \tag{3.37}$$

$$T_{33}^\pm = -p_0^\pm \pm 2\gamma H_\pm \pm \frac{1}{2} \frac{\partial_1 h}{l_1^\pm} T_{13}^\pm \pm \frac{1}{2} \frac{\partial_2 h}{l_2^\pm} T_{23}^\pm \ . \tag{3.38}$$

To leading order in ε we thus have

$$l_i^\pm = a_i + \mathcal{O}\left(\varepsilon \right) \ , \tag{3.39}$$

$$T_{ij}^+ + T_{ij}^- = 2\bar{T} \ . \tag{3.40}$$

We define

$$\Delta H = H_+ - H_- \ , \quad \bar{H} = \frac{1}{2} \left(H_+ + H_- \right) \ , \tag{3.41}$$

$$\Delta p = p_0^+ - p_0^- \ , \quad \bar{p} = \frac{1}{2} \left(p_0^+ + p_0^- \right) \tag{3.42}$$

and assume that $h\kappa_1 \ll 1$ and $h\kappa_2 \ll 1$ so that by applying the long wavelength approximation for the viscous terms we get:

$$T_{31}^+ - T_{31}^- = \tfrac{1}{2}\frac{\partial_1 h}{a_1}\left(-2\gamma\left(H_+ - H_-\right) + p_0^+ + p_0^- + 2\bar{T}_{11}\right) + \frac{\partial_2 h}{a_2}\bar{T}_{21} \tag{3.43}$$

$$T_{32}^+ - T_{32}^- = \tfrac{1}{2}\frac{\partial_2 h}{a_2}\left(-2\gamma\left(H_+ - H_-\right) + p_0^+ + p_0^- + 2\bar{T}_{22}\right) + \frac{\partial_1 h}{a_1}\bar{T}_{21} \tag{3.44}$$

$$T_{31}^+ + T_{31}^- \approx \tfrac{1}{2}\frac{\partial_1 h}{a_1}\left(\Delta p - 2\gamma\left(H_+ + H_-\right) + T_{11}^+ - T_{11}^-\right) + \tfrac{1}{2}\frac{\partial_2 h}{a_2}\left(T_{21}^+ - T_{21}^-\right) \approx 0 \tag{3.45}$$

$$T_{32}^+ + T_{32}^- \approx \tfrac{1}{2}\frac{\partial_2 h}{a_2}\left(\Delta p - 2\gamma\left(H_+ + H_-\right) + T_{22}^+ - T_{22}^-\right) + \tfrac{1}{2}\frac{\partial_1 h}{a_1}\left(T_{21}^+ - T_{21}^-\right) \approx 0\;. \tag{3.46}$$

Another way to argue that $\bar{T}_{3\beta} \approx \tfrac{1}{2}\left(T_{3\beta}^+ + T_{3\beta}^-\right) \approx 0$ is by looking at the stress element itself. Using

$$\frac{\partial v_\beta}{\partial x_3} = \frac{\partial u_\beta}{\partial x_3} + \frac{\partial}{\partial x_3}\left(\frac{\partial \mathbf{r}}{\partial t}\right) = \frac{\partial u_\beta}{\partial x_3} - \left(\kappa_\beta \bar{w}_\beta + \frac{1}{a_\beta}\frac{\partial \bar{w}_3}{\partial x_\beta}\right)\hat{\mathbf{e}}_\beta\;, \tag{3.47}$$

we find that:

$$\bar{T}_{3\beta} = \mu\left(\left\lfloor\frac{\partial u_\beta}{\partial x_3}\right\rfloor_{x_3=0} + \kappa_\beta \bar{u}_\beta\right) \tag{3.48}$$

To leading order, however, we expect the fluid particles to move around a curving sheet with roughly the same local angular speed unless some external shear is applied (the minus sign results from the convention that the normal points outwards, so the radius of curvature has an opposite sign). Hence:

$$\left\lfloor\frac{\partial u_\beta}{\partial x_3}\right\rfloor_{x_3=0} \approx -\kappa_\beta \bar{u}_\beta\;. \tag{3.49}$$

We can then estimate the pressure at the midsurface, $\bar{p}$ using (3.32):

$$\bar{T}_{33} = \frac{T_{33}^+ + T_{33}^-}{2} \Rightarrow$$

$$-\bar{p} = -\tfrac{1}{2}\left(p_0^+ + p_0^-\right) + \gamma\Delta H + \frac{2\mu}{a_1 a_2}\left[\frac{\partial}{\partial x_1}\left(a_2\bar{u}_1\right) + \frac{\partial}{\partial x_2}\left(a_1\bar{u}_2\right) + \frac{\partial}{\partial t}\left(a_1 a_2\right)\right] \tag{3.50}$$

The last equation is a direct result of the lubrication approximation, where we treat $\partial_1 h\left(T_{31}^+ - T_{31}^-\right)/a_1$ and $\partial_2 h\left(T_{32}^+ - T_{32}^-\right)/a_2$ as small, viscosity-dependent terms in the long wavelength limit. Finally, we estimate $\lfloor\partial_{x_3}T_{i3}\rfloor_{x_3=0}$ using equations $(3.36) - (3.38)$ together

49

with (3.45) and (3.46) in (3.33) :

$$\left. \frac{\partial T_{13}}{\partial x_3} \right|_{x_3=0} = \frac{\partial_1 h}{a_1 h} \left(\tfrac{1}{2} \left(p_0^+ + p_0^- \right) - \gamma \Delta H + \bar{T}_{11} \right) + \frac{\partial_2 h}{a_2 h} \bar{T}_{21} \; , \qquad (3.51)$$

$$\left. \frac{\partial T_{23}}{\partial x_3} \right|_{x_3=0} = \frac{\partial_1 h}{a_1 h} \bar{T}_{21} + \frac{\partial_2 h}{a_2 h} \left(\tfrac{1}{2} \left(p_0^+ + p_0^- \right) - \gamma \Delta H + \bar{T}_{22} \right) \; , \qquad (3.52)$$

$$\left. \frac{\partial T_{33}}{\partial x_3} \right|_{x_3=0} = \frac{-\Delta p + 2\gamma \left(H_+ + H_- \right)}{h} \; . \qquad (3.53)$$

3.5 Continuity equation

The kinematic boundary condition is:

$$\frac{d}{dt} \left(x_3 \pm \tfrac{1}{2} h \right) = 0 \; , \qquad (3.54)$$

whose leading order expression is written as

$$u_3^\pm = \pm \tfrac{1}{2} \left(\frac{\partial h}{\partial t} + \frac{\bar{u}_1}{a_1} \frac{\partial h}{\partial x_1} + \frac{\bar{u}_2}{a_2} \frac{\partial h}{\partial x_2} \right) \; . \qquad (3.55)$$

Combining with (3.32), after some algebra we obtain a continuity equation of the form

$$\left. \frac{\partial v_3}{\partial x_3} \right|_{x_3=0} = \frac{u_3^+ - u_3^-}{h} \Rightarrow$$

$$\frac{\partial h}{\partial t} + \frac{1}{a_1 a_2} \left[\frac{\partial}{\partial x_1} \left(h a_2 \bar{u}_1 \right) + \frac{\partial}{\partial x_2} \left(h a_1 \bar{u}_2 \right) \right] = -\frac{h}{a_1 a_2} \left[\frac{\partial}{\partial x_1} \left(a_2 \bar{w}_1 \right) + \frac{\partial}{\partial x_2} \left(a_1 \bar{w}_2 \right) \right]$$

$$- h \left(\kappa_1 + \kappa_2 \right) \bar{w}_3 \; . \qquad (3.56)$$

The term on the right hand side of (3.56) accounts for the motion of the midsurface. Rearranging terms using equation (3.22) yields the simpler expression:

$$\frac{\partial}{\partial t} \left(a_1 a_2 h \right) + \frac{\partial}{\partial x_1} \left(h a_2 \bar{u}_1 \right) + \frac{\partial}{\partial x_2} \left(h a_1 \bar{u}_2 \right) = 0 \; . \qquad (3.57)$$

3.6 Leading order Navier Stokes equations

To simplify the notation we define a *modified* pressure P, in terms of the physical pressure p derived in equation (3.50)

$$P = \tfrac{1}{2}\left(p_0^+ + p_0^-\right) - \gamma\Delta H \ . \tag{3.58}$$

The stress elements are also modified by a tensor $\bar{S}_{\alpha\beta}$ such that

$$\bar{T}_{11} = -P + \bar{S}_{11} \ , \quad \bar{T}_{33} = -P \ , \\ \bar{T}_{22} = -P + \bar{S}_{22} \ , \quad \bar{T}_{12} = \bar{S}_{12} \ . \tag{3.59}$$

After a bit of algebra, we find the tensor elements to be:

$$\bar{S}_{11} = \frac{2\mu}{a_1 a_2}\left[\frac{1}{\bar{u}_1}\frac{\partial\left(\bar{u}_1^2 a_2\right)}{\partial x_1} + \frac{1}{a_1}\frac{\partial\left(\bar{u}_2 a_1^2\right)}{\partial x_2} + \frac{1}{a_1}\frac{\partial a_1^2 a_2}{\partial t}\right] \ , \tag{3.60}$$

$$\bar{S}_{22} = \frac{2\mu}{a_1 a_2}\left[\frac{1}{a_2}\frac{\partial\left(\bar{u}_1 a_2^2\right)}{\partial x_1} + \frac{1}{\bar{u}_2}\frac{\partial\left(a_1\bar{u}_2^2\right)}{\partial x_2} + \frac{1}{a_2}\frac{\partial\left(a_1 a_2^2\right)}{\partial t}\right] \ , \tag{3.61}$$

$$\bar{S}_{12} = \frac{\mu}{a_1 a_2}\left(a_1^2\frac{\partial\left(\bar{u}_1/a_1\right)}{\partial x_2} + a_2^2\frac{\partial\left(\bar{u}_2/a_2\right)}{\partial x_1}\right) \ . \tag{3.62}$$

Using equations $(3.51)-(3.53)$ in (3.30), we arrive at the leading order momentum equations along each of the vectors $\hat{e}_1, \hat{e}_2$ and $\hat{e}_3$ respectively:

$$\rho\left(\frac{\partial^2 \mathbf{r}_0}{\partial t^2} + 2\bar{u}_1\frac{\partial\hat{e}_1}{\partial t} + 2\bar{u}_2\frac{\partial\hat{e}_2}{\partial t}\right)\cdot\hat{e}_1 + \frac{\rho}{a_1}\left[\frac{\partial\left(a_1\bar{u}_1\right)}{\partial t} + \frac{1}{2}\frac{\partial\bar{u}_1^2}{\partial x_1} + \frac{\bar{u}_2}{a_2}\frac{\partial\left(a_1\bar{u}_1\right)}{\partial x_2} - \frac{\bar{u}_2^2}{a_2}\frac{\partial a_2}{\partial x_1}\right]$$
$$= -\frac{1}{a_1}\frac{\partial P}{\partial x_1} + \frac{1}{a_1 a_2 h}\frac{\partial\left(h a_2\bar{S}_{11}\right)}{\partial x_1} + \frac{1}{h a_2 a_1^2}\frac{\partial}{\partial x_2}\left(h a_1^2\bar{S}_{12}\right) - \frac{1}{a_1 a_2}\frac{\partial a_2}{\partial x_1}\bar{S}_{22} \ , \tag{3.63}$$

$$\rho\left(\frac{\partial^2 \mathbf{r}_0}{\partial t^2} + 2\bar{u}_1\frac{\partial\hat{e}_1}{\partial t} + 2\bar{u}_2\frac{\partial\hat{e}_2}{\partial t}\right)\cdot\hat{e}_2 + \frac{\rho}{a_2}\left[\frac{\partial\left(a_2\bar{u}_2\right)}{\partial t} + \frac{1}{2}\frac{\partial\bar{u}_2^2}{\partial x_2} + \frac{\bar{u}_1}{a_1}\frac{\partial\left(a_2\bar{u}_2\right)}{\partial x_1} - \frac{\bar{u}_1^2}{a_1}\frac{\partial a_1}{\partial x_2}\right]$$
$$= -\frac{1}{a_2}\frac{\partial P}{\partial x_2} + \frac{1}{a_1 a_2 h}\frac{\partial\left(h a_1\bar{S}_{22}\right)}{\partial x_2} + \frac{1}{h a_1 a_2^2}\frac{\partial}{\partial x_1}\left(h a_2^2\bar{S}_{12}\right) - \frac{1}{a_1 a_2}\frac{\partial a_1}{\partial x_2}\bar{S}_{11} \ , \tag{3.64}$$

$$\rho\left(\frac{\partial^2 \mathbf{r}_0}{\partial t^2} + 2\bar{u}_1\frac{\partial\hat{e}_1}{\partial t} + 2\bar{u}_2\frac{\partial\hat{e}_2}{\partial t}\right)\cdot\hat{e}_3 + \rho\left(\bar{u}_1^2\kappa_1 + \bar{u}_2^2\kappa_2\right) = \frac{-\Delta p + 4\gamma\bar{H}}{h} + \kappa_1\bar{S}_{11} + \kappa_2\bar{S}_{22} \ . \tag{3.65}$$

This concludes our derivation of the leading order equations, that extends the prior work in [96] and [45], through the inclusion of the inertial effects and pressure contributions in

the tangential direction. The addition of these extra terms is important for a number of problems; for instance in sheet retraction the driving force originates in the ∇P term, which was omitted to leading order in the past. The addition of the inertial terms enables us to examine sheet motion at arbitrary Reynolds numbers. Finally, we note the error made by Fliert *et al.* [45] in deriving equation (3.62).

The system of equations (3.63) - (3.65) is completed by the continuity equation (3.57). We thus have 4 equations to solve for the unknown midsurface, h, $\bar{u}_1$ and $\bar{u}_2$. Additional equations and conditions need to be included, if the geometry under consideration is more complex and requires more than one function to be completely determined.

In this thesis, we shall concentrate on axisymmetric sheets. Nonetheless, we note that other geometries can also be considered provided we can parametrize the midsurface using line-of-curvature coordinates at all times. If this is not feasible, the more complicated equations shown in the previous chapter must be considered.

3.7   Unsteady axisymmetric sheets

Here we consider the motion of an unsteady axisymmetric sheet. We can parametrize its center-surface by (see figure 3-1)

$$\mathbf{r}_0 = [R\,(s,t)\cos\phi, R\,(s,t)\sin\phi, F\,(s,t)] \ , \tag{3.66}$$

where s corresponds to the arclength. The parametrization by arclength requires

$$R_s^2 + F_s^2 = 1 \ , \tag{3.67}$$

where the subscript denotes differentiation. The tangent vectors are

$$\mathbf{e}_1 = [R_s\cos\phi, R_s\sin\phi, F_s] \ \Rightarrow a_1 = 1 \ , \tag{3.68}$$

$$\mathbf{e}_2 = [-R\sin\phi, R\cos\phi, 0] \ \Rightarrow a_2 = R \tag{3.69}$$

and the corresponding outward (pointing away from the axis of rotation) unit normal vector is

$$\hat{\mathbf{n}} = \frac{\mathbf{e}_1 \times \mathbf{e}_2}{|\mathbf{e}_1 \times \mathbf{e}_2|} = [-F_s\cos\phi, -F_s\sin\phi, R_s] \ . \tag{3.70}$$

52
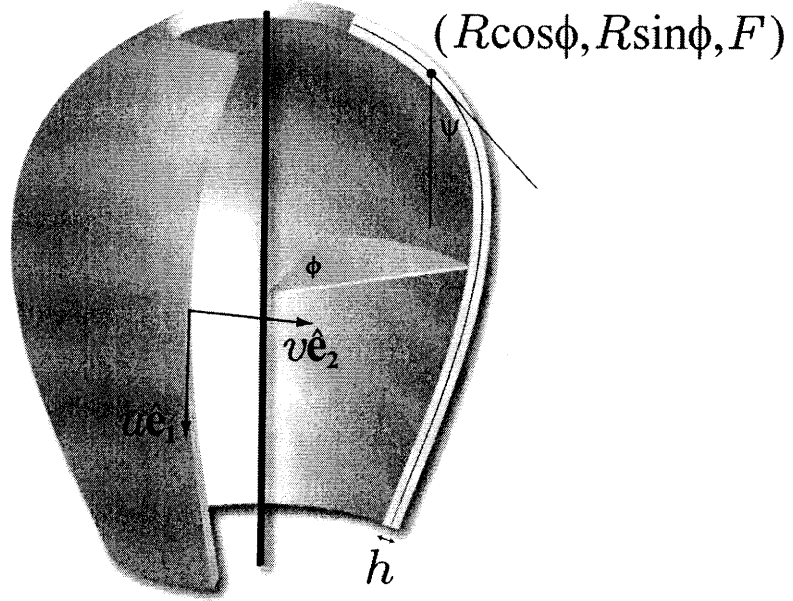
Figure 3-1: Axisymmetric Sheet Geometry

Introducing the angle the tangent makes with the vertical, ψ, we can reduce the complexity of the equations. We thus write:

$$F_s = -\cos\psi \tag{3.71}$$

$$R_s = \sin\psi \ , \tag{3.72}$$

and express the azimuthal κ_1 and axial κ_2 curvatures in terms of ψ as

$$\kappa_1 = \frac{\partial_s \mathbf{e}_1 \cdot \hat{\mathbf{n}}}{\mathbf{e}_1 \cdot \mathbf{e}_1} = \psi_s \ , \tag{3.73}$$

$$\kappa_2 = \frac{\partial_\phi \mathbf{e}_2 \cdot \hat{\mathbf{n}}}{\mathbf{e}_2 \cdot \mathbf{e}_2} = \frac{F_s}{R} = \frac{-\cos\psi}{R} \ . \tag{3.74}$$

Moreover the unit cylindrical coordinate vectors, $\mathbf{e}_z$ and $\mathbf{e}_r$, can be expressed in terms of the vectors $\mathbf{e}_1 = \hat{\mathbf{e}}_1$ and $\hat{\mathbf{n}}$ through

$$\mathbf{e}_r = R_s \hat{\mathbf{e}}_1 - F_s \hat{\mathbf{n}} = \sin\psi \hat{\mathbf{e}}_1 + \cos\psi \hat{\mathbf{n}} \tag{3.75}$$

$$\mathbf{e}_z = F_s \hat{\mathbf{e}}_1 + R_s \hat{\mathbf{n}} = -\cos\psi \hat{\mathbf{e}}_1 + \sin\psi \hat{\mathbf{n}} \ . \tag{3.76}$$

With the help of these expressions we can determine the time derivatives of the surface vectors:

$$\frac{\partial \mathbf{e}_1}{\partial t} = \psi_t \hat{\mathbf{n}} \ , \quad \frac{\partial \mathbf{e}_2}{\partial t} = R_t \hat{\mathbf{e}}_2 \ \text{ and } \ \frac{\partial \hat{\mathbf{n}}}{\partial t} = -\psi_t \hat{\mathbf{e}}_1 \ . \tag{3.77}$$

In the same manner, we determine the velocity and acceleration of the midsurface

$$\frac{\partial \mathbf{r}_0}{\partial t} = \mathbf{V}_0 = (R_t \sin\psi - F_t \cos\psi)\,\hat{\mathbf{e}}_1 + (R_t \cos\psi + F_t \sin\psi)\,\hat{\mathbf{n}} \ , \tag{3.78}$$

$$\frac{\partial^2 \mathbf{r}_0}{\partial t^2} = \frac{\partial \mathbf{V}_0}{\partial t} = (R_{tt} \sin\psi - F_{tt} \cos\psi)\,\hat{\mathbf{e}}_1 + (R_{tt} \cos\psi + F_{tt} \sin\psi)\,\hat{\mathbf{n}} \ . \tag{3.79}$$

Let the velocity of fluid particles on the midsurface relative to the moving coordinate system be:

$$\mathbf{U} = u\hat{\mathbf{e}}_1 + v\hat{\mathbf{e}}_2 \ . \tag{3.80}$$

Thus we have a system of 5 equations in the 5 unknowns F, R, u, v and h :

$$\rho\left(R_{tt}\sin\psi - F_{tt}\cos\psi + \frac{\partial u}{\partial t} + \frac{1}{2}\frac{\partial u^2}{\partial s} - \frac{v^2}{R}\frac{\partial R}{\partial s}\right) = -\frac{\partial P}{\partial s} + \frac{1}{Rh}\frac{\partial\left(hR\bar{S}_{11}\right)}{\partial s}$$
$$- \frac{1}{R}\frac{\partial R}{\partial s}\bar{S}_{22} + \rho g\cos\psi \ , \tag{3.81}$$

$$\rho\left(\frac{\partial\left(Rv\right)}{\partial t} + u\frac{\partial\left(Rv\right)}{\partial s}\right) = \frac{1}{hR}\frac{\partial}{\partial s}\left(hR^2\bar{S}_{12}\right) \ , \tag{3.82}$$

$$\rho\left(R_{tt}\cos\psi + F_{tt}\sin\psi + 2u\psi_t + u^2\psi_s - v^2\frac{\cos\psi}{R}\right) = \frac{-\Delta p + 4\gamma\bar{H}}{h} + \psi_s\bar{S}_{11}$$
$$- \frac{\cos\psi}{R}\bar{S}_{22} - \rho g\sin\psi \ , \tag{3.83}$$

$$\frac{\partial}{\partial t}\left(Rh\right) + \frac{\partial}{\partial s}\left(hRu\right) = 0 \ , \tag{3.84}$$

$$F_s = -\cos\psi \ , \tag{3.85}$$

$$R_s = \sin\psi \ , \tag{3.86}$$

54
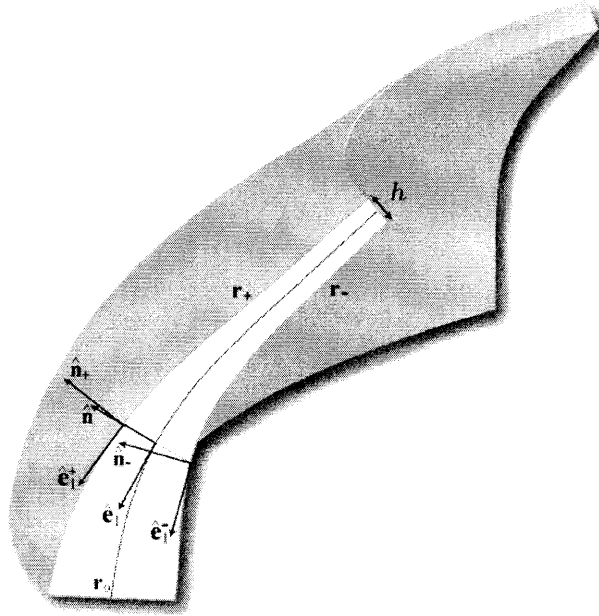
Figure 3-2: Geometry of the outer surfaces

where the stress elements are now:

$$\bar{S}_{11} = \frac{2\mu}{R} \left[\frac{\partial R}{\partial t} + \frac{1}{u} \frac{\partial \left(u^2 R \right)}{\partial s} \right] = \frac{2\mu}{R} \left[\frac{\partial R}{\partial t} + 2R \frac{\partial u}{\partial s} + u \frac{\partial R}{\partial s} \right] , \qquad (3.87)$$

$$\bar{S}_{22} = \frac{2\mu}{R^2} \left[\frac{\partial R^2}{\partial t} + \frac{\partial \left(u R^2 \right)}{\partial s} \right] = \frac{2\mu}{R} \left[2 \frac{\partial R}{\partial t} + R \frac{\partial u}{\partial s} + 2u \frac{\partial R}{\partial s} \right] , \qquad (3.88)$$

$$\bar{S}_{12} = \mu R \frac{\partial \left(v/R \right)}{\partial s} . \qquad (3.89)$$

The principal curvatures of the outer surfaces need to be determined in order to find $\bar{H} = \frac{1}{2} \left(H_+ + H_- \right)$ and $\Delta H = H_+ - H_-$. The leading order expressions for the mean curvatures $H_\pm$ was given in Chapter 2 (see equation (2.63)). To study the effects of highly curved sheets and/or sheets whose thickness varies rapidly, all terms need to be retained. The upper $(+)$ and lower $(-)$ surfaces are (see figure 3-2):

$$\mathbf{r}_\pm = \mathbf{r}_0^\pm \pm \tfrac{1}{2} h \hat{\mathbf{n}} , \qquad (3.90)$$

whose corresponding tangents are given by:

$$\mathbf{e}_1^{\pm} = \left[\left(l_{1\pm} \sin\psi \pm \tfrac{1}{2}h_s \cos\psi \right) \cos\phi, \ \left(l_{1\pm} \sin\psi \pm \tfrac{1}{2}h_s \cos\psi \right) \sin\phi, \ -l_{1\pm} \cos\psi \pm \tfrac{1}{2}h_s \sin\psi \right],$$
(3.91)

$$\mathbf{e}_2^{\pm} = R \left[-l_{2\pm} \sin\phi, l_{2\pm} \cos\phi, 0 \right],$$
(3.92)

where we set

$$l_{1,2\pm} = 1 \mp \tfrac{1}{2}h\kappa_{1,2}.$$
(3.93)

Using (3.91) and (3.92) we can deduce the components of the first fundamental form:

$$a_{11}^{\pm} = \mathbf{e}_1^{\pm} \cdot \mathbf{e}_1^{\pm} = l_{1\pm}^2 + \tfrac{1}{4}h_s^2,$$
(3.94)

$$a_{22}^{\pm} = \mathbf{e}_2^{\pm} \cdot \mathbf{e}_2^{\pm} = R^2 l_{2\pm}^2,$$
(3.95)

$$a_{12}^{\pm} = 0.$$
(3.96)

The normal vectors are

$$\hat{\mathbf{n}}_{\pm} = \frac{\mathbf{e}_1^{\pm} \times \mathbf{e}_2^{\pm}}{|\mathbf{e}_1^{\pm} \times \mathbf{e}_2^{\pm}|} = \frac{1}{\sqrt{a_{11}^{\pm}}} \left[\left(l_{1\pm} \cos\psi \mp \tfrac{1}{2}h' \sin\psi \right) \cos\phi, \right.$$

$$\left. \left(l_{1\pm} \cos\psi \mp \tfrac{1}{2}h' \sin\psi \right) \sin\phi, \ \left(l_{1\pm} \sin\psi \pm \tfrac{1}{2}h' \cos\psi \right) \right].$$
(3.97)

and the derivatives of tangent vectors are:

$$\partial_s \mathbf{e}_1^{\pm} = \left[\left[\left(l_{1\pm s} \mp \tfrac{1}{2}h_s\kappa_1 \right) \sin\psi + \left(l_{1\pm}\kappa_1 \pm \tfrac{1}{2}h_{ss} \right) \cos\psi \right] \cos\phi, \right.$$

$$\left[\left(l_{1\pm s} \mp \tfrac{1}{2}h_s\kappa_1 \right) \sin\psi + \left(l_{1\pm}\kappa_1 \pm \tfrac{1}{2}h_{ss} \right) \cos\psi \right] \sin\phi,$$

$$\left. - \left(l_{1\pm s} \mp \tfrac{1}{2}h_s\kappa_1 \right) \cos\psi + \left(l_{1\pm}\kappa_1 \pm \tfrac{1}{2}h_{ss} \right) \sin\psi \right],$$
(3.98)

$$\partial_\phi \mathbf{e}_2^{\pm} = \left[-Rl_{2\pm} \cos\phi, -Rl_{2\pm} \sin\phi, 0 \right].$$
(3.99)

The second fundamental form is found after some algebra involving equations (3.97)−(3.99):

$$b_{11}^{\pm} = \partial_s \mathbf{e}_1^{\pm} \cdot \hat{\mathbf{n}}_{\pm} = \frac{1}{\sqrt{a_{11}^{\pm}}} \left(\kappa_1 a_{11}^{\pm} \pm \tfrac{1}{2}l_{1\pm}h_{ss} + \tfrac{1}{4}h_s \left(h\kappa_1 \right)_s \right)$$
(3.100)

$$b_{22}^{\pm} = \partial_\phi \mathbf{e}_2^{\pm} \cdot \hat{\mathbf{n}} = -\frac{Rl_{2\pm}}{\sqrt{a_{11}^{\pm}}} \left(l_{1\pm} \cos\psi \mp \tfrac{1}{2}h_s \sin\psi \right)$$
(3.101)

The principal curvatures are thus:

$$
\kappa_1^{\pm} = \frac{b_{11}^{\pm}}{a_{11}^{\pm}} = \frac{\kappa_1}{\sqrt{\left(1 \mp \frac{1}{2}h\kappa_1\right)^2 + \frac{1}{4}h_s^2}} + \frac{h_s\left(h\kappa_1\right)_s \pm 2h_{ss}\left(1 \mp \frac{1}{2}h\kappa_1\right)}{4\left(\left(1 \mp \frac{1}{2}h\kappa_1\right)^2 + \frac{1}{4}h_s^2\right)^{3/2}} \ , \tag{3.102}
$$

$$
\kappa_2^{\pm} = \frac{b_{22}^{\pm}}{a_{22}^{\pm}} = \frac{\kappa_2}{\left(1 \mp \frac{1}{2}h\kappa_2\right)}\frac{\left(1 \mp \frac{1}{2}h\kappa_1\right) \mp \frac{1}{2}h_s \tan\psi}{\sqrt{\left(1 \mp \frac{1}{2}h\kappa_1\right)^2 + \frac{1}{4}h_s^2}} \ . \tag{3.103}
$$

In the limit where $h\kappa_\alpha << 1$, but h_s and h_{ss} are appreciable we find that:

$$
H_+ + H_- = \frac{\left(\kappa_1 + \kappa_2\right)}{\sqrt{1 + \frac{1}{4}h_s^2}} + \frac{h_s\left(h\kappa_1\right)_s}{4\left(1 + \frac{1}{4}h_s^2\right)^{3/2}} \ , \tag{3.104}
$$

$$
H_+ - H_- = \frac{\frac{1}{2}h_{ss}}{\left(1 + \frac{1}{4}h_s^2\right)^{3/2}} - \frac{\frac{1}{2}h_s\kappa_2 \tan\psi}{\sqrt{1 + \frac{1}{4}h_s^2}} \ . \tag{3.105}
$$

This concludes our derivation of the governing equations. In the chapters that follow, we will focus on applying this more general framework to a number of specific physical problems.

Chapter 4

Planar sheet retraction

In this chapter we consider the retraction of a planar, semi-infinite viscous sheet under the influence of surface tension (figure 4-1). Experimental study of the retraction of a planar film is impractical owing to the edge effects [21] and the difficulties inherent in producing a perfectly linear rupture. Nevertheless it is interesting to study this geometry in order to gain physical insights from the relatively simpler governing equations and to make comparisons with the more experimentally feasible circular geometry.

4.1 Introduction
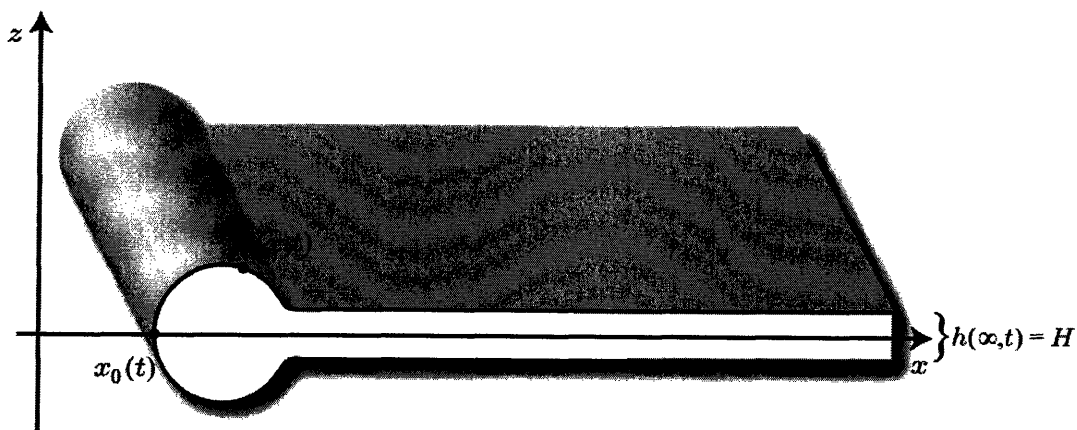
Figure 4-1: Planar Sheet Geometry

Planar sheet retraction has been investigated numerically by a number of authors, begin-

ning with the work of Brenner & Gueyffier [13], who presented a study of a one dimensional lubrication model. For a planar sheet of thickness $h(x, t)$ moving under the influence of curvature forces along the x-axis with speed $u(x, t)$ (figure 4-1), the equations used in [13] follow directly from equations (3.57) and (3.63) by setting $a_1 = a_2 = 1$. We find:

$$u_t + uu_x = \frac{4\mu}{\rho h}(hu_x)_x + \frac{\gamma}{\rho}\kappa_x \ , \tag{4.1a}$$

$$h_t + (hu)_x = 0 \ , \tag{4.1b}$$

where $\kappa(x, t)$ corresponds to the curvature of the film profile,

$$\kappa = \frac{\frac{1}{2}h_{xx}}{\left(1 + \frac{1}{4}h_x^2\right)^{3/2}} \ . \tag{4.2}$$

Brenner & Gueyffier identified three distinct regimes that depend on the Ohnesorge number that characterizes the flow, defined as:

$$\mathrm{Oh} = \frac{\mu}{\sqrt{2H\rho\gamma}} \ , \tag{4.3}$$

Their simulations revealed that in the low Oh regime (Oh < 0.1) capillary waves exist ahead of a retracting rim. For moderate Oh ($0.1 < $ Oh < 10) a rim is present, but no capillary waves form, whereas in the high Oh regime (Oh $\gg 10$) no rims were found in accordance with the observations of Debrégeas et al. [35] (see figure 4-2).

The retraction time scales are different in the high and low Oh regimes. Since numerical simulations indicated that the characteristic speed, u_c, is independent of Oh, the length scale prescribes the characteristic retraction time. Naturally, this length scale is a measure of the distance from the tip over which the film is disturbed and depends on the relative importance of viscosity to surface tension, as quantified through Oh. In the low Oh regime, the motion is primarily concentrated near the tip, so that the characteristic length scale is set equal to H. This implies that the characteristic time scale is

$$\tau_{\mathrm{inv}} = \frac{H}{u_c} = \sqrt{\frac{\rho H^3}{2\gamma}} \ , \tag{4.4}$$

which is in the order of microseconds for the soap films in Ranz's experiments [92]. Conversely, at high Oh, a larger portion of the film is accelerated by the unbalanced curvature

Oh < 0.1

0.1 < Oh < 10

10 < Oh
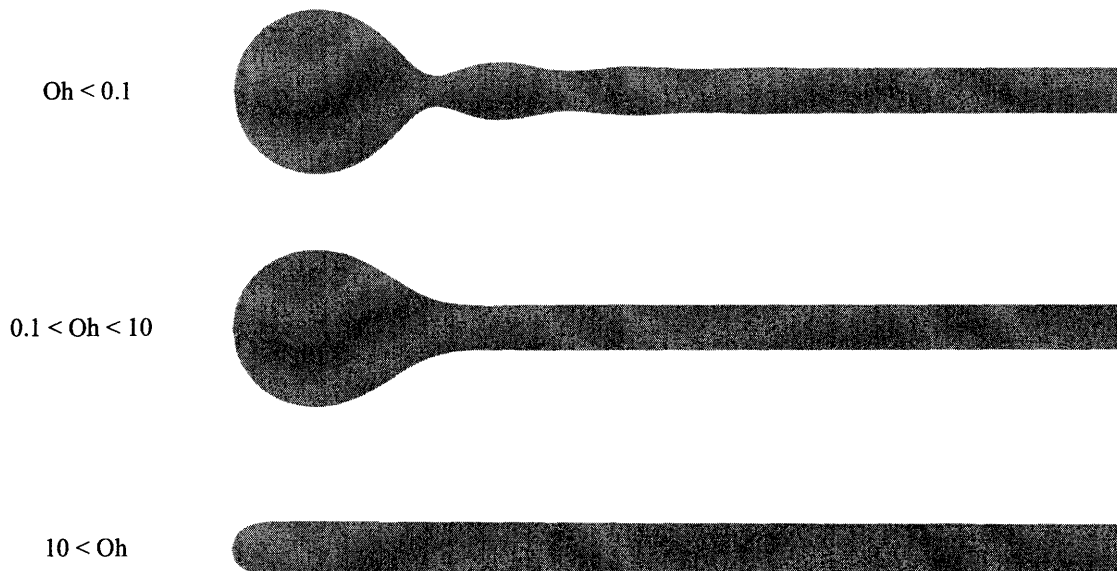
Figure 4-2: Schematic illustration of the three distinct regimes obtained for a retracting sheet [13]. As the Oh progressively increases, the capillary waves and then the rim disappear through the action of viscosity.

near the tip and the flow is characterized by a length scale $\mathrm{Oh}H$. Hence the characteristic retraction time is given by:

$$\tau_{\mathrm{vis}} = \frac{\mathrm{Oh}H}{u_c} = \frac{\mu H}{2\gamma} \ . \tag{4.5}$$

This time was of the order of seconds for Debrégeas' thicker films [35].

Following the work of Brenner & Gueyffier, two-dimensional simulations of planar sheet retraction were presented by Song & Tryggvason [108], who took into account the effect of the ambient fluid. They found that even when the ambient to sheet viscosity is of the order of 0.1, the influence of the ambient fluid is minor. Their results however were somewhat limited due to the short extent of the fluid sheet, and no conclusion could be drawn concerning the dynamics in the long time limit. More recently, Sünderhauf et al. [111] performed two-dimensional simulations of the Navier-Stokes equations, but neglected the ambient fluid on the basis of the prior work of Song & Tryggvason. They focused primarily on exploring the acceleration phase of the film edge towards the terminal Taylor-Culick speed and provided some insights into the stability of falling liquid sheets.

In this chapter we explore further the model of Brenner & Gueyffier [13]. Even though this geometry has been previously considered, several new insights may be obtained. In § 4.2

we present the derivation of the conservation laws and clarify why equation (1.7) adequately describes flow with viscous dissipation, despite the fact that viscosity was neglected in its derivation. In § 4.3 we calculate an analytic expression for the hole growth during the early stages of retraction in the high Oh limit. Finally in § 4.4, we derive a simple analytic formula that gives the maximum thickness of a high Oh film at all times. These new analytic results are compared with numerical solutions.

4.2   Conservation laws

We consider a planar sheet of finite initial length L. At any instant, the edge of the sheet is located at $x_{\text{tip}}(t)$. Imposing the conditions

$$h\left(x_{\text{tip}}, 0\right) = h_x\left(L, t\right) = h_{xx}\left(L, t\right) = 0 \ , \tag{4.6a}$$

$$u\left(L, t\right) = u_x\left(L, t\right) = 0 \ , \tag{4.6b}$$

$$\text{and } h\left(L, t\right) = H \ , \tag{4.6c}$$

we can deduce the conservation laws for the mass, momentum and energy. The total mass of the fluid (per unit length) is:

$$m = \rho \int_{x_{\text{tip}}}^{L} h \ dx \ . \tag{4.7}$$

Mass conservation trivially follows from (4.1b) since

$$\frac{dm}{dt} = \rho \int_{x_{\text{tip}}}^{L} h_t \ dx = -\rho \left. hu \right|_{x_{\text{tip}}}^{L} = 0 \ . \tag{4.8}$$

More importantly, an expression for the total sheet momentum

$$P = \rho \int_{x_{\text{tip}}}^{L} hu \ dx \tag{4.9}$$

can be found by multiplying equation (4.1b) by u and equation (4.1a) by h and adding them together. Making use of

$$h \left(\frac{\frac{1}{2} h_{xx}}{\left(1 + \frac{1}{4} h_x^2\right)^{3/2}} \right)_x = \left(\frac{\frac{1}{2} h h_{xx}}{\left(1 + \frac{1}{4} h_x^2\right)^{3/2}} + \frac{2}{\sqrt{1 + \frac{1}{4} h_x^2}} \right)_x \ , \tag{4.10}$$

61

we obtain the equation

$$(\rho h u)_t + \left(\rho h u^2 - 4\mu h u_x - \gamma h \kappa - 2\gamma \left(1 + \tfrac{1}{4}h_x^2\right)^{-1/2}\right)_x = 0 \ . \tag{4.11}$$

Integrating from x_{tip} to L and making use of (4.6) yields:

$$\frac{dP}{dt} = 2\gamma \ , \tag{4.12}$$

under the assumption that $h_x \to \infty$ as $x \to x_{\mathrm{tip}}$. Hence, we find that even though the dissipation due to viscosity is not directly described by Taylor and Culick's momentum balance, its inclusion does not alter the veracity of their result. With this simple new calculation, we see the role of viscosity in the dynamics of retraction: it affects *how* the momentum is distributed through the film, but does not affect its terminal speed, u_c. As also pointed out in the two-dimensional numerical calculations of Sünderhauf *et al.* [111], in the long time limit $1/2$ of the surface energy is converted to kinetic energy; the other $1/2$ is ultimately dissipated due to viscosity.

To obtain the corresponding energy equation, we multiply equation (4.1*b*) by u^2 and equation (4.1*a*) by hu and add them, which yields:

$$\tfrac{1}{2}\rho \left(h u^2\right)_t + \tfrac{1}{2}\rho \left(h u^3\right)_x = 4\mu u \left(h u_x\right)_x + \gamma u h \kappa_x \ . \tag{4.13}$$

The two terms on the right hand side of (4.13) can be written as:

$$u \left(h u_x\right)_x = \left(u u_x h\right)_x - h u_x^2 \tag{4.14}$$

$$u h \kappa_x = \left(u h \kappa\right)_x - \left(h u\right)_x \kappa = \left(u h \kappa\right)_x + h_t \kappa \ . \tag{4.15}$$

After some manipulation we find that

$$h_t \kappa = \left(\tfrac{1}{2}h_x h_t \left(1 + \tfrac{1}{4}h_x^2\right)^{-1/2}\right)_x - 2\left(\sqrt{1 + \tfrac{1}{4}h_x^2}\right)_t \ , \tag{4.16}$$

which allows us to write

$$\left(\tfrac{1}{2}\rho h u^2 + 2\gamma\sqrt{1 + \tfrac{1}{4}h_x^2}\right)_t + \left(\tfrac{1}{2}\rho h u^3 - 4\mu h u u_x - \gamma u h \kappa - \tfrac{1}{2}\gamma h_x h_t \left(1 + \tfrac{1}{4}h_x^2\right)^{-1/2}\right)_x = -4\mu h u_x^2 \ . \tag{4.17}$$

Integration with respect to x and use of the boundary conditions (4.6) yields

$$\frac{d}{dt}\int_{x_{\rm tip}}^{L}\left(\tfrac{1}{2}\rho h u^2 + 2\gamma\sqrt{1+\tfrac{1}{4}h_x^2}\right)dx = -4\mu\int_{x_{\rm tip}}^{L} h u_x^2\; dx$$
$$-\lim_{x\to x_{\rm tip}}\left(\tfrac{1}{2}\gamma h_x h_t\left(1+\tfrac{1}{4}h_x^2\right)^{-1/2} - 2\gamma\frac{dx_{\rm tip}}{dt}\sqrt{1+\tfrac{1}{4}h_x^2}\right)\;.$$

(4.18)

Using (4.1b), we finally obtain

$$\frac{d}{dt}\left(E_{\rm k} + E_\sigma\right) = -D\;,$$

(4.19)

where we identify

$$E_{\rm k} = \tfrac{1}{2}\rho\int_{x_{\rm tip}}^{L} h u^2\; dx\;,$$

(4.20)

$$E_\sigma = 2\gamma\int_{x_{\rm tip}}^{L}\sqrt{1+\tfrac{1}{4}h_x^2}\; dx\;,$$

(4.21)

$$D = -4\mu\int_{x_{\rm tip}}^{L} h u_x^2\; dx\;,$$

(4.22)

as the total kinetic energy, surface energy and viscous dissipation of the sheet respectively. This argument reveals why Dupré's original argument of balancing surface energy lost and kinetic energy gained by the retracting film predicted an incorrect retraction speed. Culick [31] argued against Dupré's prediction on physical grounds, attributing the discrepancy to the energy lost while the undisturbed film accelerates inelastically to the constant Taylor-Culick speed. We now see that momentum conservation equation nevertheless yields the correct expression for u_c, since the viscous terms dropped out of equation (4.12).

4.3 Early stages of retraction

Assuming that we are in the high Oh regime, we can obtain an analytic expression that describes the initiation of the sheet retraction. Non-dimensionalizing the equations by

$$t \to \tau_{\rm vis}t^*,\quad x \to {\rm Oh}Hx^*,\quad h \to Hh^*\ \text{and}\ u \to u_c u^*\;,$$

we can write the momentum equation in non-dimensional form as

$$u_{t^*}^* + u^* u_{x^*}^* = \frac{4}{h^*} (h^* u_{x^*}^*)_{x^*} + \tfrac{1}{2} \mathrm{Oh}^{-2} \kappa_{x^*}^* \ .$$ (4.23)

If we assume that the fluid sheet consists of a nearly semi-circular cap followed by a straight edge, there occurs a singularity in the curvature at $x_0^* = (2\mathrm{Oh})^{-1}$, since at $t^* = 0$ it satisfies

$$\kappa^* = \begin{cases} 2\mathrm{Oh}^2 & 0 \le x^* < (2\mathrm{Oh})^{-1} \\ 0 & x^* > (2\mathrm{Oh})^{-1} \end{cases} .$$ (4.24)

Therefore we can approximate $\kappa_{x^*}^*$ initially by a delta function

$$\kappa_{x^*}^* = 2\mathrm{Oh}^2 \delta (x - x_0) \ .$$ (4.25)

We further assume that during the initial stages of retraction, the film thickness remains uniform to leading order, x_0^* is small compared to the axial extent of the film, the delta-function structure is preserved in $\kappa_{x^*}^*$, and the semi-circular cap moves at nearly constant speed. We thus reduce the problem to

$$u_t = 4u_{xx} + \delta (x - x_0) \ ,$$ (4.26)

where we have dropped the stars for convenience. These simplifying assumptions are expected to be strictly valid only in the high Oh regime, where the viscous effects dominate and resist the shape change of the fluid film, specifically the development of a pronounced rim.

The velocity is assumed to be continuous, which allows us to integrate equation (4.26) from $x_0 - \varepsilon$ to $x_0 + \varepsilon$ for some $\varepsilon > 0$ small. Taking the limit as $\varepsilon \to 0$ yields a jump condition for u_x :

$$[u_x] = -\tfrac{1}{4} \ .$$ (4.27)

Away from the discontinuity at x_0 (which without loss of generality we set to be $x_0 = 0$) we are left with the heat equation

$$u_t = 4u_{xx} \ , \ x \ge 0 \ ,$$ (4.28)
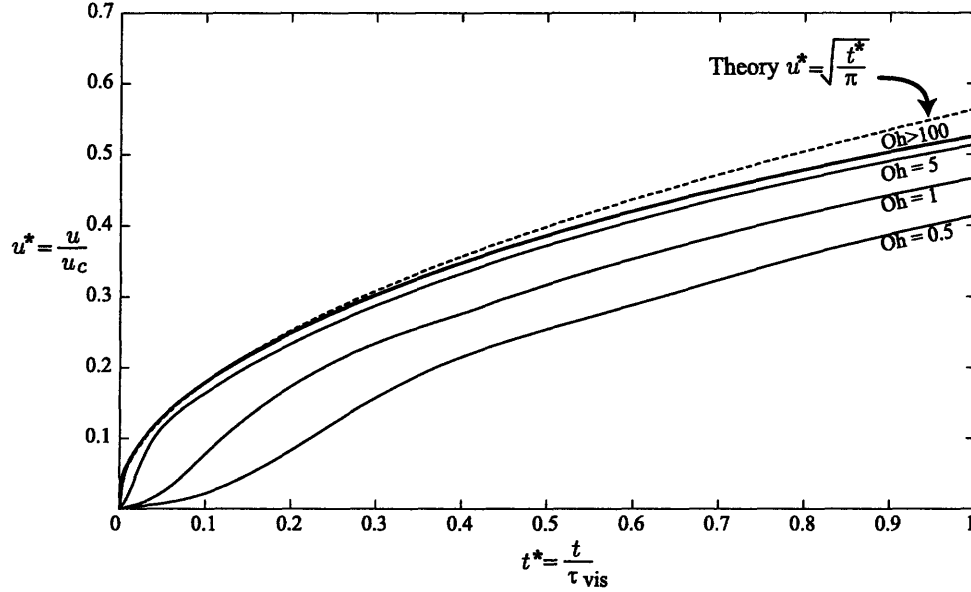
Figure 4-3: Plot of the tip velocity vs time during the early stages of retraction for different Ohnesorge numbers. The plots for Oh = 100, 500, 1000 and 10000 are indistinguishable. The dotted curve shows the theoretical result, equation (4.34), which is in good agreement with numerics up to a time $t \approx 0.4\tau_{\rm vis}$, where $\tau_{\rm vis} = \frac{\mu H}{2\gamma}$.

which we solve subject to the conditions

$$u(x,0) = 0 \ , \tag{4.29}$$

$$u_x(0,t) = -\tfrac{1}{4} \ , \tag{4.30}$$

$$u(x,t) \to 0 \text{ as } x \to \infty \ . \tag{4.31}$$

The condition (4.30) comes from the jump in u_x at x_0 and assumes that there are no velocity gradients within the fluid cap. Defining $\bar{u}$ as the Laplace transform of u, we take the Laplace transform of equation (4.28) to find:

$$\frac{d^2\bar{u}}{ds} - \frac{s}{4}\bar{u} = 0 \Rightarrow \bar{u} = -\tfrac{1}{2}\frac{1}{\sqrt{s}}\exp\left(-\tfrac{1}{2}x\sqrt{s}\right) \ . \tag{4.32}$$

The transform can be inverted by contour integration to yield

$$u(x,t) = -\frac{x}{\sqrt{2\pi}}\int_{x/4t}^{\infty}\frac{e^{-s^2}}{s^2}ds = \sqrt{\frac{t}{\pi}}\exp\left(-\frac{x^2}{16t}\right) - \tfrac{1}{4}x\operatorname{erfc}\left(\frac{x}{4\sqrt{t}}\right) \ . \tag{4.33}$$

65

The speed at the tip is thus

$$u(0,t) = \sqrt{\frac{t}{\pi}},$$

(4.34)

or, in dimensional variables,

$$u(0,t) = u_c \sqrt{\frac{t}{\pi \tau_{\mathrm{vis}}}},$$

(4.35)

which implies that the free edge is located at

$$x_0 = \frac{2}{3\sqrt{\pi}} \left(\frac{t}{\tau_{\mathrm{vis}}}\right)^{3/2} H.$$

(4.36)

In figure 4-3 we show the evolution of the tip speed for various Ohnesorge numbers which verifies the validity of our calculation for short times. This new result supports the idea that the geometry does play an important role in the retraction dynamics as suggested by Brenner & Gueyffier [13]. The edge of a planar film initially recedes with a displacement that scales as $t^{3/2}$ while in the experiments reported in [35], [32] and [99] the retraction of a circular hole follows an exponential law.

Despite our assumptions greatly simplified the problem, the analytical solution obtained matches perfectly the numerical simulations at early times ($t < 0.2t_{\mathrm{vis}}$). At later times, the agreement is quite good with an error of less than 6% at $t \approx t_{\mathrm{vis}}$. Beyond that time, a number of neglected effects become significant, such as h_x and the convective term, thus rendering this approximation invalid.

In figure 4-4 we plot the evolution of the tip speed for various Oh. We see that for films of Oh > 100, the tip speed evolution curves coincide with each other . This behavior could also be inferred from equation (4.26), where Oh dropped out in the end. This observation provides further support that the retraction indeed occurs on the viscous timescale.

4.4   Maximum film thickness

In the high Oh limit, no visible rim forms as the sheet retracts; therefore, by mass conservation, the film thickness must increase with time. To find the maximum film thickness, $h_m(t)$, we examine equation (4.23). We assume that the semi-circular cap is preserved at
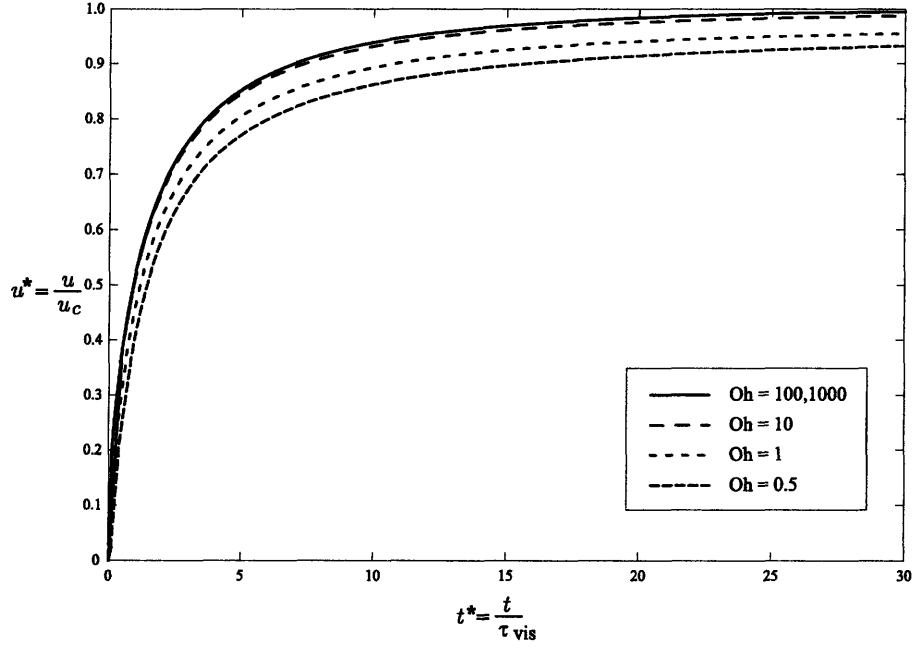
Figure 4-4: Velocity of the film edge for different Ohnesorge numbers. In the high Oh limit the velocity curves coincide with each other.

all times. The non-dimensional curvature is thus assumed to be

$$
\kappa^* = \begin{cases} \dfrac{2\mathrm{Oh}^2}{h_m^*(t)} & 0 \le x^* < \tfrac{1}{2}h_m^*(t)/\mathrm{Oh} \\ 0 & x^* > \tfrac{1}{2}h_m^*(t)/\mathrm{Oh} \end{cases} \qquad (4.37)
$$

The maximum film thickness is expected to be at the point of discontinuity in curvature, the center of the semi-circular cap, where $x_0^* = \tfrac{1}{2}h_m^*(t)/\mathrm{Oh}$. Plugging this expression for κ^* into equation (4.23), integrating over an interval around x_0^* and shrinking it to zero yields the jump condition at x_0^*:

$$
[h^* u_{x^*}^*] = -\frac{1}{4} . \qquad (4.38)
$$

Just to the right of x_0^*, we use mass conservation (4.1b) and the jump condition (4.38) to find

$$
h_m(t) = H\left(1 + \tfrac{1}{4}\frac{t}{\tau_{\mathrm{vis}}}\right) , \qquad (4.39)
$$

where H is the initial film thickness. The linear increase in film thickness is confirmed with the numerical results shown in figure 4-5. Since in a numerical solution having a discon-

67
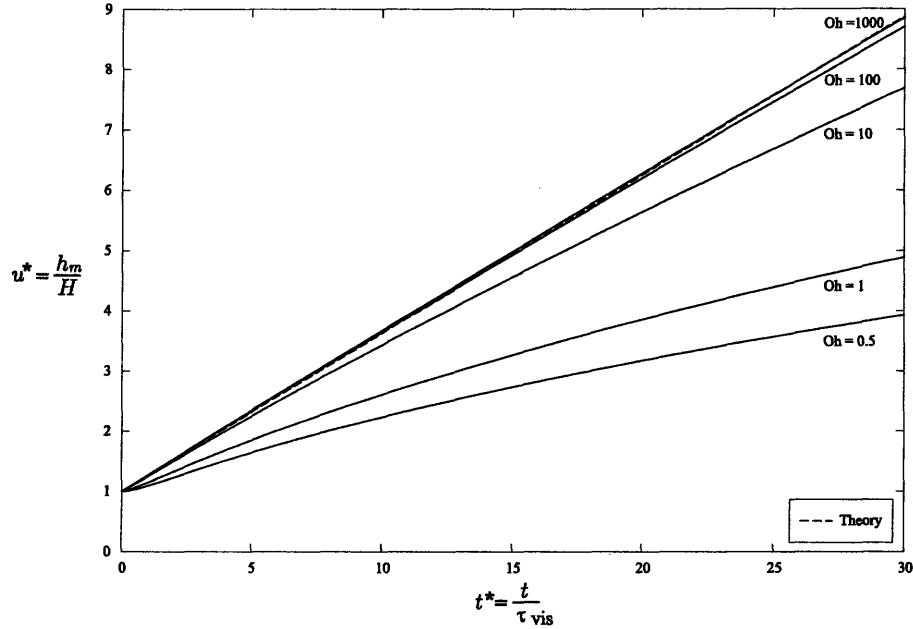
Figure 4-5: Maximum film thickness, h_m, vs time for different Ohnesorge numbers. In the high Oh limit, h_m grows linearly in time, confirming the theory represented by the dotted line. The numerical results correspond to profiles with $\kappa_0 = 2.1$.

tinuity in curvature would complicate its implementation, we smooth the initial curvature gradient as discussed in Appendix B. The slope of the line is corrected to account for this smoothing by writing:

$$h_m = H \left(1 + \tfrac{1}{8} H \kappa_0 \frac{t}{\tau_{\text{vis}}} \right) , \tag{4.40}$$

where κ_0 corresponds to the initial curvature at the tip. It is also important to note here the difference with the low Oh regime films, where one finds through mass conservation that the maximum film thickness, or in other words the rim radius, evolves according to $\sqrt{t/t_{\text{inv}}}$.

In summary, we clarified through directly manipulating the lubrication equations how the momentum balance obtained in terms of an inviscid theory by Taylor [114] and Culick [31] can be similarly obtained for arbitrary viscosities. Moreover, by making some simplifying assumptions made for the high Oh films, we were able to obtain new analytical expressions for the rate of retraction during the initial stages of the motion the maximum film thickness as a function of time. These results will be built upon and extended in our consideration of circular sheet retraction in Chapter 5.

Chapter 5

Circular sheet retraction

We now turn our attention to the retraction of flat films that move owing to the unbalanced surface tension force that results from nucleating a hole of radius R_0 at time $t = 0$. This configuration is easily achieved in the laboratory with the bursting of a soap film (see figure 5-1). To complement the numerous experimental studies on film rupture (e.g. [77], [92], [35]), we develop a new theoretical model that allows us to investigate the film motion for arbitrary Ohnesorge numbers.
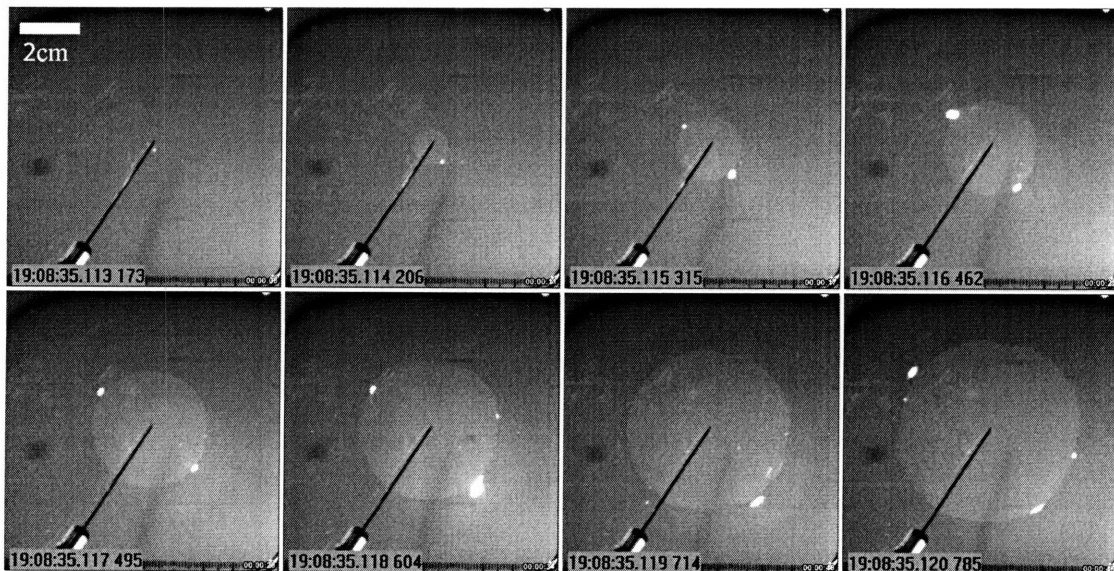
Figure 5-1: Frames taken from the bursting of a soap film. Time increases from left to right and from top to bottom. The times are indicated at each frame. The retraction process lasts about 7.6 ms.

5.1 Introduction
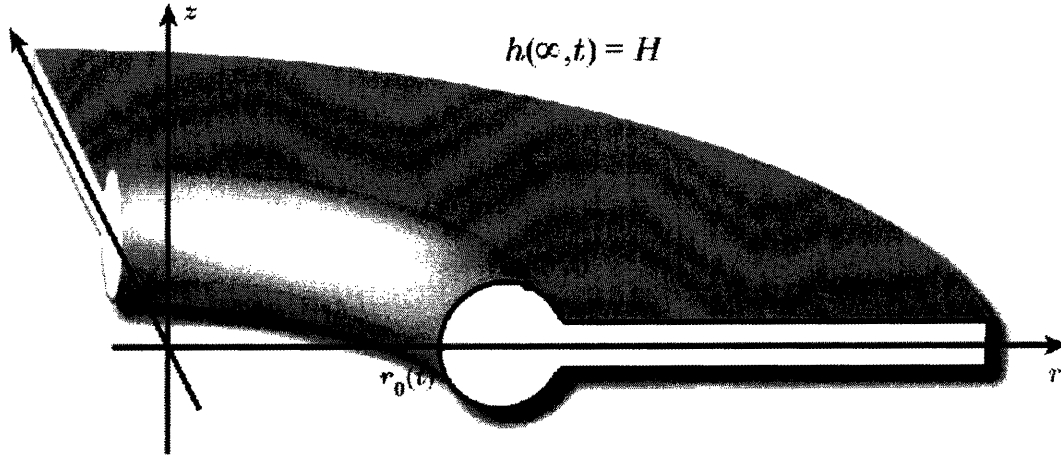
Figure 5-2: Circular Sheet geometry

As in the planar case considered in Chapter 4, we assume that the film thickness $h(r,t)$ varies slowly with r and so describe the equations of motion with the lubrication model derived in Chapter 3. In particular, we set $a_1 = 1$ and $a_2 = x_1 = r$ in the continuity (3.57) and momentum (3.63) equations to find:

$$h_t + \frac{1}{r}\left(hur\right)_r = 0, \tag{5.1a}$$

$$u_t + uu_r = \frac{4\mu}{h\rho}\left[\left(\frac{h}{r}\left(ru\right)_r\right)_r - \frac{u}{2r}h_r\right] + \frac{\gamma}{\rho}\kappa_r, \tag{5.1b}$$

where $u(r,t)$ is the radial sheet speed and $\kappa(r,t)$ is the curvature of the film profile, given by equation (2.67), namely:

$$\kappa(r,t) = \frac{h_{rr}}{2\left(1 + \frac{1}{4}h_r^2\right)^{3/2}} + \frac{h_r}{2r\left(1 + \frac{1}{4}h_r^2\right)^{1/2}}. \tag{5.2}$$

We note here that the azimuthal dependence in our model was neglected on the basis of the experiments of Debrégeas *et al.* [35], who confirmed that the resulting motion is purely radial via particle tracking.

Holes in thin films do not necessarily open, because the second term in equation (5.2), the azimuthal curvature, acts in opposition to the hole expansion. The only possible stationary configuration would arise when the free surface has the shape of a *catenoid*, which has zero

70

curvature everywhere. For the hole to expand radially, the force due to surface tension, $\gamma \kappa_r$, must be positive at the tip. However, when we have that

$$\tfrac{1}{2}H < R_0 < H \ , \tag{5.3}$$

it easy to verify that $\kappa_r < 0$ at the tip, meaning that a hole of this size will contract and eventually close itself and film rupture would not take place. We note that similar criteria for the stability to film puncture were established by Taylor & Michael [118]. We shall henceforth proceed by considering configurations for which holes will grow.

The governing equations are not amenable to extensive analytical work, so we will begin in § 5.2 by following the argument of Debrégeas [35], that describes the dynamics in the high Ohnesorge number limit during the early stages of retraction. We then proceed in § 5.3 by describing our numerical procedure and in § 5.4 we present our results. The chapter concludes in § 5.5 where we present a discussion of three-dimensional effects that were neglected in the present model.

5.2 Early stages of retraction

In the high Oh limit, viscous stresses dominate inertia and curvature. Non-dimensionalizing the equations as in (5.11b) and away from the hole, where both κ_r and h_r are assumed negligible, (5.1b) can be approximated as

$$(ru)_r \sim 0 \quad \Rightarrow \quad u\left(r\right) = \frac{\dot{r}_0 r_0}{r} \ , \tag{5.4}$$

where $r_0\left(t\right)$ corresponds to the radius of the punctured hole and the dot denotes differentiation with respect to time. Since the surface energy is

$$E_s = 4\pi\gamma \int_{r_0}^{\infty} r\sqrt{1 + \tfrac{1}{4}h_r^2} \, dr \approx 4\pi\gamma \int_{r_0}^{\infty} r dr \ , \tag{5.5}$$

its rate of change during retraction is simply

$$\dot{E}_s = 4\pi\gamma r_0 \dot{r}_0 \ . \tag{5.6}$$

In the viscous limit, the surface energy is primarily dissipated within the film through the action of viscosity. The viscous dissipation Φ_V is thus:

$$\Phi_V = 2\pi H \int_{r_0}^{\infty} (\boldsymbol{\sigma} : \nabla \mathbf{u})\, r\, dr = 4\pi \mu H \int_{r_0}^{\infty} \left(u_r^2 + u^2/r^2 \right)^2\, dr = 4\pi \mu H \dot{r}_0^2 \ . \tag{5.7}$$

Energy conservation yields an expression that gives the radius of the punctured hole as a function of time. Specifically, $\dot{E}_s = \Phi_V$ implies that:

$$\frac{\dot{r}_0}{r_0} = \frac{\gamma}{\mu H} \ , \tag{5.8}$$

from which we can deduce

$$r_0\,(t) = R_0 e^{\frac{t}{2\tau_{\text{vis}}}} \ , \tag{5.9}$$

where $\tau_{\text{vis}} = \frac{1}{2}\mu H/\gamma$. Equation (5.9), initially obtained by Debrégeas et $al.$ [35], can be contrasted with their experimental observations that also yield an exponential retraction rate:

$$r_{0_{\text{exp}}}\,(t) = R_0 \exp \left(\frac{t}{1.4\tau_{\text{vis}}} \right) \ . \tag{5.10}$$

The difference in the exponents in equations (5.9) and (5.10) will be considered in section 5.4.1, where we shall demonstrate that it may be ascribed to the initial film profile. Despite the fact that Debrégeas et $al.$ did not resort to viscoelasticity theory to obtain equation (5.9), they suggested that the exponential behavior may be due to the viscoelasticity of the films. It is now clear however, that the exponential behavior need not be attributed to viscoelastic effects; rather, it is a generic feature of the circular hole retraction in a viscous sheet.

5.3 Numerical method

Before presenting our results, we describe the finite difference scheme used to solve the system of equations (5.1). In § 5.3.1, we introduce the two different ways used to non-dimensionalize the governing equations, based on the Ohnesorge number. We then proceed in § 5.3.2, where we explain the domain mapping transformation that maps the tip location to the origin of our computational domain. In § 5.3.3, we derive the equation used at the tip and conclude with § 5.3.4, where we present the discretization of the equations on a

staggered grid.

5.3.1 Non-dimensionalization of the governing equations

In non-dimesionalizing the governing equations (5.1) the timescale is chosen according to the Ohnesorge number. By selecting the larger timescale of the two, τ_{inv} and τ_{vis} , we facilitate the computations, since with the same computational cost, we can integrate the equations further in physical time. Given that $\tau_{\text{vis}} = \text{Oh}\tau_{\text{inv}}$, when $\text{Oh} < 1$, the flow is primarily dominated by inertia and the appropriate retraction timescale is given by τ_{inv} as defined in equation (4.4). By introducing the scalings $t = \tau_{\text{inv}}t^*$, $u = u_c u^*$, $h = Hh^*$ and $r = Hr^*$, equations (5.1a), (5.1b) and (5.2) may be written in non-dimensional form:

$$h_{t^*}^* + \frac{1}{r^*}(h^*u^*r^*)_{r^*} = 0, \tag{5.11a}$$

$$u_{t^*}^* + u^*u_{r^*}^* = \frac{4\text{Oh}}{h^*}\left[\left(\frac{h^*}{r^*}(r^*u^*)_{r^*}\right)_{r^*} - \frac{u^*}{2r^*}h_{r^*}^*\right] + \frac{1}{2}\kappa_{r^*}^*, \tag{5.11b}$$

$$\kappa^* = \frac{h_{r^*r^*}^*}{2\left(1 + \frac{1}{4}h_{r^*}^{*2}\right)^{3/2}} + \frac{h_{r^*}}{2r^*\left(1 + \frac{1}{4}h_{r^*}^{*2}\right)^{1/2}}. \tag{5.11c}$$

Conversely, when $\text{Oh} > 1$, using the scalings $t = \tau_{\text{vis}}t^*$, $u = u_c u^*$, $h = Hh^*$ and $r = \text{Oh}Hr^*$ yields the system:

$$h_{t^*}^* + \frac{1}{r^*}(h^*u^*r^*)_{r^*} = 0, \tag{5.12a}$$

$$u_{t^*}^* + u^*u_{r^*}^* = \frac{4}{h^*}\left[\left(\frac{h^*}{r^*}(r^*u^*)_{r^*}\right)_{r^*} - \frac{u^*}{2r^*}h_{r^*}^*\right] + \frac{1}{2\text{Oh}^2}\kappa_{r^*}^*, \tag{5.12b}$$

$$\kappa^* = \frac{h_{r^*r^*}^*}{2\left(1 + \frac{1}{4\text{Oh}^2}h_{r^*}^{*2}\right)^{3/2}} + \frac{h_{r^*}}{2r^*\left(1 + \frac{1}{4\text{Oh}^2}h_{r^*}^{*2}\right)^{1/2}}. \tag{5.12c}$$

At the far end of the film $(r \to \infty)$, Neumann conditions are used for the thickness. For the velocity, we use either a Dirichlet or a Neumann condition depending on whether we pin the film at the far end of the domain. As far as the initial film profile is concerned, we use

$$h^*(r^*, 0; \alpha) = \sqrt{1 - \left(\frac{1}{2} - \alpha - (r^* - r_0^*) + \frac{1}{2}\sqrt{(1 + 2\alpha)^2 + 4(r^* - r_0^*)(2\alpha + r^* - r_0^* - 1)}\right)^2}, \tag{5.13}$$

where α is a parameter that controls the curvature profile and $r^* \geq r_0^*$. In Appendix B, we justify our choice of this profile.

5.3.2 Computational domain mapping

Equations (5.11) and (5.12) are rearranged to solve for $f = h^2/4$, because the slope of h, which goes like $\sqrt{r - r_0(t)}$ near the tip, becomes infinite there. Doing so avoids the difficulties in taking the derivatives of h to evaluate the curvature at the tip, which now transforms to:

$$\kappa = 2\frac{2ff_{rr} - f_r^2}{(4f + f_r^2)^{3/2}} + \frac{f_r}{r(4f + f_r^2)^{3/2}}. \tag{5.14}$$

In their examination of jet breakup, Eggers & Dupont [43] remedied the difficulty of h_r blowing up at the tip by fitting an even quartic polynomial to the jet profile in this region. Our approach is more natural in terms of implementation as the discretization of the equations is done without resorting to polynomial fits.

Since this is a free boundary problem, where the tip of the film moves, solving the system of equations (5.1a) and (5.1b) requires the remeshing of the domain at each time step. To avoid this difficulty, we map the computational domain (r', t') to the physical (r, t)-plane via the transformation

$$r = \left(1 - \frac{r_0(t)}{L}\right)r' + r_0(t) \ , \tag{5.15a}$$

$$t = t' \ , \tag{5.15b}$$

where $0 < r' < L$ and L is the radial extent of the film. We note that this approach was previously employed by Zhang [131], who studied the run-up of ocean waves on a sloping beach. Under this mapping, the edge of the film is always located at $r' = 0$ in the computational domain and $r = L$ is mapped to $r' = L$; the free boundary problem is thus transformed into a fixed boundary problem.

The derivatives must be transformed accordingly by

$$\frac{\partial}{\partial t} = \frac{\partial}{\partial t'} - \frac{1 - r'/L}{1 - r_0(t)/L}u_0(t)\frac{\partial}{\partial x'} \ , \tag{5.16}$$

$$\frac{\partial}{\partial x} = \frac{1}{1 - r_0(t)/L}\frac{\partial}{\partial x'} \ , \tag{5.17}$$

where the tip speed

$$u_0 = \frac{dr_0}{dt}. \tag{5.18}$$

Dropping the primes, the mapping given by equations (5.15) transforms the system of equations (5.1a) and (5.1b) into:

$$f_t/c + (u - (1 - r/L) u_0) f_r + 2fu_r + \frac{2fu}{r + r_0c} = 0, \qquad (5.19a)$$

$$u_t + c(u - (1 - r/L) u_0) u_r = \frac{4\mathrm{Oh}}{f} c^2 \left[\left(\frac{f}{r + r_0c} (ru)_r \right)_r - f_r \left(\tfrac{1}{2} u_r + \tfrac{3}{4} \frac{u}{r + r_0c} \right) \right] + \frac{1}{2} c\kappa_r, \qquad (5.19b)$$

$$\kappa = c^2 \left(2 \frac{2ff_{rr} - f_r^2}{(4f + c^2 f_r^2)^{3/2}} - \frac{f_r}{(r + r_0c)(4f + c^2 f_r^2)^{3/2}} \right), \qquad (5.19c)$$

where

$$c(t) = \frac{1}{1 - r_0(t)/L}. \qquad (5.20)$$

Equations (5.19) together with (5.18) constitute a hybrid Lagrangian-Eulerian system. The computational domain for $r \neq 0$ is prescribed by a Eulerian formulation. The tip, however, is treated as a Lagrangian point, and this requires an additional equation, which we derive next.

5.3.3 Tip condition

In order to obtain the appropriate boundary condition at the film edge, the governing equations are alternatively derived by means of a Taylor expansion. This idea was previously introduced in the past to study slender geometries that arise in jet breakup (Eggers and Dupont [43], Eggers and Brenner [42]). Assuming symmetry about $z = 0$ we write

$$U(r, z, t) = u(r, t) + u_2(r, t) z^2 + \dots , \qquad (5.21a)$$

$$V(r, z, t) = v_1(r, t) z + v_3(r, t) z^3 + \dots, \qquad (5.21b)$$

$$p(r, z, t) = p_0(r, t) + p_2(r, t) z^2 + \dots, \qquad (5.21c)$$

where p is the pressure and U and V are the radial and normal velocity components respectively. Matching powers of z in the continuity equation,

$$\partial_r (Ur) + \partial_z (Vr) = 0 , \qquad (5.22)$$

75
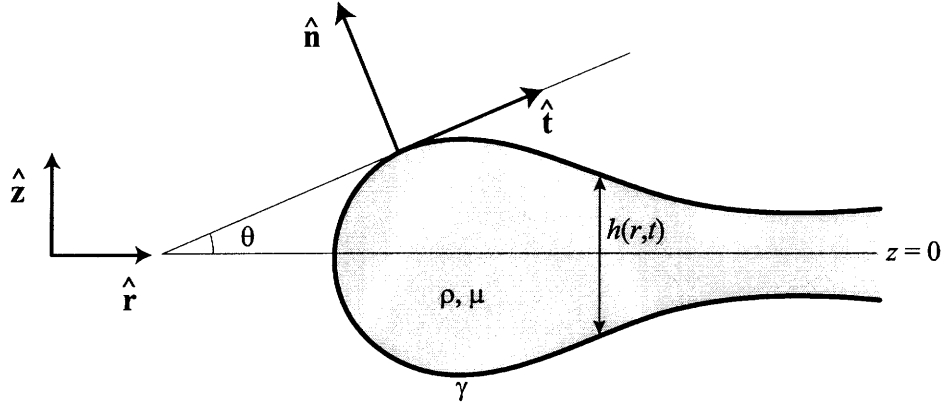
Figure 5-3: Orientation of vectors for the stress balance equations (5.29) and (5.30).

we find that

$$v_1 = -\left(\partial_r u + \frac{u}{r}\right) , \tag{5.23}$$

$$v_3 = -\tfrac{1}{3}\left(\partial_r u_2 + \frac{u_2}{r}\right) . \tag{5.24}$$

Similarly, the momentum equations

$$\partial_t U + U\partial_r U + V\partial_z U = -\partial_r p/\rho + \nu\left(\partial_r^2 U + \partial_z^2 U + \partial_r U/r - U/r^2\right) , \tag{5.25}$$

$$\partial_t V + U\partial_r V + V\partial_z V = -\partial_z p/\rho + \nu\left(\partial_r^2 V + \partial_z^2 V + \partial_r V/r\right) , \tag{5.26}$$

yield

$$\partial_t u + u\partial_r u = -\partial_r p_0/\rho + \nu\left(\partial_r^2 u + \partial_r u/r - u/r^2 + 2u_2\right) , \tag{5.27}$$

$$\partial_t v_1 + u\partial_r v_1 + v_1^2 = -2p_2/\rho + \nu\left(\partial_r^2 v_1 + \partial_r v_1/r + 6v_3\right) . \tag{5.28}$$

The stress balance equations at the boundary $z = h\left(r,t\right)/2 = \sqrt{f\left(r,t\right)}$ are:

$$\hat{\mathbf{n}} \cdot \mathbf{T} \cdot \hat{\mathbf{n}} = \gamma\nabla\cdot\hat{\mathbf{n}} \Rightarrow -\frac{p}{\rho} + 2\nu\left[\partial_r U \sin^2\theta - (\partial_r V + \partial_z U)\sin\theta\cos\theta + \partial_z V \ \cos^2\theta\right] = \frac{\gamma}{\rho}\kappa , \tag{5.29}$$

$$\hat{\mathbf{n}} \cdot \mathbf{T} \cdot \hat{\mathbf{t}} = 0 \Rightarrow \ 2\left(\partial_z V - \partial_r U\right)\sin\theta\cos\theta + \left(\partial_r V + \partial_z U\right)\left(\cos^2\theta - \sin^2\theta\right) = 0 , \tag{5.30}$$

76

where $\hat{n}$ and $\hat{t}$ correspond to the unit normal and tangent vectors of the surface, $\mathbf{T}$ is the stress tensor, and $\partial_r h = 2\tan\theta$ is the slope of the interface (see figure 5-3). In the long wavelength limit, $f \gg \partial_r f$ we find that to leading order in f:

$$-\frac{p}{\rho} = \frac{\gamma}{\rho}\kappa - 2\nu v_1 \ , \tag{5.31}$$

$$2u_2 = -\frac{\partial_r f}{f}\left(v_1 - \partial_r u\right) - \partial_r v_1 \ . \tag{5.32}$$

Substitution of equations (5.31) and (5.32) into (5.27) yields the equations governing circular sheet retraction presented in (5.1). However this long-wavelength approximation is not valid everywhere and the equations become singular as we approach the film tip. Similar difficulties arise in various applications of the lubrication approximation; nevertheless, such models perform surprisingly well. For instance, in Eggers and Dupont [43], the lubrication model yields excellent agreement with the actual experiments of jet breakup and pendant drop formation. In Barenblatt *et al.* [4], a similar issue is encountered for the spreading of the film on a solid substrate, and the failure of the lubrication equations near the contact line is treated by introducing an *autonomous contour region,* which is assumed to be moving at a speed that does not vary within that region. The free boundary problem is then solved by assuming that this region is much smaller than the region where the lubrication approximation holds and by introducing some matching conditions between these two regions.

In Eggers' work, the failure of the lubrication approximation is remedied by 'switching-off' the effect of viscosity near the tip (personal communication with the author). In the jet breakup problem, the condition at the jet tip is apparently not critical. Nevertheless, choosing the appropriate tip condition is crucial here and needs to be addressed more carefully. We see that when $\theta = \pi/2$ and $h = 0$, equation (5.30) is trivially satisfied no matter what u_2 is. Hence we infer u_2 by extrapolating over the values of u_2 in the interior, found using equation (5.32). Quadratic extrapolation yields:

$$u_2|_{\text{tip}} = \frac{x_1 x_2 \left(x_2 - x_1\right) u_{2,3} + x_1 x_3 \left(x_1 - x_3\right) u_{2,2} + x_2 x_3 \left(x_3 - x_2\right) u_{2,1}}{x_1 x_2 \left(x_2 - x_1\right) + x_1 x_3 \left(x_1 - x_3\right) + x_2 x_3 \left(x_3 - x_2\right)} \ , \tag{5.33}$$

where $x_i = r_i - r_0$ is the $(i+1)$-st node in the computational grid at which u_2 takes the
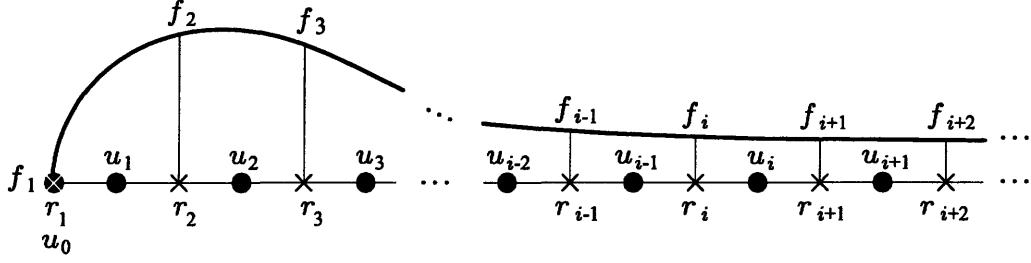
Figure 5-4: The staggered grid used for the computation. The values of f_i are prescribed at the mesh points r_i and the values of u_i are prescribed at $(r_i + r_{i+1})/2$.

value $u_{2,i}$. Substituting $\theta = \pi/2$ and $f = 0$ in (5.29) gives

$$-\left.\frac{p}{\rho}\right|_{\text{tip}} = \frac{\gamma}{\rho}\kappa - 2\nu\partial_r u_0 \tag{5.34}$$

Using equation (5.34) in (5.27), we find that the velocity at the film edge evolves according to:

$$\frac{du_0}{dt} = \frac{\gamma}{\rho}\partial_r\kappa + 2\nu\left(-\partial_{rr}u_0 + \frac{\partial_r u_0}{r} - \frac{u_0}{r^2} + u_2\right)\bigg|_{\text{tip}} . \tag{5.35}$$

The presence of the viscous term is essential here. Had we followed Eggers' remedy, the absence of viscosity at the tip causes the hole to expand at a faster rate.

5.3.4 Finite difference scheme

Following Eggers and Dupont, [43], the numerical solution of equations (5.18), (5.19) and (5.35) was implemented with a centered finite difference scheme on a staggered mesh over the interval $0 \leq r \leq L$. Implementation with a non-staggered grid introduced spurious oscillations in the curvature in the long time limit. Note that similar spurious oscillations occur in the pressure field, when the Navier-Stokes equations are solved by prescribing all velocities and pressures at the nodes of a cartesian grid [126]. In general, we use a smoothly varying, non-uniformly spaced mesh

$$0 = r_0 < r_2 < \ ... \ < r_{N-1} = L , \tag{5.36}$$

78

and solve at each timestep for f_i, the square of the thickness at $r = r_i$ and for u_i, the film speed $r = r_{i+1/2} = (r_i + r_{i+1})/2$ (see figure 5-4). Defining

$$\Delta r_i = r_{i+1} - r_i \ , \tag{5.37}$$

$$\Delta r_{i+1/2} = r_{i+1/2} - r_{i-1/2} \ , \tag{5.38}$$

we discretize the equation for h_i, (5.19a), at each point r_i and the equation for u_i, (5.19b), at each point $r_{i+1/2}$. Doing so, we define

$$
\begin{aligned}
Q_i\left(\mathbf{h}, \mathbf{u}\right) &= \left[\frac{\Delta r_{i-1} u_i + \Delta r_i u_{i-1}}{\Delta r_i + \Delta r_{i-1}} - \left(1 - \frac{r_i}{L}\right) u_0 \right] \\
&\quad + 2 f_i \frac{u_i - u_{i-1}}{\Delta r_i - \Delta r_{i-1}} + \frac{2 f_i}{r_i + r_0 c} \frac{\Delta r_i u_{i-1} + \Delta r_{i-1} u_i}{\Delta r_i + \Delta r_{i-1}} \ , \\[2mm]
W_i\left(\mathbf{h}, \mathbf{u}\right) &= c \left(u_i - \left(1 - \frac{r_{i+1/2}}{L}\right) u_0 \right) \frac{u_{i+1} - u_{i-1}}{\Delta r_{i+1/2}} - \frac{1}{2} c \frac{\kappa_{i+1} - \kappa_i}{\Delta r_i} \\[2mm]
&\quad - \frac{8 \mathrm{Oh} c^2}{f_i + f_{i+1}} \left[\frac{1}{\Delta r_i} \left[\frac{f_i}{r_i + r_0 c} \frac{r_{i+3/2} u_{i+1} - r_{i+1/2} u_i}{\Delta r_{i+1/2}} - \frac{f_{i-1}}{r_{i-1} + r_0 c} \frac{r_{i+1/2} u_i - r_{i-1/2} u_{i-1}}{\Delta r_{i-1/2}} \right] \right. \\[2mm]
&\quad \left. - \frac{f_{i+1} - f_i}{\Delta r_i} \left(\frac{1}{2} \frac{u_{i+1} - u_{i-1}}{\Delta r_{i+1/2}} + \frac{3 u_i}{4 \left(r_{i+1/2} + r_0 c\right)} \right) \right] \ ,
\end{aligned}
$$

$$\tag{5.39}$$
$$\tag{5.40}$$

where the curvatures κ_i are formed as the usual second order centered finite differences, defined at the mesh points r_i. Time integration was performed with the implicit θ−weighted finite difference scheme:

$$\frac{f_i^t - f_i^{t-\delta t}}{\delta t} - \theta Q_i\left(\mathbf{h}^t, \mathbf{u}^t\right) + \left(\theta - 1\right) Q_i\left(\mathbf{h}^{t-\delta t}, \mathbf{u}^{t-\delta t}\right) = 0 \ , \tag{5.41a}$$

$$\frac{u_i^t - u_i^{t-\delta t}}{\delta t} - \theta W_i\left(\mathbf{h}^t, \mathbf{u}^t\right) + \left(\theta - 1\right) W_i\left(\mathbf{h}^{t-\delta t}, \mathbf{u}^{t-\delta t}\right) = 0 \ , \tag{5.41b}$$

where $\mathbf{h}^t$ and $\mathbf{u}^t$ correspond to the solution vectors at time t and δt is the time step of the computation. In order to solve the resulting system (5.41), we use a matrix-free Newton-Krylov method, described in Appendix A.

5.4 Results and discussion

We now present the results of our computations. Even though we explored a wide range of Oh, particular attention was given to the high Oh regime, in order to make comparisons
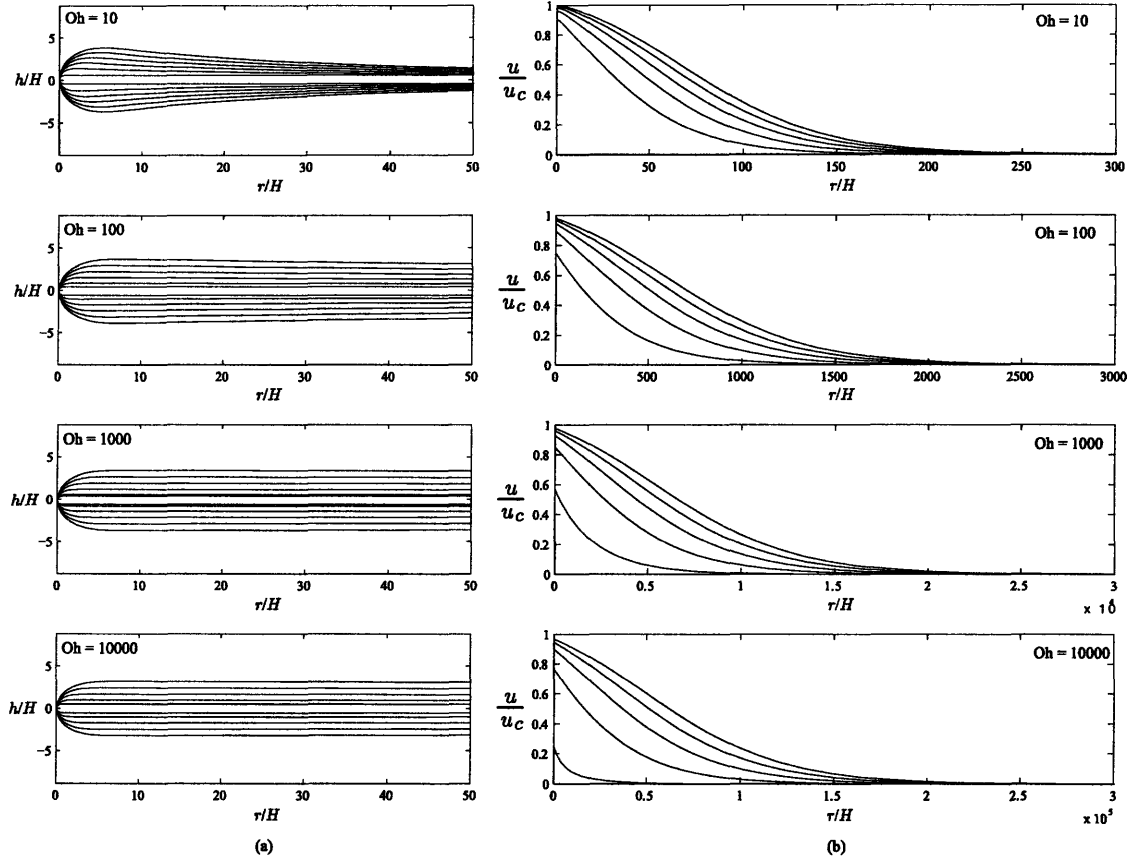
Figure 5-5: Evolution of the film boundaries and midplane velocities for high Oh and initial hole size $R_0 = 50H$ in time increments of $\delta t = 10$ τ_{vis}. Distances are scaled by the film thickness, H. As Oh is progressively increased from 10 to 10^4 the rim becomes less pronounced and diffuses towards the bulk. At the same time, the region of influence of the disturbance caused by the tip motion extends further into the film and is proportional to Oh.

with the recently reported experimental work (e.g. [35], [32], [99]). The regimes identified in the work of Brenner & Gueyffier [13] are also present in the retraction of circular sheets (figure 4-2). While the differences between the two geometries are not significant at low Oh, there are striking differences in the retraction dynamics in the high Oh regime. For the sake of clarity of the presentation, we devote sections § 5.4.1, § 5.4.2 and § 5.4.3 to discussions of the high (Oh ≫ 10), moderate (0.01 < Oh < 10) and low (Oh < 0.01) Ohnesorge number regimes, respectively.

5.4.1 High Oh

Experiments in the high Oh limit have been limited to non-Newtonian fluids (e.g. PDMS in [35], molten polystyrene in [32] and [99]). We proceed by demonstrating that the essential features of retraction including the exponential hole retraction are captured by a Newtonian fluid description.

Figure 5-5 illustrates the evolution of typical film profiles at various Oh and their corresponding velocities along the film midplane in time increments of $\delta t = 10\tau_{\text{vis}}$. As Oh increases beyond Oh > 100, the rim diffuses towards the bulk of the film, thus making the film appear to be of uniform thickness. However, as one would expect, the film is slightly thicker near the rim and very gradually thins further away from the tip. It is also important to note that the region of influence of the film is directly proportional Oh. This was also suggested by Brenner & Gueyffier [13], who identified the Stokes length $\mu/\rho u_c = \text{Oh}H$ as the characteristic lengthscale at high Oh. As time progresses, more fluid is set into motion and hence the region of influence due to tip motion grows in time.

Just as the velocity curves for a planar sheet asymptote to a single curve in the high Oh limit (see figure 4-4), something similar can be said for the circular sheet. However, the initial size of the nucleated hole has to be taken into account. In particular, having written the momentum equations in non-dimensional form as in (5.12b) and by assuming that the film profile near the tip is preserved, we can replace the derivative of the film curvature with the approximate expression

$$\kappa_{r^*}^* \approx 2\text{Oh}^2\delta\left(r - r_0^*\right) ,\tag{5.42}$$

provided that the azimuthal curvature term in (5.12c) is much smaller than the curvature of the film profile. Doing so leaves us with a set of dimensionless equations that do not depend on Oh. Therefore two different simulations will yield almost identical results provided that r_0^*, the dimensionless initial hole radius, is the same. In other words, curves that have the same ratio

$$C = \frac{R_0}{H\text{Oh}}\tag{5.43}$$

will yield virtually indistinguishable velocity curves, as confirmed by a number of simulations. For example, tip speeds of a simulation with Oh $= 10^4$ and $R_0 = 50H$ are
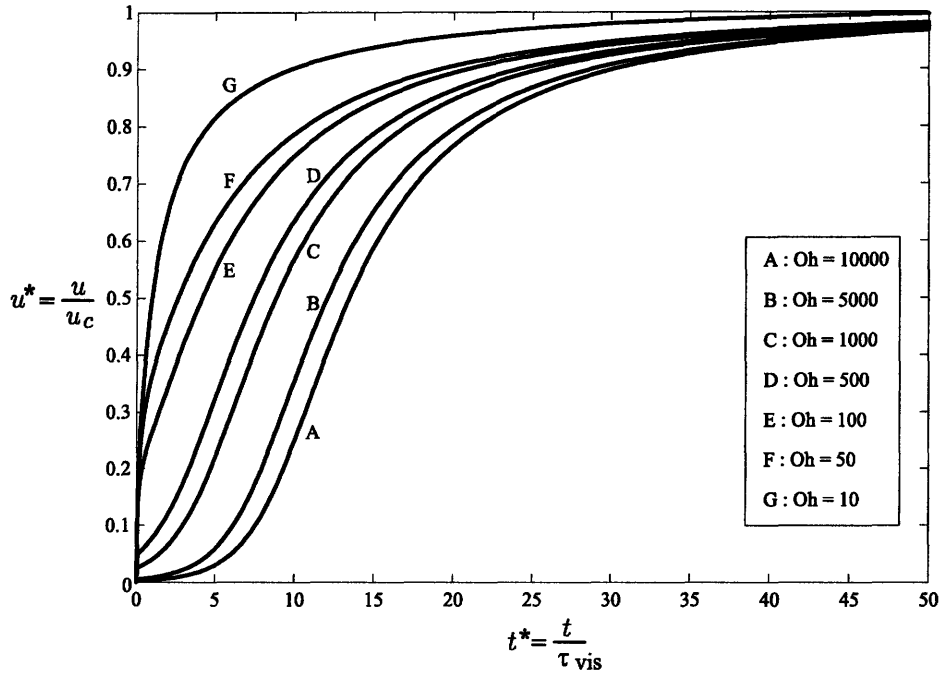
Figure 5-6: Speed at the film edge as a function of time for different values of Oh, with initial hole radius of $R_0 = 50H$. The higher the Oh, the slower the approach towards the Taylor-Culick speed, u_c.

indistinguishable from these with Oh $= 10^3$ and $R_0 = 5H$.

Figure 5-6 indicates the dependence on Oh of the approach of the sheet tip to the Taylor-Culick speed. Compared to the low Oh regime, high Oh films require substantially more time to approach u_c. Viscous resistive forces delay the acceleration process, because a larger amount of fluid needs to be accelerated by curvature forces concentrated near the film edge. In order to assess how Oh affects the acceleration phase, we plot in figure 5-7 the time required for the tip to attain 30%, 60% and 90% of the Taylor-Culick speed for different Oh. Each simulation was initialized with a hole radius of $R_0 = 50H$. As can be inferred from the theoretically predicted exponential law in equation (5.9), we find that the times $t_{1,2}$ needed for the tip to attain the speed of a certain fraction of u_c that correspond to $Oh_{1,2}$ satisfy the relation

$$\frac{t_1}{Oh_1} - \frac{t_2}{Oh_2} = 2\log\left(\frac{Oh_1}{Oh_2}\right) , \tag{5.44}$$

provided that $Oh_{1,2} \geq 100$. At lower Oh, there is a clear deviation from this relation, which

82
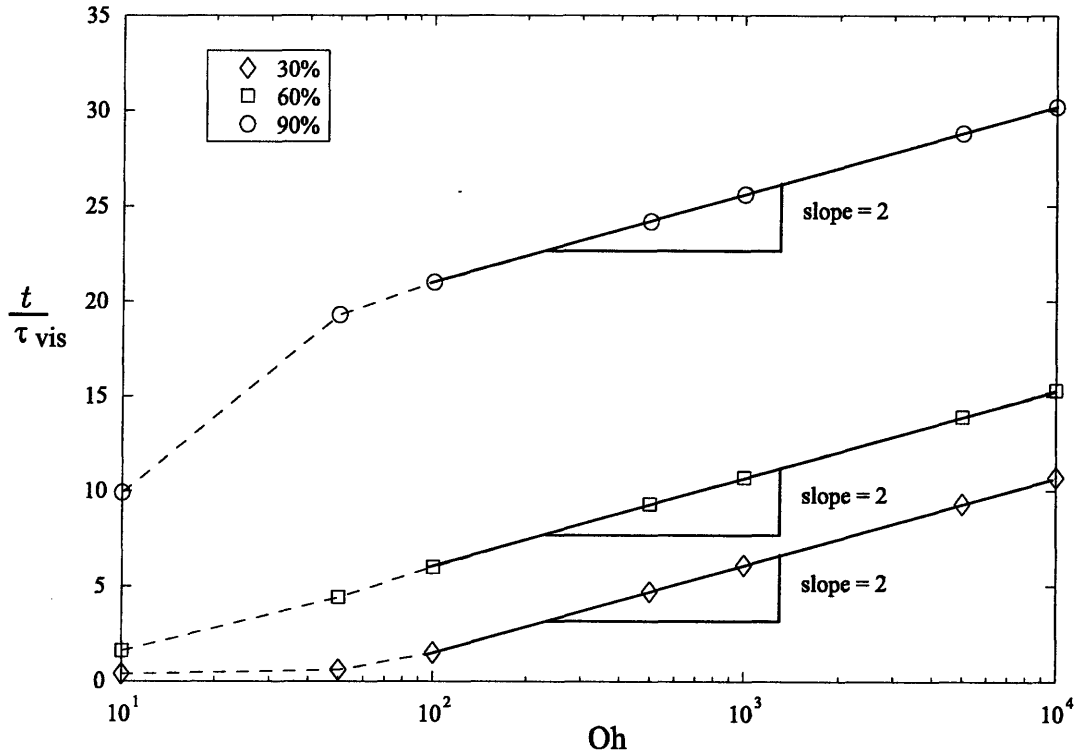
Figure 5-7: Time to reach 30%, 60% and 90% of the Taylor-Culick speed vs Oh for simulations with $R_0 = 50H$. For Oh $\geq$ 100, there is logarithmic dependence on the Ohnesorge number, confirming the theoretically predicted retraction rate, equation (5.9).

suggests that the rim acceleration is different from that predicted in the viscous limit. It is rather surprising that equation (5.44) extends beyond the range of validity of the exponential retraction.

In figure 5-8 we confirm the exponential retraction rate observed in the experiments ([35], [36], [32] and [99]) during the early stages of retraction. We note that the higher the Oh, the longer the hole grows according to the exponential law. Using additional information from figure 5-6, our simulations reveal that the deviation from the exponential behavior occurs quite early in the retraction process, typically when the rim speed is of the order of $0.2u_c$.

As we saw in §5.1, sheet rupture does not occur when the punctured hole is of radius less than the film thickness. We proceed by looking at the effect of the initial hole size on the retraction dynamics. Figure 5-9(a) shows the evolution of the hole radius for a number of different initial radii, when Oh $= 1000$. The calculations indicate that the smaller the
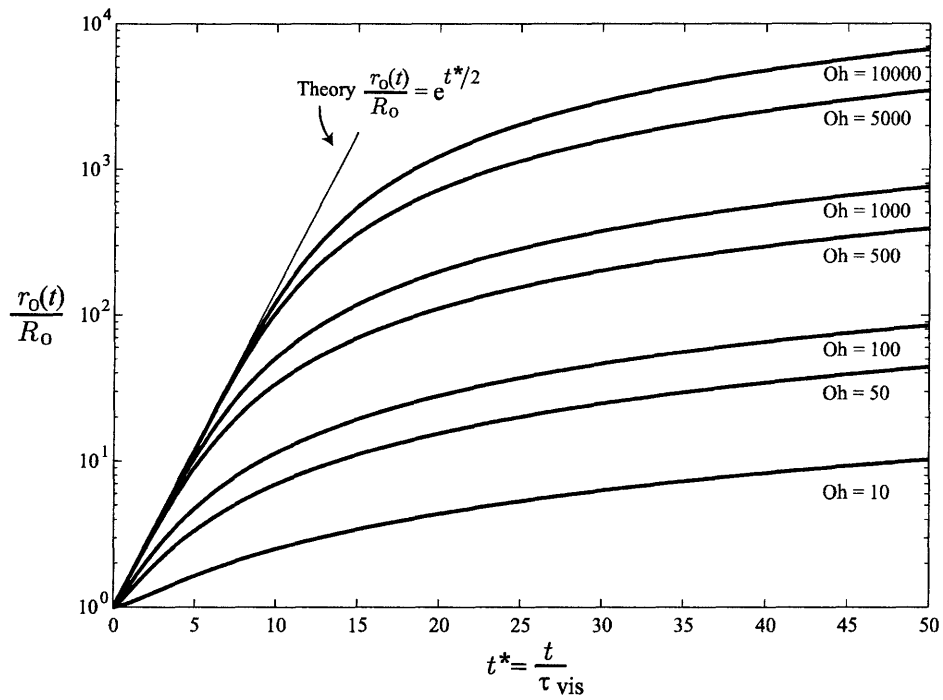
Figure 5-8: Hole growth vs time for different Oh, for an initial hole size $R_0 = 50H$. The higher the Oh, the longer the hole grows according to the exponential law, equation (5.9).
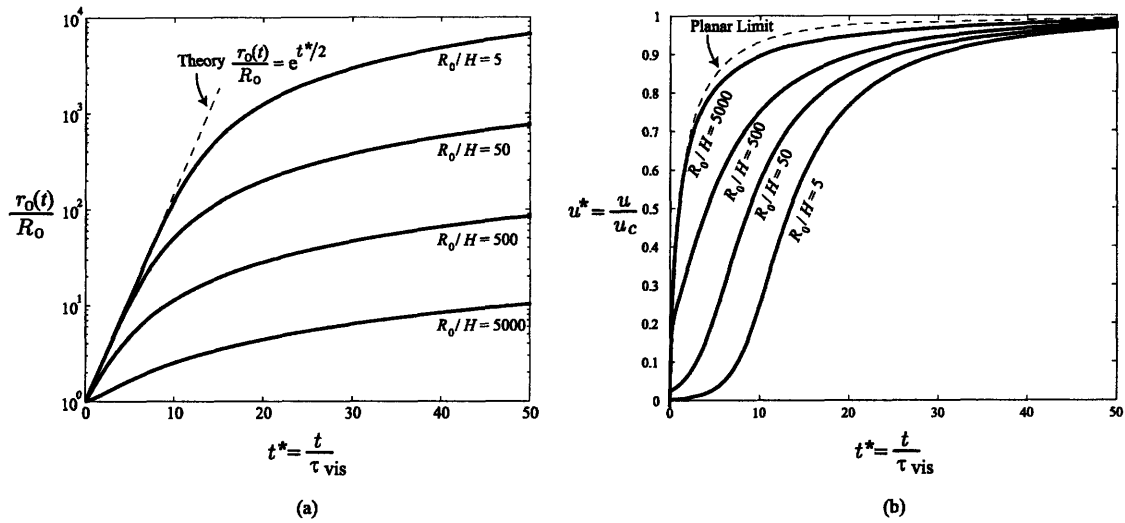
Figure 5-9: Variation of initial hole size for Oh = 1000: (a) Hole expansion vs time and (b) Approach to Taylor-Culick speed vs time. For small initial hole radii, the agreement with the theoretically predicted rate lasts for longer times. For larger initial radii, we approach the planar limit, considered in Chapter 4.

initial hole size, the longer the hole radius evolves according to the theoretically estimated exponential rate of expansion, equation (5.9). In other words, the circular geometry is influencing the dynamics for longer times when the initial hole radius is relatively small. However, when the hole radius is large, the film motion rapidly approaches the planar limit considered in Chapter 4. Evidently the variations in the initial hole radius affect the low Oh films to a lesser extent, mainly due to the shorter timescales involved. This can also be inferred from figure 5-9 and the criterion for similarity obtained in equation (5.43).

The discrepancy between the experimentally determined hole growth rate in the work of Debrégeas *et al.*, $1/1.4$ in equation (5.10), and the retraction rate predicted by theory, $1/2$ in equation (5.9), prompts us to look at the effect of the initial film profile during the initial stages of film rupture. If the needle the initiates the retraction is orders of magnitude thicker than the film, the film profile near the tip may not be semi-circular and a more pointed tip would be a more realistic initial shape. The film profile used, equation (5.13), facilitates this calculation as it can be conveniently modified via a single parameter, $\alpha > 0$. As $\alpha \to 0$, the tip approaches a circular cap; the curvature at the tip increases with α according to equation (B.9). In figure 5-10 we show the effect on the retraction rate as the initial film profile becomes more pointed near the tip. Sheets with more pointed

85
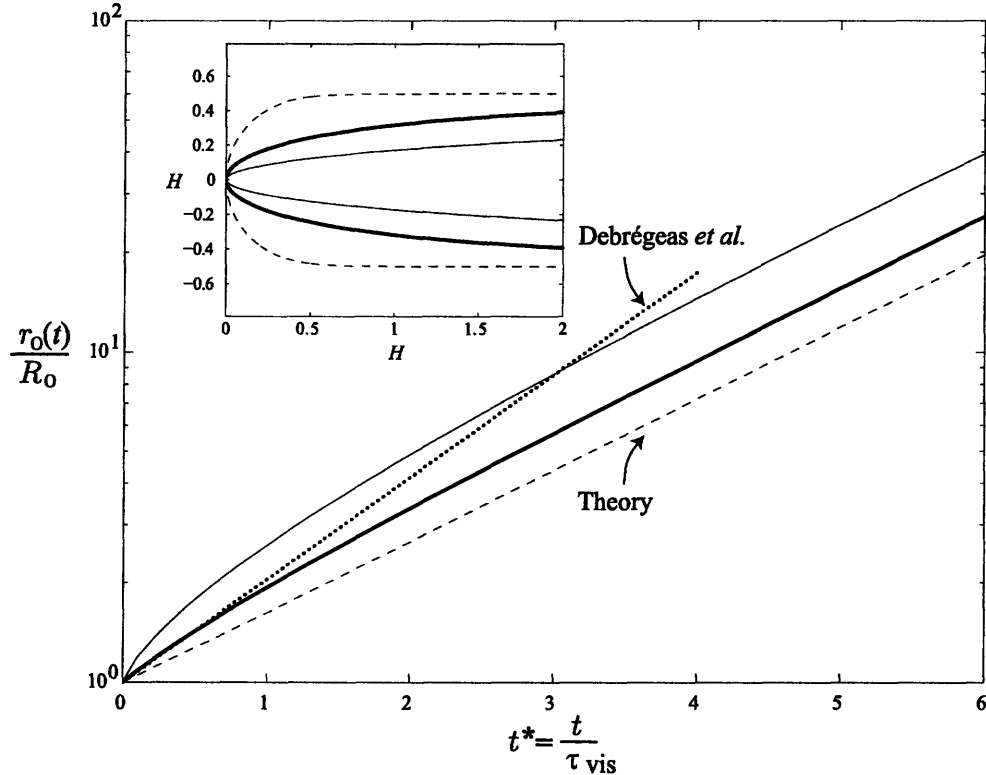
Figure 5-10: Effect of the initial film profile. Hole growth vs time for Oh $= 8\times10^3$ and $R_0 = 40$. The inset shows the corresponding initial film profiles at the vicinity of the tip. When using a more pointed initial film profile we obtain a faster rate of retraction until the pointed tip relaxes to a semi-circular cap, which then retracts according to the theoretically predicted rate, shown by the dashed curves.

tips initially retracted faster owing to the enhanced curvature force. Eventually as the rim acquires a more circular form, the retraction slows down to the rate predicted by theory. Whether the pointed initial profile is the source of the anomalously large retraction rate observed by Debrégeas et al. in [35] cannot be assessed due to uncertainty in the film shape and to the limited duration over which their data was collected. Nevertheless, the experiments of Roth et al. [99], suggest that an initially pointed profile can potentially explain the different retraction regimes they observe in experiments using polystyrene films that have a characteristic timescale $\tau_{vis} = \mathcal{O}\left(10^4 s\right)$. To account for these effects and analyze the collected data, they assumed an empirically deduced time-dependent viscosity that was fitted with the experimental data. However our calculation yields a behavior that is quite similar to their experimental observations, thus suggesting that the initial retraction rate
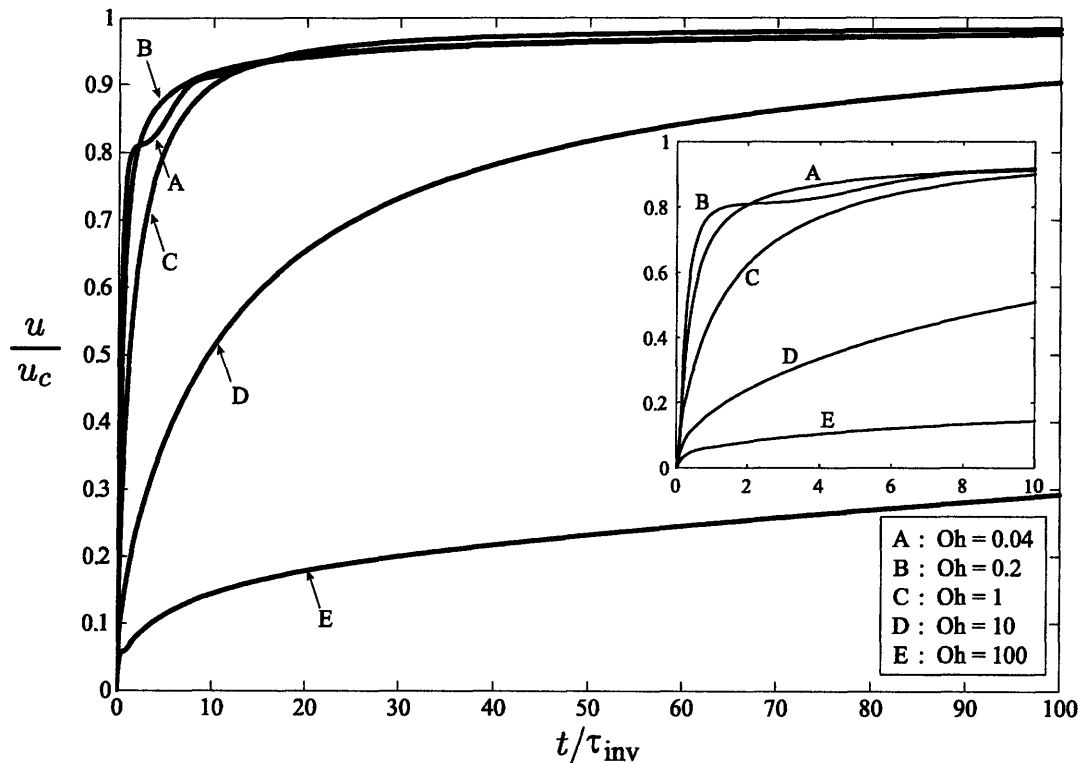
Figure 5-11: Speed of the film tip vs time since rupture for moderate Oh. Note the retraction of the Oh = 100 film that happens at a much slower time scale. Inset: early stages of retraction. When Oh = 0.04, there is a brief reduction in the rate at which the film approaches u_c, due to the production of capillary waves ahead of the rim.

they observe can be attributed to the initial puncture shape.

5.4.2 Moderate Oh

Moderate Oh films (0.01 < Oh < 10) arise in most configurations of practical importance, for example the bursting of soap films. Prior to fragmentation, a sheet is generally bounded by an edge that recedes and accumulates fluid [123]. In figure 5-11 we show the evolution of the tip velocity for different Oh, when the initial hole radius is $R_0 = 50H$. Not much can be typically said about the acceleration phase of the film edge because it happens extremely rapidly, on the order of microseconds. For comparison, we included the calculation for a high Oh film (Oh=100), that illustrates that the transition to u_c happens on a much slower timescale. It is also worth noting that in the Oh = 0.04 case, there is temporarily a slight reduction in the acceleration of the tip, because of the capillary waves that are being

87
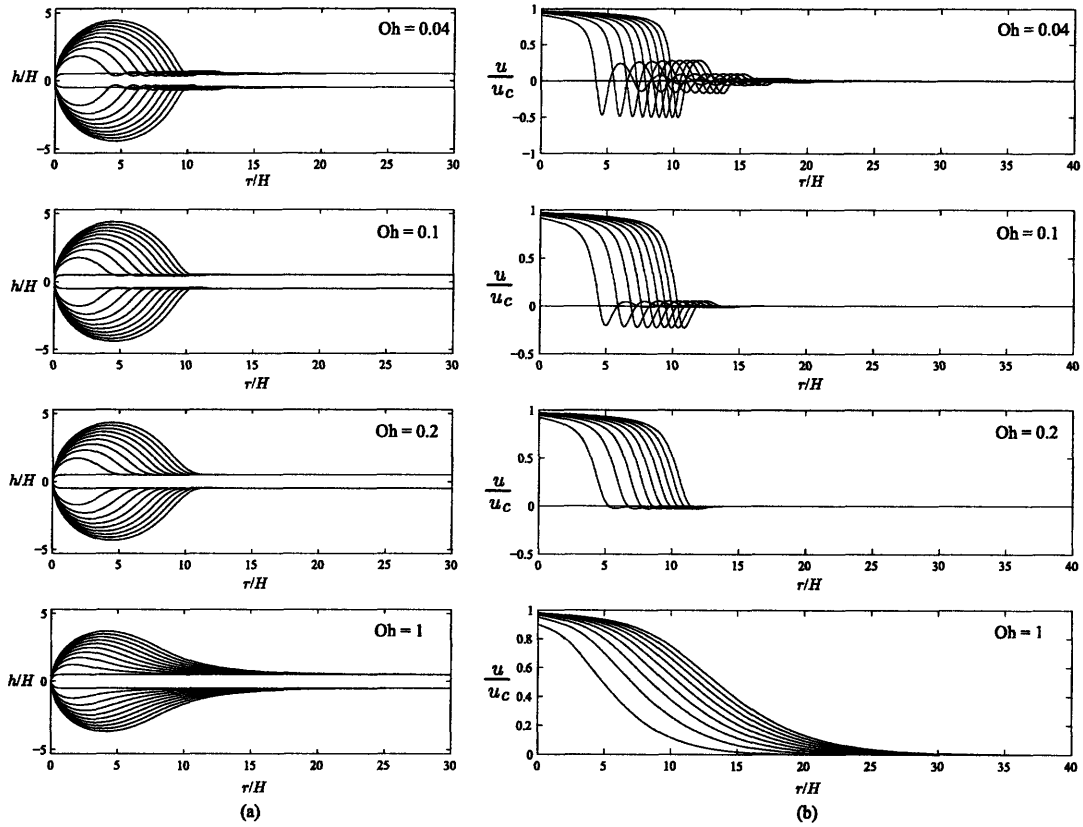
Figure 5-12: Evolution of the film boundaries and midplane velocities for moderate Oh in time increments of $\delta t = 10\ \tau_{\text{inv}}$, when the initial radius of the hole is $R_0 = 50H$. Note the generation of the capillary waves which are more pronounced for Oh $= 0.04$ and the associated oscillations in the midplane velocities. As Oh is increased, the capillary waves diminish and the previously pronounced rim begins to diffuse towards the bulk of the film.

generated ahead of the rim. These waves transfer momentum upstream of the advancing rim and the associated wave drag slows down the rim.

In figure 5-12 we show the evolution of typical film profiles and their corresponding radial velocities along the midplane of the film in time increments of $\delta t = 10\tau_{\text{inv}}$. It is evident from these figures that at low Oh, the motion is more localized in the vicinity of the edge. The curvature forces impart acceleration to the rim, which in turn collides with the quiescent fluid in the bulk of the film. The inertia of the fluid ahead of the edge is thus responsible for rim formation.

As is evident in figure 5-12, film retraction at Oh < 0.1 is accompanied by capillary waves that precede the rim. The work of Song & Tryggvason [108] provided some physical

insights regarding rim and capillary wave formation of planar sheets. In particular, via two-dimensional simulations, they argued that the curvature variations near the tip generate vorticity there that initiates the retraction of the edge. For high Oh films, this vorticity diffuses through the rest of the film and for that reason no rim forms.

While the study of vorticity in our one-dimensional model is not possible, we can gain some insights into the flow by constructing an approximation to the velocity field using the expansions obtained in § 5.3.3. Using the velocity u and film thickness h obtained from our simulations, we plot the velocity field (U, V) along the (r, z) directions in polar coordinates and the pressure along the midplane of the film using the set of equations (5.21). Even though the computation of u and h is second order accurate in δr and the computations for U and V involve the evaluation of higher derivatives of u, it is possible to capture the essential features of the flow.

Figure 5-13 shows plots of the velocity field in the film together with the pressure along the midplane for films in the three regimes of interest. In the high Oh regime, (c), the pressure field attains its maximum near the film tip and monotonically decreases towards the bulk. This pressure gradient essentially generates the flow that drives the retraction. As the Oh is decreased, (b), we see that the pressure is nearly constant in the rim and then drops in the vicinity of the rim tip. From the velocity field in the lab frame we notice a backflow towards the rim, thus contributing to its growth. For the low Oh film, at each successive neck there are pressure drops and we see circulating flow, confirming the local generation of vorticity.

A neck that connects the rim with the rest of the film only arises for Oh < 0.1, unlike the ubiquitous necking that arises in the capillary breakup of jets [93]. As Song & Tryggvason pointed out [108], the mechanisms involved in neck thinning and jet breakup are qualitatively different. The pinch-off that leads to jet breakup is induced by perturbations to the jet boundaries, which increase the pressure near depressions of the jet boundaries, thus driving fluid away from them. In a low Oh film however, the pressure attains a local *minimum* at the neck. The clockwise circulation that is evident in the upper part of the film near the neck in figure 5-13(a), tends to push fluid into the rim and out of the neck, thus contributing to the gradual neck thinning. While we suspect that the Oh = 0.04 film depicted in figure 5-12 will pinch-off eventually, the computational cost of such a protracted simulation can be quite large, especially if a high accuracy calculation is desired.
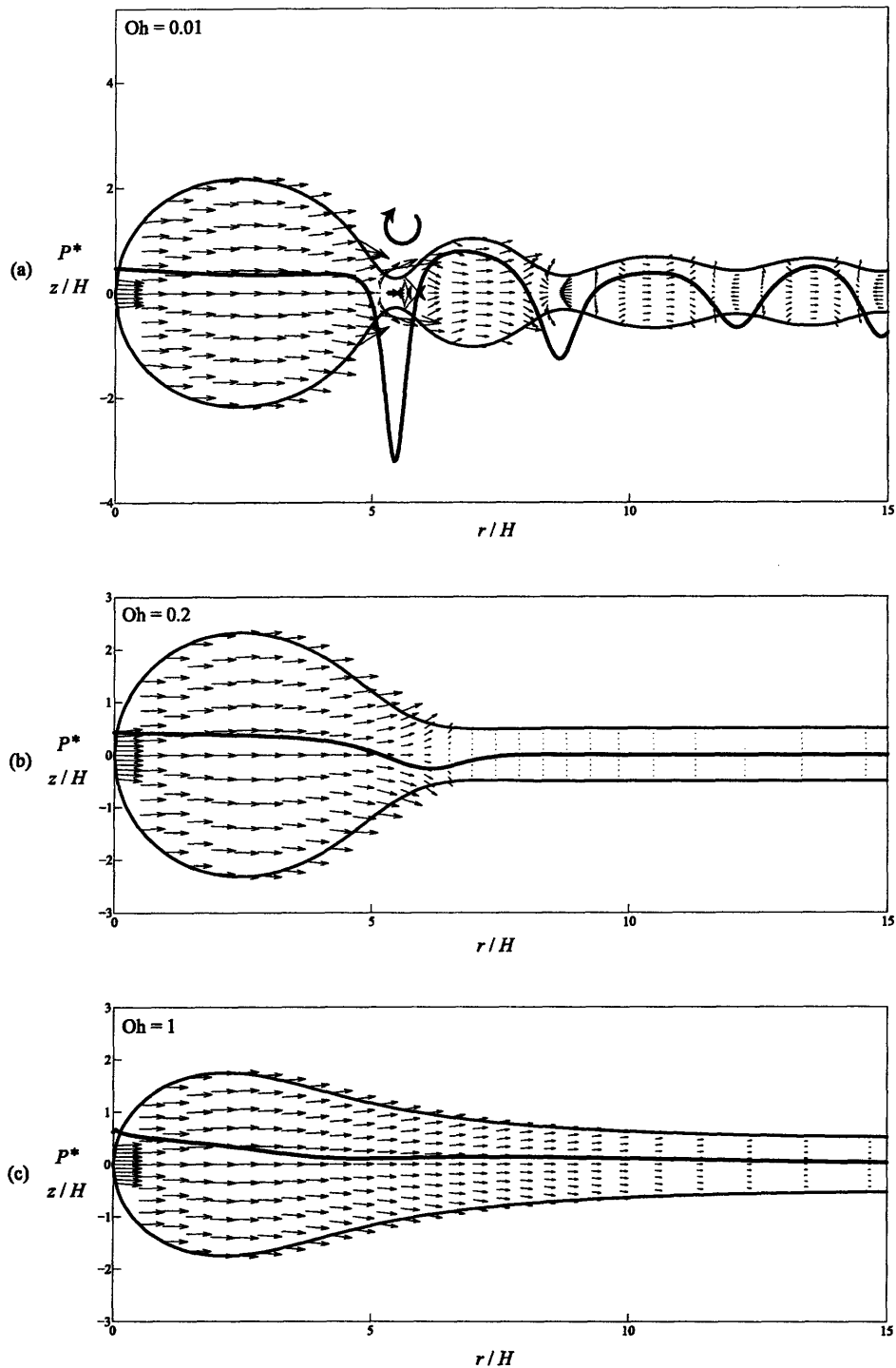
Figure 5-13: Velocity field and midplane pressure for different Oh. The vector field is depicted by the arrows and the curve corresponds to the dimensionless pressure $P^* = Hp/\gamma$ along the film midplane. For the low Oh in (a) vorticity generates capillary waves that are connected to the rim via a neck region. As Oh increases, the waves diminish and the rim begins to diffuse towards the bulk of the film for Oh $= 1$, (c). Note also the pressure drops near neck regions.
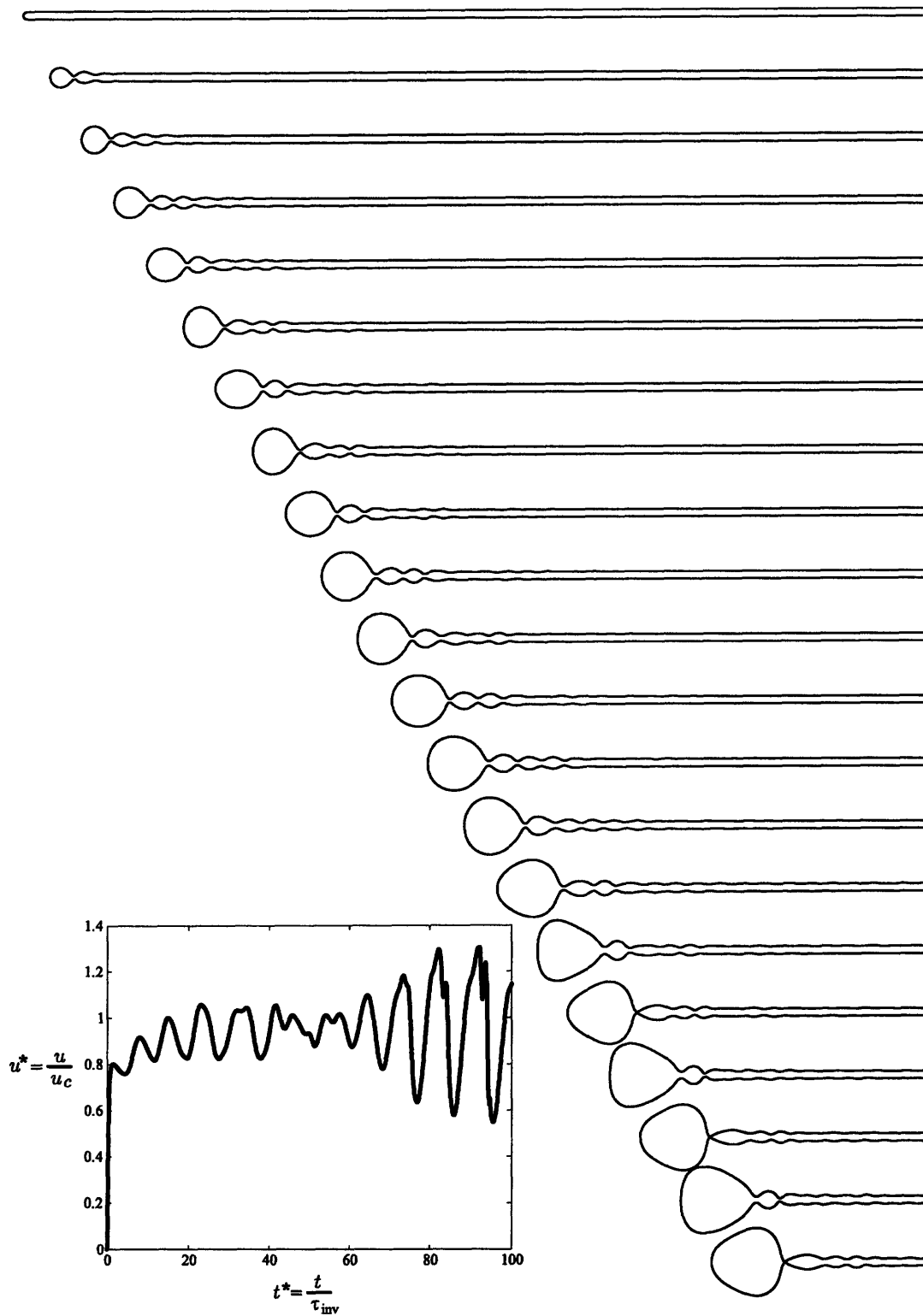
Figure 5-14: Sequence of the film profiles for Oh = 0.01 in time increments of $\delta t = 5t_{\mathrm{inv}}$; inset: tip speed vs time. The capillary waves are more pronounced and begin to interact with the rim after an initial transient. This interaction becomes more violent as time progresses and eventually causes breakup. Inset: the evolution of the tip speed resulting from the rim-wave interation.

91
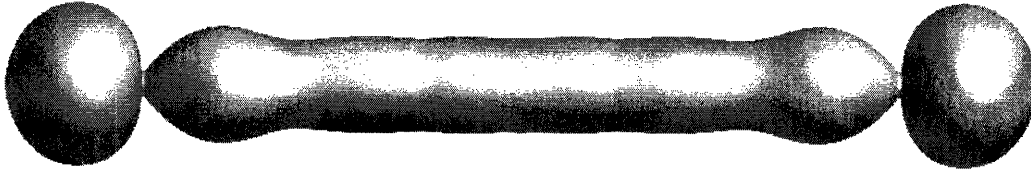
Figure 5-15: A contracting filament at Oh = 0.001 can exhibit similar breakup characteristics with a retracting sheet (reproduced from simulations of Notz & Basaran [80]).

5.4.3 Low Oh regime

The situation is markedly different for Oh < 0.04. A simulation was run for Oh = 0.01, frames of which are shown in figure 5-14. As expected, the capillary waves generated are of higher amplitude than the Oh = 0.04 case. When these waves grow sufficiently in amplitude, they begin to interact with the growing rim. As time progresses, this interaction becomes more violent, causing the thickness of the neck near the rim to oscillate towards zero. At $t = 100\tau_{inv}$, when the simulation was terminated, the film was on the verge of pinch off as the film thickness was approaching zero.

The inset of 5-14 shows the evolution of the tip speed, which oscillates with an amplitude that increases over time, as the rim interacts with the waves it generates. This can be compared with the Oh = 0.04 film in figure 5-11, where the tip almost monotonically increases to u_c, apart from a short interval during which the train of waves is generated. Thus the waves in the Oh = 0.04 case do not grow substantially over the interval of the computation, contrary to the Oh = 0.01 case.

An indication exists in the work of Song & Tryggvason [108], that this wave-rim interaction can occur for Oh $= \mathcal{O}(0.01)$; however their two-dimensional simulations were not carried out long enough to see whether it becomes more violent at later times. Such growing amplitude oscillations of the tip speed were also observed at the edge of a contracting filament in simulations by Notz & Basaran [80] (figure 5-15). Depending on the Ohnesorge number, there were cases where the filament profiles they obtained, were not single-valued functions of r near pinch-off. However, our lubrication approximation presumes a single valued film profile and this has to be borne in mind, as it possible that the rim might have pinched-off at some earlier time.

Simulations at even lower Oh (Oh = 0.005) revealed that sheet breakup can happen

almost as soon as retraction is initiated. We note that such low Oh are not readily achieved in a laboratory setting, since in order to probe into this regime, a water sheet needs to be about 0.5mm thick, a few orders of magnitude thicker than a typical soap film.

5.5 Three-dimensional and other considerations

The model we considered here neglects any three-dimensional effects; specifically we have neglected the azimuthal variations in rim radius that are expected to rise via capillary instability of which there is ample experimental evidence (e.g. [77], [82]). Rim instabilities also occur in the so-called Edgerton crows, formed by the rim of a tubular film that is ejected after the impingement of a drop on a thin layer of fluid (e.g. [130], [127]).

While the rim instability is also commonly attributed to the Rayleigh-Plateau instability, if we look at the relevant timescales, we see that the instability is more complex here due to the fact that the rim grows in time. For instance in the moderate Oh regime, if a rim of radius R were to pinch off due to the capillary instability, it would do so after a time

$$\tau_c \sim \sqrt{\frac{\rho R^3}{2\gamma}} \, , \qquad (5.45)$$

which can be comparable to the low Oh timescale of retraction,

$$\tau_{\text{inv}} = \sqrt{\frac{\rho H^3}{2\gamma}}. \qquad (5.46)$$

This is especially true at the onset of retraction, where H and R are comparable. However, experiments in [77] have shown that rim instability is delayed by the rim growth, which makes τ_c larger. The tendency of the rim growth to suppress the onset of this instability was demonstrated in the numerical simulations of Fullana & Zaleski [48], who suggested that the rim will eventually become unstable to perturbations of wavelength that are typically a few orders of magnitude longer than the film thickness. Despite the fact that the understanding of this mechanism will contribute to our ability to predict drop sizes resulting from film disintegration [123], it is a problem that has not been addressed at a fundamental level yet. Apart from the suppression of the capillary instability due to the rim growth, the stability of the rim is further enhanced through the action of viscosity as was confirmed in the experiments using highly viscous fluids ([35], [32], [99]).

Chapter 6

Concluding remarks

6.1 Summary

In this thesis, we have presented the formulation of the governing equations of Newtonian thin film flows. In Chapter 2, we presented a formal fluid mechanical treatment of the Navier Stokes equations on an arbitrarily curved surface, drawing upon various concepts from differential geometry and tensor calculus. Particular attention was given to incorporating the inertial effects and the surface tension contributions that arise from the variations in the film thickness, measured relative to a center surface that prescribes the coordinate system. The equations obtained in the end, albeit complicated, are essential for simulating thin film flows of arbitrary geometries, where the exact resolution of the free boundaries is desired.

In Chapter 3, we considered simpler geometries that can be parametrized by a curvilinear coordinate system. Under the assumption that longitudinal fluid motions dominate the transverse ones, we performed a perturbation expansion in powers of a small parameter corresponding to the ratio of the characteristic thickness to longitudinal length scales to obtain the leading order equations. Doing so reduces the dimensionality of the problem by one, which is of great advantage for numerical simulations. Several previous studies performed on fluid jets employed similar approaches that compared well with experimental observations, despite the fact that the lubrication assumption (that the slope of the free surface is much smaller than unity), strictly fails near neck regions or at the jet tip [43]. These issues also arise in our thin film flow models, but were ameliorated by including the curvature effects due to rapid variations in film thickness and using the appropriately modified condition at the film edge. In the special case of an axisymmetric geometry,

the equations were further reduced to obtain a system of time-dependent, one-dimensional partial differential equations. These equations are essentially a generalization of the models used for example by Taylor [112] and Bark *et al.* [5] to study the steady axisymmetric sheets obtained when a jet hits an impactor; our model is appropriate for unsteady motions and includes the effects of viscosity.

In Chapter 4, we turned our attention to the simplest physical system that may be examined with this formalism; the bursting of planar films. We clarified the shortcoming of Dupré's attempt to use an energy principle to obtain the retraction speed, by properly manipulating the lubrication equations. We found that viscous forces do not contribute to the total momentum of the film; consequently our formulation yielded the same result as that of Taylor [114] and Culick [31], who deduced the correct speed on the basis of an inviscid theory. As we have seen, viscosity essentially dictates how momentum is distributed throughout the film. A measure of the effect of viscosity is quantified through the Ohnesorge number, $Oh = \mu/\sqrt{2\rho\gamma H}$. In the low Oh regime, the retraction is inertia-dominated and we get capillary wave formation ahead of a growing rim. For moderate Oh numbers, no capillary waves form ahead of the rim and for the high Oh films, the retraction is dominated by viscosity and no rim forms. Brenner & Gueyffier [13] were the first to identify these regimes. We extended their work on retraction in this geometry, by predicting analytically the dynamics in the high Oh regime at the onset of rupture. In particular, we found that the edge of the film recedes a distance that grows according to $(t/\tau)^{3/2}$, where τ is the characteristic timescale. Additionally, we determined analytically that the tip curvature grows linearly in time, contrary to the low Oh regime which has a square root dependence.

In Chapter 5, we developed a theoretical model that allows us to investigate the retraction dynamics of a circular sheet and made comparisons of our model with the experimental investigations of Debrégeas *et al.* [35], Dalnoki *et al.* and Roth *et al.* [99]. Our results confirmed the conjecture of Brenner & Gueyffier that geometry is important in sheet retraction especially in the high Oh regime. During the initial stages of retraction, the circular hole punctured on a sheet expands according to $e^{t/2\tau}$, while the planar sheet recedes according to the power law obtained. This difference is associated with the azimuthal curvature that opposes the initial expansion of the circular hole and the viscous stresses that are relatively large when the punctured hole is small. In the long-time limit however, after which the circular hole has grown substantially, these effects are diminished and the governing equations
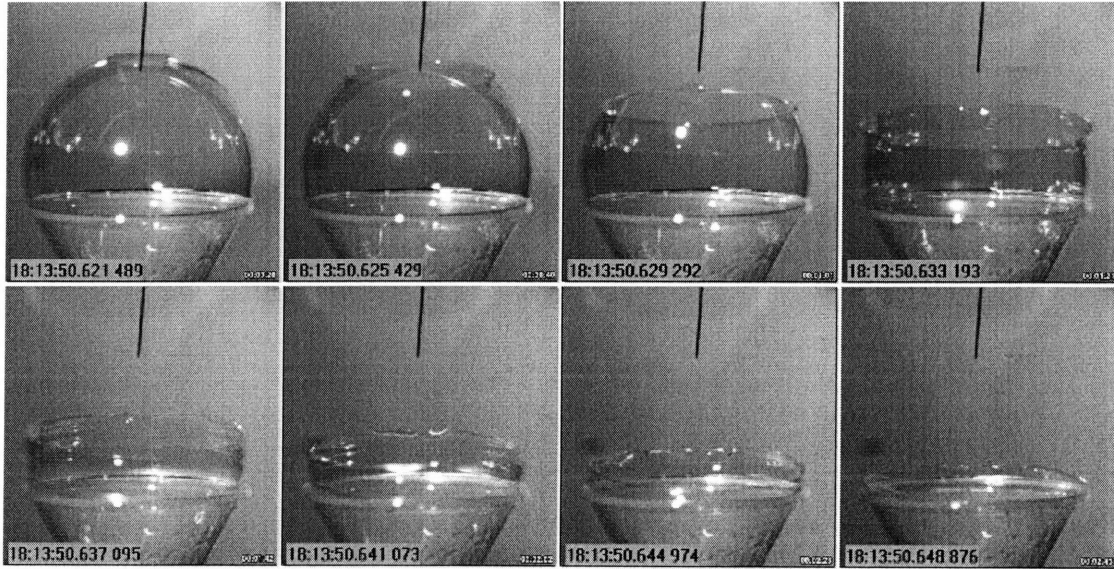
Figure 6-1: Frames taken from the bursting of a viscous bubble. The centripetal force due to the curvature of the bubble deforms the initially spherical shape of the bubble as time progresses.

asymptote to those arising in the planar geometry. The discrepancy between the predicted and observed retraction rates, may be attributed in part to the details of the puncture through the initial film profile. In particular, we found that the initial retraction rate could be made faster with a slightly pointed initial film profile, but as time progresses, the retraction rate approaches that of a film with a nearly semi-circular initial profile. Similar observations were made by Roth *et al.* [99], with his experiments on polystyrene films, but were not attributed to the profile of the film. It is hoped that our findings might motivate and inform further experiments on the early stages of film retraction.

6.2   Discussion and future work

Even the general approach adopted has its limitations. For example, there are cases where the transverse motions are appreciable, so our perturbation expansion cannot be meaningfully applied. Nevertheless, these models may serve as a foundation stone upon which to build more complex models that include, for example, surface tension gradients and the ambient fluid effects.

As a natural extension to the retraction problems considered in Chapters 4 and 5, we

can use the unsteady axisymmetric thin film equations derived in Chapter 3 to study the retraction of a curved film. Experimental work on bubble retraction that covered a rather broad range of fluid viscosities was performed in the past by Debrégeas et al. [36] and also by Pandit & Davidson [82]. Apart from direct comparisons with experiments, the ultimate goal of such a study would be to gain more insight into spray formation via bubble bursting, as arises, for example, when air bubbles burst at the sea surface of the sea [8]. The novel feature brought about by this process is the fact that the curved geometry introduces additional centripetal forces, that are absent in flat geometries. These, in addition to the unbalanced capillary forces at the edge, cause the retraction process to be accompanied by the formation of ligaments that eventually disintegrate into small drops via capillary instability [88].

Our theoretical framework might also be applied in modeling bubble production, a problem with many applications in the food and chemical industries [109] and other industrial processes [67]. The study of the stability of gas-core annular jets, which eventually break to yield spherical shells, goes back to the early linear analyses of Rayleigh [93] and Chandrasekhar [20]. Experiments by Kendall [68] showed that under certain flow conditions, periodic oscillations occur downstream that eventually cause the encapsulation and sealing of the gas core into shells. These forms eventually detach from the jet and then rapidly evolve into shells with a high degree of periodicity and spherical symmetry. More recently, Gordillo et al. [52] and Lorenceau et al. [75] utilized a similar mechanism to produce micro-bubbles in a liquid suspension and Utada et al. [120] proposed a novel technique to produce emulsions of drops that encapsulate droplets of another immiscible fluid. By employing a variant of the unsteady axisymmetric models derived in Chapter 3, we can study the formation and stability of such forms under perturbations. It would be interesting to rationalize Kendall's experimental observations, by predicting the size and formation time of these bubbles.

On a more fundamental level, thin film models can be used to study the stability of the receding edge of a film. The destabilization of the rim of a fluid sheet is found in many contexts such as in the celebrated Worthington-Edgerton crowns [127], that occur when a droplet impacts a thin film of fluid, in sheet retraction (McEntee & Mysels [77], Queré & Reyssat [91]) or at the edge of the sheet formed by the oblique collision of jets (Bush & Hasha [17], Bremond & Villermaux [12]). Small perturbations induced either artificially

or due to unavoidable irregularities in source conditions may cause the rim to deform into cusped shapes from which ligaments are emitted, which then break into droplets. While the breakup characteristics are reminiscent of the classical Rayleigh-Plateau instability of jets [93], to date the understanding of this fundamental phenomenon is not yet complete. Despite the wealth of theoretical and experimental attempts (Yarin [130], Villermaux and Clanet [122]) and simulations (e.g. Rieber and Frohn [98] Fullana & Zaleski [48]) on the subject, there is no compelling answer that elucidates the precise mechanism responsible for the cusp formation. Studying the stability of the rim goes a step beyond the subject of this thesis; the inclusion of three-dimensional effects makes the problem all the more challenging.

It is hoped that through the formalism developed herein, a number of fundamental problems in thin film flows can be addressed in the future. Simulation of the full Navier Stokes equations is currently impractical for this class of problems, given that the resolution of some of the fine features in thin film flows would require a dense mesh in the vicinity of the film. As our calculations on the dynamics of retracting films demonstrate, the simpler lubrication models employed here are able to capture the essential dynamics and yield results that compare favorably with both experimental observations and simulations of the two dimensional momentum equations. This success adds to our confidence that such models may be applied to tackle more complex problems.

Appendix A

Numerical solution

A.1 Iteration scheme

In this appendix we present the method employed to solve the system of equations (5.41) for the sheet retraction problem. To simplify the notation, the system of equations is recast in the form

$$\mathbf{G}(\mathbf{x}) = 0 \, , \tag{A.1}$$

where $\mathbf{G}$ and $\mathbf{x}$ are vectors. In solving this system of equations at each *timestep*, Newton's method is used. Starting from an initial guess $\mathbf{x}_0$, we solve equation

$$\mathbf{J}(\mathbf{x}_k) \, \Delta\mathbf{x}_k = -\mathbf{G}(\mathbf{x}_k) \tag{A.2}$$

for $\Delta\mathbf{x}_k$ at each iteration, where $\mathbf{J}(\mathbf{x})$ corresponds to the $N \times N$ Jacobian matrix of the system. The updated solution is

$$\mathbf{x}_{k+1} = \mathbf{x}_k + \Delta\mathbf{x}_k \, . \tag{A.3}$$

The iteration is continued until

$$\|\mathbf{G}(\mathbf{x}_{k+1})\| < \varepsilon \tag{A.4}$$

for some $\varepsilon > 0$ small, typically close to machine precision. The solution of $(A.2)$ requires a matrix inversion and it is the most time consuming part of the computation, especially if we use a fine spatial discretization. To overcome the difficulty of matrix inversion, $(A.2)$ is

solved iteratively using the generalized conjugate residual method, which can be found for example in [50]. At each iteration i, this method essentially solves the least squares problem

$$\min \left\| \mathbf{J}\left(\mathbf{x}_k\right) \ \Delta\mathbf{x}_k^{(i)} + \mathbf{G}\left(\mathbf{x}_k\right) \right\| . \tag{A.5}$$

In the absence of roundoff error, the exact solution is found in at most N iterations. The algorithm used by this method is outlined below:

1. Choose $\Delta\mathbf{x}_k^{(0)}$

2. Compute $\mathbf{r}_0 = \mathbf{J}\ \Delta\mathbf{x}_k^{(0)} + \mathbf{G}\left(\mathbf{x}_k\right)$

3. Set $\mathbf{p}_0 = \mathbf{r}_0$

4. For $i = 0$ until convergence compute the following
$$a_i = \frac{\mathbf{p}_i \cdot \mathbf{J}\ \mathbf{p}_i}{\|\mathbf{J}\mathbf{p}_i\|^2}$$
$$\mathbf{r}_{i+1} = \mathbf{r}_i - a_i \mathbf{J}\ \mathbf{p}_i$$
$$b_j^{(i)} = -\frac{\mathbf{J}\ \mathbf{r}_{i+1} \cdot \mathbf{J}\ \mathbf{p}_j}{\|\mathbf{J}\ \mathbf{p}_j\|^2}, \quad j \le i.$$
$$\mathbf{p}_{i+1} = \mathbf{r}_{i+1} + \sum_{j=0}^{i} b_j^{(i)} \mathbf{p}_j$$
$$\Delta\mathbf{x}_k^{(i+1)} = \Delta\mathbf{x}_k^{(i)} + a_i \mathbf{p}_i$$

The choice of a_i above minimizes the norm of the residual

$$\|\mathbf{r}_{i+1}\| = \left\| \mathbf{J}\left(\Delta\mathbf{x}_k^{(i)} + a\mathbf{p}_i\right) + \mathbf{G}\left(\mathbf{x}_k\right) \right\| \tag{A.6}$$

as a function of a, so the norm decreases at subsequent iterations. The generalized conjugate residual method involves computations with the Jacobian matrix, $\mathbf{J}$. This can be computed for example by a hand-written analytic formula or via the finite difference scheme

$$J_{ij}\left(\mathbf{x}\right) = \frac{G_i\left(\mathbf{x} + h\mathbf{e}_j\right) - G_i\left(\mathbf{x}\right)}{h}. \tag{A.7}$$

However the algorithm outlined above involves only Jacobian-vector products which are computed using:

$$\mathbf{J}\ \mathbf{v} = \frac{\mathbf{G}\left(\mathbf{x} + h\mathbf{v}\right) - \mathbf{G}\left(x\right)}{h}. \tag{A.8}$$

for some properly chosen $h > 0$ (see [19] and [69]). This Jacobian-free approach is the most advantageous since no costs of forming or storing the actual Jacobian are involved.
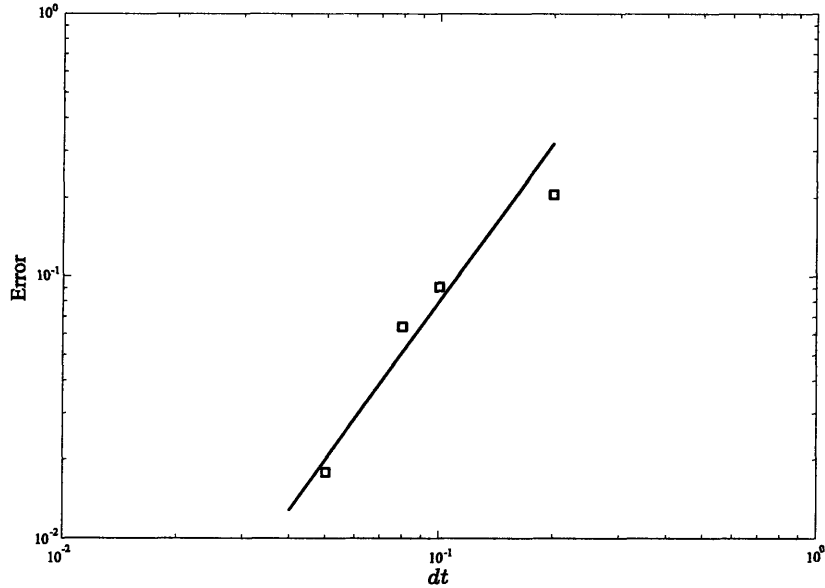
Figure A-1: Plot of the Error vs δx to illustrate second order convergence. When $\delta x = 0.2$ the errors are quite large due to the intial peak in the curvature gradient around $x = 0.5$.

Moreover, numerical tests showed that the convergence was quite fast compared to other methods for solving equation ($A.2$) and hence there is no need for preconditioning. At each timestep, the Newton iteration is initialized by extrapolation. For example, for a fixed time-step δt, we use

$$\mathbf{x}_0^{t+\delta t} = 2\mathbf{x}^t - \mathbf{x}^{t-\delta t}, \tag{A.9}$$

where $\mathbf{x}^t$ and $\mathbf{x}^{t-1}$ correspond to the converged solutions at times t and $t - \delta t$ respectively.

This is the essential basis of the matrix-free Newton-Krylov method employed to solve the system of equations. An overview of Jacobian-free methods can be found in the paper by Knoll and Keyes, [69] and further details can be found in the books by Kelley ([65] and [66]).

A.2   Convergence tests

The quadratic convergence of the Newton iteration was confirmed by a series of tests. To test the accuracy of the finite difference scheme employed we fixed the Ohnesorge number to Oh=0.2, the domain length to $L = 40$ times and integrated the equations until $T_f = 30$. Computations were performed to verify both spatial and temporal convergence.

101
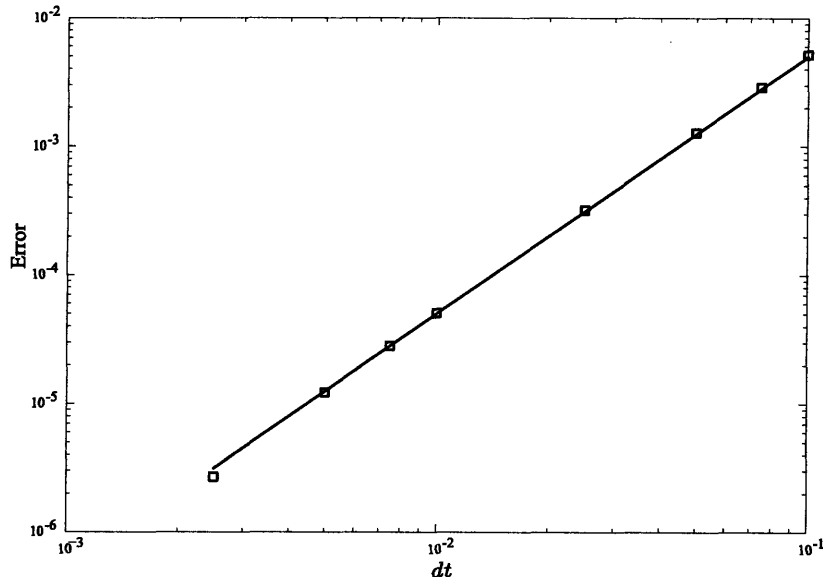
Figure A-2: Plot of the Error versus δt to illustrate the second order temporal discretization.

The equations used are obviously singular and blow up as δx, the spatial discretization of the domain, goes to zero; this is a shortcoming of the lubrication approximation, which assumes slow variations in the thickness of the film. However the fact that such models were used in the past and gave results that compared well with experimental observations, adds to our confidence in these models. For this reason, the grids were discretized for $\delta x = 0.04, 0.05, 0.08, 0.1, 0.2$, avoiding the use of finer grids which would get closer to the tip. On the other hand, the use of a grid coarser than $\delta x = 0.2$ would yield poor results, since we initially have an abrupt peak in the curvature gradient around $x = 0.5$. Figure A-1 confirms that even under these restrictions imposed on δx, we roughly get quadratic convergence for our scheme.

As mentioned in section 5.3.4, we use a θ-weighted scheme for the temporal discretization of the equations. When $\theta = 0.5$ (corresponding to the Crank Nicholson scheme), we are guaranteed quadratic convergence for linear PDEs. In our case the equations are highly nonlinear so we needed to verify this quadratic convergence. In our computations, we took θ slightly larger than $\theta = 0.5$, which gave better behaved solutions, without compromising accuracy, especially near the film breakup (Eggers & Dupont [43]). The quadratic convergence is confirmed in figure A-2 for various values of δt ranging from 10^{-3} to 10^{-1}.

One striking feature of the Newton iteration scheme that was observed during the tem-
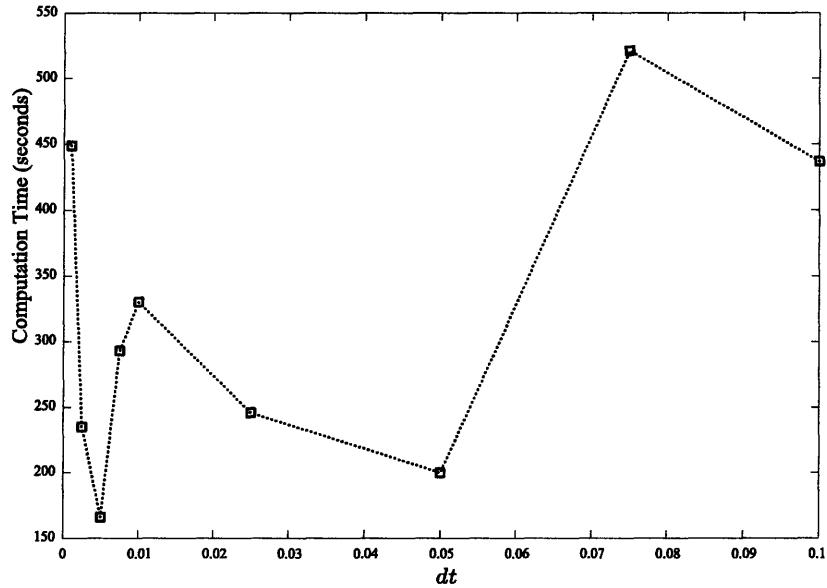
Figure A-3: Computation time vs time step δt. The computation time is minimized when $\delta t = 5 \times 10^{-3}$.

poral convergence analysis is that computational cost did not monotonically increase with decreasing time step. It was found that smaller time steps would sometimes perform faster than larger ones. This can be ascribed to the way the Newton iteration is initialized; the larger the time-step, the farther away the extrapolated initial guess in $(A.9)$ is from the converged solution. In figure A-3, we plot the computation time versus the timestep, δt. Of course there is ultimately a trade-off between taking more time-steps versus performing more iterations. Our results indicate that $\delta t \approx 5 \times 10^{-3}$ is the optimal timestep that achieves best accuracy and fastest overall performance.

Appendix B

Initial film profile for the sheet retraction problem

Since it is impossible to determine the exact initial profile of the film following its rupture, it is imposed rather artificially. We thus assume that the sheet consists of a semicircular cap together with a nearly straight strip of constant thickness 1 (in non-dimensional units). If we naively apply such a condition we encounter discontinuities in curvature because we have a jump from a curvature -2 to a zero curvature (see figure B-1). We thus need to construct a function $\eta(x) = \frac{1}{2}h(x)$ that mimics this initial condition, i.e.

$$\eta(x) = \tfrac{1}{2}\sqrt{1 - y(x)^2} \, , \tag{B.1}$$
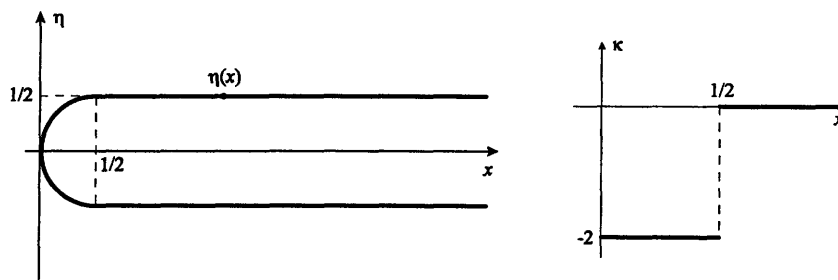
Figure B-1: Choosing a semi-spherical cap together with a straight strip introduces a jump discontinuity in the curvature.

where

$$y\left(x\right) = \begin{cases} -2\left(x - \frac{1}{2}\right) & 0 \leq x \leq 1/2 \\ 0 & x \geq 1/2 \end{cases} . \tag{B.2}$$

The last equation resembles the classical phase plane flows arising in dynamical systems that are known to exhibit stable and unstable orbits [110]. We can reproduce a smooth approximation to $y\left(x\right)$, if we borrow some ideas from this branch of mathematics. A simple dynamical system that has stable and unstable orbits along $y = -2x$ and $y = 0$ is:

$$\dot{x} = x + y , \tag{B.3}$$

$$\dot{y} = -y . \tag{B.4}$$

If we look at the phase plane, the solutions to this system of ODEs follow curves given by

$$xy = -\tfrac{1}{2}y^2 + \alpha, \text{ for } \alpha > 0.$$

When $\alpha = 0$, we find that $y = 0$ and $y = -2x$. In order to give a smooth representation for $y\left(x\right)$, we shift these curves to the right by some distance λ; hence

$$\left(x + \lambda\right)y = -\tfrac{1}{2}y^2 + \alpha . \tag{B.5}$$

Since $y\left(0\right) = 1$, we find that

$$\lambda = \alpha - 1/2 . \tag{B.6}$$

Solving for $y\left(x;\alpha\right)$ gives

$$y\left(x;\alpha\right) = \frac{1}{2} - \alpha - x + \frac{1}{2}\sqrt{\left(1 + 2\alpha\right)^2 + 4x\left(x + 2\alpha - 1\right)} . \tag{B.7}$$

Therefore the initial film profile takes the form

$$\eta\left(x;\alpha\right) = \tfrac{1}{2}\sqrt{1 - y\left(x;\alpha\right)^2} . \tag{B.8}$$

In the limit $\alpha \to 0$, we retain the piecewise $y\left(x\right)$. The smaller we take α, the more pronounced the peak in the curvature gradient, and the finer the mesh required to resolve the
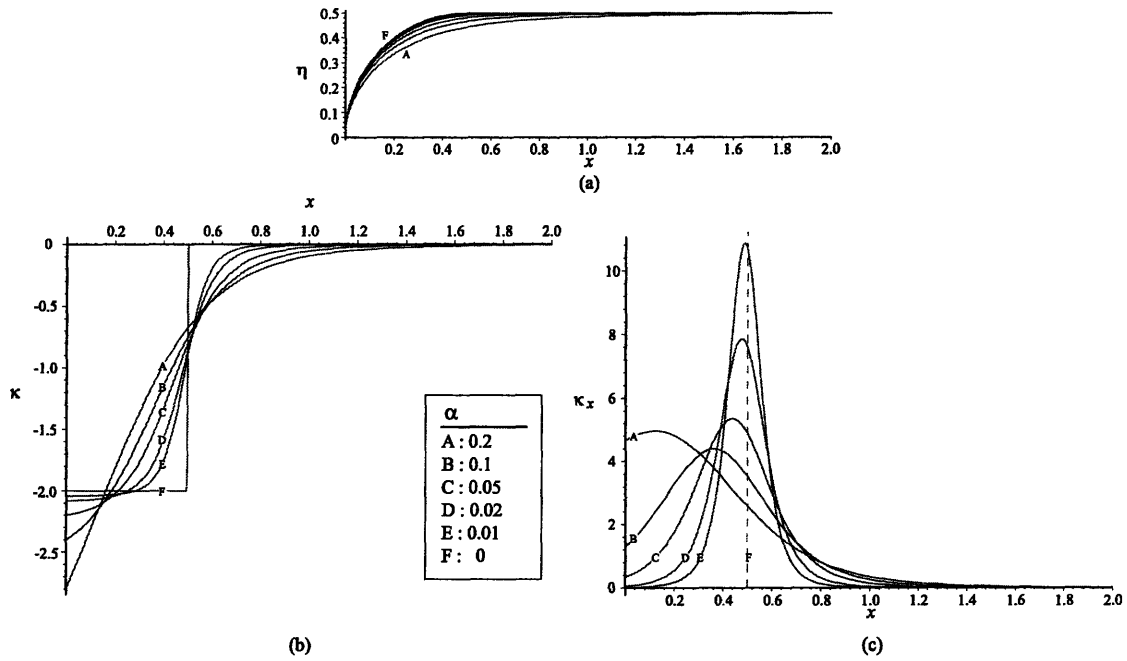
Figure B-2: Film profiles, (a), their curvature, (b) and curvature gradient, (c) for different values of α.

sheet shape. In the numerical computations, we typically used $\alpha = 1/20$ to $1/100$. Two formulae of interest is the curvature and its derivative at the tip:

$$\kappa\,(0;\alpha) = -2 - 4\alpha \tag{B.9}$$

$$\kappa_x\,(0;\alpha) = \frac{48\alpha^2\,(3 + 2\alpha)}{1 + 2\alpha} \tag{B.10}$$

As we increase α, the curvature at the tip *increases* and as does the curvature gradient. Figure B-2 shows some representative plots of these profiles. Choosing such forms for the initial film profile allows us to study the effect of the initial tip curvature on the retraction dynamics by simply varying the parameter α.

Appendix C

Tensor calculus

C.1   Christoffel symbols

The Christoffel symbols associated with the bases $\left\{\mathbf{g}_i, \mathbf{g}^i\right\}$ defined in equation (2.26) are:

$$\bar{\Gamma}^r_{ij} = \mathbf{g}^r \cdot \partial_j \mathbf{g}_i = \mathbf{g}^r \cdot \partial_i \mathbf{g}_j = -\mathbf{g}_i \cdot \partial_j \mathbf{g}^r \tag{C.1}$$

The computations are performed using the following identities

$$\partial_\beta \mathbf{g}_\alpha = \left(\partial_\beta q^\gamma_\alpha + q^\lambda_\alpha \Gamma^\gamma_{\beta\lambda}\right) \mathbf{e}_\gamma + b_{\beta\lambda} q^\lambda_\alpha \mathbf{e}_3 \tag{C.2}$$

$$\partial_3 \mathbf{g}_\alpha = \partial_\alpha \mathbf{g}_3 = -b^\beta_\alpha \mathbf{e}_\beta \tag{C.3}$$

$$\partial_3 \mathbf{g}_3 = 0 \tag{C.4}$$

These yield,

$$\bar{\Gamma}^\alpha_{3\beta} = \mathbf{g}^\alpha \cdot \partial_3 \mathbf{g}_\beta = -b^\gamma_\beta \left(q^\rho_\rho \delta^\alpha_\gamma - q^\alpha_\gamma\right)/Q \tag{C.5}$$

$$\bar{\Gamma}^\gamma_{\alpha\beta} = \mathbf{g}^\gamma \cdot \partial_\alpha \mathbf{g}_\beta = \left(q^\rho_\rho \delta^\gamma_\lambda - q^\gamma_\lambda\right)\left(\partial_\beta q^\lambda_\alpha + q^\xi_\alpha \Gamma^\lambda_{\beta\xi}\right)/Q \tag{C.6}$$

$$\bar{\Gamma}^3_{\alpha\beta} = b_{\beta\lambda} q^\lambda_\alpha \tag{C.7}$$

$$\bar{\Gamma}^i_{33} = \bar{\Gamma}^3_{3\alpha} = 0 \tag{C.8}$$

where $Q = q^1_1 q^2_2 - q^2_1 q^1_2$.

Bibliography

[1] Anderson, W. E., Ryan, H. M. & Santoro, R. J. 1995 Impinging jet injector atomization. In *Liquid Rocket Engine Combustion Instability*, vol. 169. AIAA.

[2] Aris, R. 1962 *Vectors, Tensors, and the Basic Equations of Fluid Mechanics*. Dover.

[3] Aristoff, J., Lieberman, C., Chan, E. & Bush, J. W. M. 2006 Water bell and sheet instabilities. *Phys. Fluids* **18**(9), 1109.

[4] Barenblatt, G. I., Beretta, E. & Bertsch, M. 1997 The problem of the spreading of a liquid film along a solid surface: A new mathematical formulation. *Proc. Natl. Acad. Sci.* **94**, 10024-10030.

[5] Bark, F. H., Wallin, H.-P., Gällsted, M. G. & Kristiansson, L. P. 1978 Swirling water bells. *J. Fluid Mech.* **90**, 625-639.

[6] Batchelor, G. K. 1967 *An Introduction to Fluid Mechanics*. Cambridge University press.

[7] Bayvel, L. & Orzechowski, Z. 1993 *Liquid Atomization*. Taylor and Francis.

[8] Blanchard, D. C. 1966 *From raindrops to volcanoes: adventures with sea surface meteorology*. Dover.

[9] Bond, W. N. 1935 The surface tension of a moving water sheet. *Proc. Phys. Soc. B* **67**, 549-558.

[10] Boussinesq, J. 1869 Théories des expériences de Savart, sur la forme que prend une veine liquide après s'être choquée contre un plan circulaire. *C. R. Acad. Sci. Paris* **69**, 45-48.

[11] Boussinesq, J. 1869 Théories des expériences de Savart, sur la forme que prend une veine liquide après s'être heurtée contre un plan circulaire (suite). *C. R. Acad. Sci. Paris* **69**, 128-131.

[12] Bremond N. & Villermaux E. 2006 Atomization by jet impact. *J. Fluid Mech.* **549**, 273-306.

[13] Brenner, M.P. & Gueyffier, D. 1999 On the bursting of viscous films. *Phys. Fluids* **11**, 737-739.

[14] Brown, D. R., 1961 A study of the behaviour of a thin sheet of a moving liquid. *J. Fluid Mech.* **10**, 297-305.

[15] Buckmaster, J. D., Nachman, A. & Ting, L. 1975 The buckling and stretching of a viscida. *J. Fluid Mech.* **69**, 1-20.

[16] Buckingham, R. & Bush, J. W. M. 2001 Fluid polygons. *Phys. Fluids* **13**(9), S10.

[17] Bush, J. W. M. & Hasha, A. E. 2004 On the collision of laminar jets: fluid chains and fishbones. *J. Fluid Mech*, **511**, 285-310.

[18] Cairncross, R. A., Schunk, P. R., Baer, T. A., Rao, R. R. & Sackinger, P. A. 2000 A finite element method for free surface flows of incompressible fluids in three dimensions. Part I. Boundary fitted mesh motion. *Int. J. Numer. Meth. Fluids* **33**, 375-403.

[19] Chan, T. F. & Jackson, K. R. 1984 Nonlinearly preconditioned Krylov subspace methods for discrete Newton algorithms. *SIAM J. Sci. Stat. Comput.*, **5**, 533-542.

[20] Chandrasekhar, S. 1961 *Hydrodynamic and Hydromagnetic Stability.* Dover.

[21] Chepushtanova, S. V. & Kliakhandler, I. L. 2007 Slow rupture of viscous films between parallel needles. *J. Fluid Mech.* **573**, 297-310.

[22] Choo, Y.-J. & Kang, B.-S. 2002 The velocity distribution of the liquid sheet formed by two low speed impinging jets. *Phys. Fluids* **14**, 622-627.

[23] Chiu-Webster, S. & Lister, J. R. 2006 The fall of a viscous thread onto a moving surface: a 'fluid-mechanical sewing machine'. *J. Fluid Mech.* **569**, 89-111.

[24] Clanet, C. 2000 Stability of water bells generated by jet impacts on a disk. *Phys. Rev. Lett.* **85**(24), 5106-5109.

[25] Clanet, C. 2001 Dynamics and stability of water bells. *J. Fluid Mech.* **430**, 111-147.

[26] Clanet, C. & Villermaux, E. 2002 Life of a smooth liquid sheet. *J. Fluid Mech.* **462**, 307-340.

[27] Clanet, C. 2007 Waterbells and liquid sheets. *Annu. Rev. Fluid Mech.* **39**, 469-496.

[28] Crapper, G. D., Dombrowski, N., Jepson, W. P. & Pyot, G. A. D. 1973 A note on the growth of Kelvin-Helmholtz waves on thin liquid sheets. *J. Fluid Mech.* **57**, 671-672.

[29] Cruickshank, J. O. & Munson, J. 1981 Viscous buckling of plane and axisymmetric jets. *J. Fluid Mech.* **113**, 221-239.

[30] Cruickshank, J. O. 1988 Low-Reynolds-number instabilities in stagnating jet flows. *J. Fluid Mech.* **193**, 111-127.

[31] Culick, F. E. C. 1960 Comments on a ruptured soap film. *J. Appl. Phys.* **31**, 1128-1129.

[32] Dalnoki-Veress, K., Nickel, B. G., Roth, C. & Dutcher, J. R. 1999 Hole formation and growth in freely standing polystyrene films. *Phys. Rev. E.* **59**(2), 2153-2156.

[33] de Luca, L. & Costa, M. 1997 Instability of a spatially developing liquid sheet. *J. Fluid Mech.* **331**, 127-144.

[34] de Luca, L. 1999 Experimental investigation of the global instability of plane sheet flows. *J. Fluid Mech.* **332**, 355-376.

[35] Debrégeas, G., Martin, P. & Brochard-Wyart, F. 1995 Viscous bursting of suspended films. *Phys. Rev. Lett.* **75**, 3886-3889.

[36] Debrégeas, G., de Gennes, G. P. & Brochard-Wyart, F. 1998 The life and death of viscous "bare" bubbles. *Science* **279**, 1704-1709.

[37] Do Carmo, M. P. 1976 *Differential Geometry of Curves and Surfaces.* Prentice-Hall, Engelwood Cliffs, NJ.

[38] Dombrowski, N. & Fraser, R. P. 1954 A photographic investigation into the disintegration of liquid films. *Philos. Trans. R. Soc. London Ser. A.* **247**, 101-130.

[39] Dombrowski, N. & Hooper, P. C. 1963 A study of the sprays formed by impinging jets in laminar and turbulent flow. *J. Fluid Mech.* **18**, 392-400.

[40] Dupré, M. A. 1867 Sixième memoire sur la theorie méchanique de la chaleur. *Ann. Chim. Phys.* **4**(11), 194.

[41] Eggers J. 1997 Nonlinear dynamics and breakup of free surface flows, *Rev. Mod. Phys.* **69**, 865-929.

[42] Eggers, J. & Brenner M. P. 2000 Spinning jets. In: H.-C. Chang (ed.), *Proceedings of the IUTAM Symposium on Nonlinear Waves in Multi-Phase Flow.* Kluwer, Dordrecht.

[43] Eggers, J. & Dupont T. F. 1994 Drop formation in a one-dimensional approximation of the Navier-Stokes equation. *J. Fluid Mech.* **262**, 205-221.

[44] Erneux, T. & Davis, S. H. 1993 Nonlinear rupture of free films. *Phys. Fluids A* **5**(5), 1117-1122.

[45] van de Fliert, B. W., Howell, P. D. & Ockenden, J. R. 1995 Pressure-driven flow of a thin viscous sheet. *J. Fluid Mech.* **292**, 359-376.

[46] Finnicum, D. S., Weinstein, S. J. & Ruschak, K. J. 1993 The effect of applied pressure on the shape of a two-dimensional liquid curtain falling under the influence of gravity. *J. Fluid Mech.* **255**, 647-665.

[47] Frankel, S. & Mysels, K. J. 1969 The bursting of soap films II. Theoretical considerations. *J. Phys. Chem.* **73**, 3028-3038.

[48] Fullana, G. M. & Zaleski, S. 1999 Stability of a growing rim in a liquid sheet of uniform thickness. *Phys. Fluids* **11**, 952-954.

[49] de Gennes, P. G., Brochart-Wyart, F. & Quéré, D. 2003 *Capillarity and wetting phenomena: drops, bubbles, pearls, waves.* Springer, New York.

[50] Eisenstat, S. C., Elman, H. C. & Schultz, M. H. 1983 Variational iterative methods for nonsymmetric systems of linear equations. *SIAM J. Num. Anal.*, **20** (2), 345-357.

[51] Gassser, J. C. & Marty, P. H. 1994 Liquid sheet modelling in an electromagnetic swirl atomizer. *Eur. J. Mech. B*, **13**(6), 765-784.

[52] Gordillo. J. M., Cheng, Z., Ganan-Calvo, A. M., Márquez, M. and Weitz, D. A. 2004 A new device for the generation of microbubbles. *Phys Fluids* **16**, 2828-2834.

[53] Green, A. E. & Zerna, W. 1992 *Theoretical elasticity*. Dover.

[54] Hasson, D. & Peck, R. E. 1964 Thickness distribution in a sheet formed by impinging jets. *AICHE J.* **10** (5), 752-754.

[55] Hopwood, F. L. 1952 Water bells. *Proc. Phys. Soc. B* **65**, 2-5.

[56] Howell, P. D. 1996 Models for thin viscous sheets. *Eur. J. Appl. Maths* **7**, 321-343.

[57] Hu X. & Jacobi A. M. 1998 Departure-site spacing for liquid droplets and jets falling between horizontal circular tubes. *Exp. Thermal Fluid Sc.* **16**, 322-331.

[58] Johnson, M. F., Miksis, M. J., Schluter, R. J. & Bankoff, S. G. 1996 Fluid chains produced by obliquely intersecting viscous jets connected by a thin free liquid film. *Phys. Fluids:Gallery of Fluid Motion* **8**, S2.

[59] Huang, J. C. P. 1970 The break-up of axisymmetric liquid sheets. *J. Fluid Mech.* **43**, 305-319.

[60] Ida, M. P. & Miksis, M. J. 1996 Thin film rupture. *Appl. Math. Lett.* **9**(3), 35-40.

[61] Ida, M. P. & Miksis M. J., 1998, The dynamics of thin films I: General theory, *SIAM J Appl Math*, **58**, 456-473.

[62] Joanny, J.-F. & de Gennes, P. G. 1987 Bursting of a soap film in a viscous environment. *Physica A* **147**, 238-255.

[63] Keller, J. B. 1983 Breaking of liquid films and threads. *Phys. Fluids* **26**, 3451-3453.

[64] Keller, J. B. & Miksis, M. J. 1983 Surface tension driven flows. *SIAM J. Appl. Math.* **43**, 268-277.

[65] Kelley, C. T. 1995 *Iterative Methods for Linear and Nonlinear Equations*, SIAM.

[66] Kelley, C. T. 2003 *Solving Nonlinear Equations with Newton's Method*, SIAM.

[67] Kendall, J. M., Lee, M. C. & Wang, T. G. 1982 Metal technology based upon hollow jet instability. *J. Vac. Sci. Technol.* **20**, 1091-1093.

[68] Kendall, J. M. 1986 Experiments on annular liquid jet instability and on the formation of liquid shells. *Phys. Fluids* **29**, 2086-2094.

[69] Knoll, D. A. & Keyes D. E. 2004 Jacobian-free Newton-Krylov methods: a survey of approaches and applications. *J. Comp. Phys.* **193,** 357-397.

[70] Lance, G. N. & Perry, R. L. 1953 Water Bells. *Proc. Phys. Soc. B* **66**, 1067-1072.

[71] Le Grand, N., Brunet, P., Lebon, L. & Limat, L. 2005 Propagating waves pattern in a falling liquid curtain. *Phys. Rev. E* **74**, 026305.

[72] Lefebvre, A. H. 1989 *Liquid Atomization.* Hemisphere.

[73] Lin, S. P. & Roberts, G. 1981 Waves in a viscous liquid curtain. *J. Fluid Mech.* **112,** 443-458.

[74] Lin, S.P. 1981 Stability of a viscous liquid curtain. *J. Fluid Mech.* **104**, 111-118.

[75] Lorenceau, E., Utada, A. S., Link, D. R., Cristobal, G., Joanicot, M. and Weitz, D. A. 2006 Generation of polymerosmes from double-emulsions. *Langmuir* **21**, 9183-9186.

[76] Mansour, A. & Chigier, N. 1990 Disintegration of liquid sheets. *Phys. Fluids. A* **2**(5), 706-719.

[77] McEntee, W. R. & Mysels, K. J. 1969 The bursting of soap films. I. An experimental study. *J. Phys. Chem.* **73,** 3018-3028.

[78] Mehring, C. & Sirignano, W. A. 1999 Nonlinear capillary wave distortion and disintegration of thin planar liquid films. *J Fluid Mech.* **388**, 69-113.

[79] Miyamoto, K. & Katagiri, Y. , 1997 Curtain coating in *Liquid Film Coating*, edited by S. F. Kistler and P. M. Schweizer. Chapman & Hall, London, 463–494.

[80] Notz, P. K. & Basaran, O. A. 2004 Dynamics and breakup of contracting filaments. *J. Fluid Mech.* **512**, 223-256.

[81] Pacheco, J. R. & Peck, R. E. 2000 Nonstaggered Boundary-fitted coordinate method for free surface flows. *Numer. Heat Trans. B* **37**, 267-291.

[82] Pandit, A. B. & Davidson, J. F. 1990 Hydrodynamics of the rupture of thin liquid films. *J. Fluid Mech.* **212**, 11-24.

[83] Parlange, J.-Y. 1967 A theory of water bells. *J. Fluid Mech.* **29**, 361-372.

[84] Pearson, J. R. A. 1985 *Mechanics of Polymer Processing.* Elsevier.

[85] Pearson, J. R. A. & Petrie, C. J. S. 1970 The flow of a tubular film. Part 1. Formal mathematical representation. *J. Fluid Mech.* **40**, 1-19.

[86] Pearson, J. R. A. & Petrie, C. J. S. 1970 The flow of a tubular film. Part 2. Interpretation of the model and discussion of solutions. *J. Fluid Mech.* **42**, 609-625.

[87] Peregrine, D.H., Shoker, G. & Symon, A. 1990 The bifurcation of liquid bridges. *J. Fluid Mech.* **212**, 25-39.

[88] Pomeau, Y. & Villermaux E. 2006 Two hundred years of capillary research. *Physics Today* **59**, 39-44.

[89] Pressley, A. 2001 *Elementary Differential Geometry.* Springer-Verlag, London.

[90] Prévost, M. & Gallez, D. 1986 Nonlinear rupture of thin liquid films. *J. Chem. Phys.* **84**(7), 4043-4048.

[91] Quéré, D. & Reyssat, É. 2006 Bursting of a fluid film in a viscous environment. *Europhys. Lett.* **76**, 232-242.

[92] Ranz, W. E. 1959 Some experiments on the dynamics of liquid films. *J. Appl. Phys.* **30**, 1950-1955.

[93] Rayleigh, Lord 1878 On the instability of jets. *Proc. Lond. Math. Soc.* **4**, 10.

[94] Rayleigh, Lord 1891 Some applications of photography. *Nature* **44**, 249-254.

[95] Ribe, N. M. 2001 Bending and stretching of thin viscous sheets. *J. Fluid Mech.* **433**, 135-160.

[96] Ribe, N. M. 2002 A general theory for the dynamics of thin viscous sheets. *J. Fluid Mech.* **457**,255-283.

[97] Ribe, N. M. 2003 Periodic folding of viscous sheets. *Phys. Rev. E.* **68**, 036305.

[98] Rieber, M. & Frohn, A. 1999 A numerical study on the mechanism of splashing. *Int. J. Heat and Fluid Flow* **20**, 455-461.

[99] Roth C. B., Deh, B., Nickel, B. G., Dutcher, J. R. 2005 Evidence of convective constraint release during hole growth in freely standing polystyrene films at low temperatures. *Phys. Rev. E* **72** (2), 021802.

[100] Savart, F. 1833 Memoire sur le choc d'une veine liquide lancée contre un plan circulaire. *Ann. de Chim.* **54**, 56-87.

[101] Savart, F. 1833 Suite du memoire sur le choc d'une veine liquide lancée contre un plan circulaire. *Ann. de Chim.* **54**, 113-145.

[102] Savart, F. 1833 Memoire sure le choc de deux veines liquides animées de mouvements directement opposés. *Ann. de Chim.* **55**, 257-310.

[103] Schmid, P. J. & Henninngson, D. S. 2002 On the stability of a falling liquid curtain. *J. Fluid Mech.* **463**, 163-171.

[104] Schulkes, R. M. S. M. 1996 The contraction of liquid filaments. *J. Fluid Mech.* **309**, 277-300.

[105] Scriven, L. E. 1960 Dynamics of a fluid interface. *Chem. Engng Sci.* **12**, 98-108.

[106] Sheludko, A. 1967 Thin liquid films. *Adv. Colloid Interface Sci.* **1**, 391-463.

[107] Skorobogatiy, M. & Mahadevan, L. 2000 Folding of viscous sheets and filaments. *Europhys. Lett.* **52**, 532-538.

[108] Song, M. & Tryggvason, G. 1999 The formation of thick borders on an initially stationary fluid sheet. *Phys. Fluids* **11**, 2487-2493.

[109] Stone, H. A., Koehler, S. A., Hilgenfeldt, S. and Durand, M. 2003 Perspectives on foam drainage and the influence of interfacial rheology. *J. Phys.: Condens. Matter* **15**, S283.

[110] Strogatz, S. 2000 *Nonlinear dynamics and chaos.* Perseus Publishing.

[111] Sünderhauf, G., Raszillier, H. & Durst, F. 2002 The retraction of the edge of a planar liquid sheet. *Phys. Fluids* **14**, 198-208.

[112] Taylor, G. I. & Howarth, L. 1959 The dynamics of thin sheets of fluid. I. Water bells. *Proc. R. Soc. London, Ser. A.* **253**, 289-295.

[113] Taylor, G. I. 1959 The dynamics of thin sheets of fluid. II. Waves on fluid sheets. *Proc. R. Soc. London, Ser. A.* **253**, 296-312.

[114] Taylor, G. I. 1959 The dynamics of thin sheets of fluid. III. Disintegration of fluid sheets. *Proc. R. Soc. London, Ser. A.* **253**, 313-321.

[115] Taylor, G. I. 1960 Formation of thin flat sheets of water. *Proc. R. Soc. London, A,* **259**, 1-17.

[116] Taylor, G. I. 1963 *The scientific papers of G. I. Taylor,* vol. 3, no. 25. Cambridge University Press.

[117] Taylor, G. I. 1969 Instability of jets, threads, and sheets of viscous fluid. *Proc. 12th Intl Congr. Appl. Mech., Stanford, 1968,* pp. 382-388. Springer.

[118] Taylor, G. I. & Michael, D. I. 1973 On making holes in a sheet of fluid. *J. Fluid Mech.* **58**, 625-639.

[119] Teng, C. H., Lin, S. P. & Chen, J. N. 1997 Absolute and convective instability of a viscous liquid curtain in a viscous gas. *J. Fluid Mech.* **332**, 105-120.

[120] Utada, A. S., Lorenceau, E. Link, D. R., Kaplan, P. D., Stone, H. A. & Weitz, D.A. 2005 Monodisperse double emulsions generated from a microcapillary device. *Science* **308**, 537-541.

[121] Vaynblat, D., Lister, J.R. & Witelski, T.P. 2001 Rupture of thin viscous films by van der Waals forces: evolution and self-similarity. *Phys. Fluids* **13**(5), 1130-1140.

[122] Villermaux, E. & Clanet, C. 2002 Life of a flapping liquid sheet. *J. Fluid Mech.* **462**, 341-363.

[123] Villermaux, E. 2007 Fragmentation. *Annu. Rev. Fluid Mech.* **39**, 419-446.

[124] Warsi, Z. U. A. 1998 *Fluid Dynamics, theoretical and computational approaches.* CRC Press.

[125] Weihs, D. 1978 Stability of thin, radially moving liquid sheets. *J. Fluid Mech.* **87**, 289-298.

[126] Wesseling, P. 2001 *Principles of computational fluid dynamics.* Springer-Verlag, Berlin.

[127] Worthington A. M. 1908. *A study of splashes.* Longmans, Green.

[128] Yarin, A. L., Gospondinov, P. & Roussinov, V. I. 1994 Stability loss and sensitivity in hollow fiber drawing. *Phys. Fluids* **6**(4), 1454-1463.

[129] Yarin, A. L. & Tchavdarov, B. M. 1996 Onset of folding in plane liquid films. *J. Fluid Mech.* **307**, 85-99.

[130] Yarin, A. L. 2006 Drop impact dynamics: splashing, spreading, receding, bouncing... *Annu. Rev. Fluid Mech.* **38**, 159-192.

[131] Zhang, J. E. 1996 *Run-up of ocean waves on beaches.* PhD Thesis, California Institute of Technology, Pasadena, CA.